

**OVERCOMING INTRINSIC SPIN RESONANCES BY
USING AN RF DIPOLE**

Mei Bai

Submitted to the faculty of the Graduate School
in partial fulfillment of the requirements
of the degree
Doctor of Philosophy
in the Department of Physics
Indiana University

February 1999

Accepted by the Graduate Faculty, Indiana University, in partial fulfillment of the requirements of the degree of Doctor of Philosophy.

Shyh-Yuan Lee, Ph.D.

Robert E. Pollock, Ph.D.

Doctoral
Committee

Peter Schwandt, Ph.D.

J. Scott Berg, Ph.D.

January 12, 1999

Copyright ©1999 by
Mei Bai
ALL RIGHTS RESERVED

To my parents and my family

Acknowledgments

This work could not come out without help, support and collaborative effort from many people. Whatever mention I can make of them here can not match their true contributions and my deep appreciation.

First of all, I would like to acknowledge my thesis advisor, Prof. S.Y. Lee, for his earnest guidance, inculcation and continued encouragement. As an excellent teacher, he intrigued my great interest in accelerator physics and influenced me with his scrupulous and assiduous attitude.

I am specially grateful to my two supervisors at Brookhaven AGS, Dr. T. Roser and Dr. M. Syphers. Their enlightening guidance, helpful advice and tremendous support have helped me find my way through mazes that had to be traversed in the course of my research work. I feel so fortune to have them as mentors. I also sincerely thank Dr. A. Yokosawa who gave me this opportunity to work as a guest graduate student of Argonne National Laboratory.

I thank Dr. G. Bunce, Dr. H. Huang, Dr. Y. I. Makdisi, Dr. L. Ratner, Dr. H. Spinka and Dr. D. G. Underwood. Their invaluable suggestions, insights in high energy physics and accelerator physics and constant support have substantially benefited me on my thesis work

I also owe an ongoing debt of gratitude to all the E880 collaborators who had made the successful E880 experiments happen. In particular, I would like to thank Dr. L. Ahrens, Dr. W. van Asselt, Dr. J. W. Glenn, Dr. A. Luccio, Dr. N. Tsoupas, Dr. P. Cameron, Dr. E. D. Courant, Dr. S. Tepikian, K. Brown and N. Williams for their enormous help, suggestions and fruitful discussions. The success of the experiments also can not be separated from the tremendous help from engineers R. Sanders who designed and tested the resonant driving circuit of the AGS RF dipole, Ann Dunbar who helped in constructing and testing the magnet, G. Smith who also helped us

with BPM system, D. Gassner, G. J. Mahler, S. Naase and the AGS operation crew, J. Reich, P. Sampson, C. Whalen and K. Zeno. I also thank the AGS chairperson, Dr. D. I. Lowenstein, for giving me this wonderful chance to work in the AGS and providing me an excellent accommodation. At last, I thank all the AGS personnel who provided me with such a friendly and cooperative atmosphere.

Again, I would like to thank my advisor committee members Prof. R. E. Pollock, Prof. V. P. Schwandt, Prof. J. S. Berg, who have also helped me in many ways. In addition, thanks are due especially to my present and former fellow colleagues at IUCF Dr. C. M. Chu, Dr. D. Jeon, Dr. X. Kang, Dr. D. Li, Dr. J. Liu, M. Berglund and X. Zhao.

My two years in Bloomington have let me meet so many wonderful people, the professors whose classes I enjoyed and am benefited, the department secretaries, B. Carson and J. Dizer who gave me their generous help and assistance especially when I was off campus. I also made a lot friends there, who gave me their precious friendship and brought me various joys of life. In this regard, I would like to thank my best friend X. Yang and her husband Adam, my classmates Kehan Jiang, Lin Chen, Xiong Fang, Xichen Jiang and Min Li and other friends Yong Wang and his wife Jing Li, Liemin Chen and his wife Yuan Yao, Zhiguo Huang, Jin Shao, Cao Yu, Shaolin Chen, Jiayu Ba, Yuezheng Zhou, Dayong Liu, Cong Yan and Haichuan Yang.

Finally, I would like to express my appreciations to my parents for raising me and giving me their care, to my husband Gang Wang for giving me his love and support, to my brother for all the laughs and quarrels we had as we grew up, and to my niece whom I have not met.

Abstract

Mei Bai

Overcoming Intrinsic Spin Resonances by Using an RF Dipole

Although the 5% partial Siberian snake has been demonstrated to be able to overcome the imperfection spin resonances in the AGS, it is still too weak to correct the intrinsic spin resonances in the AGS as well. To accelerate polarized protons to 25 GeV/c, the injection energy of the Relativistic Heavy Ion Collider, seven intrinsic spin resonances are encountered, i.e. $0 + \nu_z$, $12 + \nu_z$, $24 \pm \nu_z$, $36 \pm \nu_z$ and $48 - \nu_z$. Four of them are strong ones: $0 + \nu_z$, $12 + \nu_z$ and $36 \pm \nu_z$, and every one of them can partially or even fully destroy the beam polarization.

To overcome these strong intrinsic spin resonances, an RF dipole was employed in the AGS polarized proton acceleration. A strong coherent oscillation was excited by the RF dipole at each of the spin resonances. Particles in the beam core then experienced stronger focusing fields and the average effective spin resonance strength of the beam was greatly enhanced. If the driven coherent oscillation is strong enough, a full spin flip can be induced under the normal AGS acceleration rate. This has been proven in the recent AGS polarized proton acceleration experiments. Unlike other non-adiabatic beam manipulations, the coherent oscillation can be excited in an adiabatic manner by slowly turning on and off the RF dipole and beam emittance can be preserved.

The principle of the adiabatic excitation of a coherent oscillation by an RF dipole is discussed in this thesis. The experimental data of using an RF dipole to overcome intrinsic spin resonances are presented. The results of a new type of second order spin resonance observed in the AGS polarized proton acceleration experiment are also included.

Shyh-Yuan Lee, Ph.D.

Robert E. Pollock, Ph.D.

Peter Schwandt, Ph.D.

J. Scott Berg, Ph.D.

Contents

Acceptance	ii
Acknowledgments	vi
Abstract	viii
1 Introduction	1
2 Spin Dynamics in Synchrotrons	7
2.1 Anomalous g -factor	8
2.2 Spin Precession in an External Electro-magnetic Field	9
2.3 Spin Motion in Synchrotrons	12
2.3.1 Differential Equation of the Spinor	15
2.3.2 Spin Depolarization Resonance and Corrections	19
2.3.3 Effect of Crossing a Single Isolated Spin Resonance – Froissart- Stora Formula	22
2.3.4 Spin Resonance Correction	24
3 RF Dipole - A Novel Solution For Intrinsic Spin Resonances	28
3.1 The Non-linear Detuning Effect	32
3.2 The Effect On The Spin Motion	36

4	Experimental Apparatus	39
4.1	RF Dipole Magnet	41
4.2	The Control Program	43
4.3	AGS Internal Polarimeter	45
4.4	AGS 5% Partial Siberian Snake	48
5	Experimental Results	52
5.1	Results Of Experiments With The AGS Au ⁺⁷⁷ Beam	52
5.2	The AGS Chromaticity Setting	60
5.3	Spin Experimental Results	66
5.3.1	RF dipole amplitude scan at three resonances	69
5.3.2	The resonant proximity parameter δ scan	73
5.3.3	Effective analyzing power of fishline	73
5.4	Effects of Linear Betatron Coupling	77
5.5	Second Order Spin Resonance	78
6	Conclusions and Future Prospects	88
6.1	Conclusions	88
6.2	Prospects Of Polarized Proton Beam Acceleration in the AGS	90
A	Multi-particle distribution in the numerical simulation of two spin resonance model	93
B	Other applications of adiabatic coherent excitation	95
B.1	Using the RF dipole as a diagnostic tool to measure the Courant-Snyder parameters	95
B.2	Spin flipper	97
C	Figure 5.4 and Figure 5.3 data	99

<i>CONTENTS</i>	xi
D Figure 5.8 and Figure 5.9 data	101
E Experimental data of second order resonance.	104

List of Tables

2.1	Intrinsic resonance strengths for the AGS	22
5.1	The coefficients of the empirical parameterized formula.	63
5.2	AGS intrinsic spin resonances in the acceleration from 2.27 GeV/c to 25 GeV/c	67
5.3	Schemes for spin resonance correction.	69
5.4	analyzing power at $G\gamma = 13.5, 24.5$ and 30.5	76
C.1	Data of Figure 5.4.	99
C.2	Data of Figure 5.3.	100
D.1	Data of the RF dipole amplitude scan and the resonance proximity parameter δ scan at $12 + \nu_z$ in Figure 5.8 and Figure 5.9.	101
D.2	Data of RF dipole amplitude scan at $0 + \nu_z$	102
D.3	Data of RF dipole amplitude scan at $36 - \nu_z$	103
E.1	Data of $\cos 9\theta$ and $\sin 9\theta$ current scan in Figure 5.13.	104
E.2	Data of energy scan in Figure 5.11.	105
E.3	Data of RF dipole turn-on time scan in Figure 5.12.	106

List of Figures

2.1	Curvilinear coordinate system in circular accelerators.	13
2.2	With a single full snake in the ring, the spin vector is flipped when the particle finishes one revolution. Thus, the kick acted on the spin vector from the perturbation field will cancel the kick the spin vector received in the previous turn.	25
2.3	The left part corresponds to the betatron tune and $G\gamma$ change during a normal acceleration cycle. The right part shows the betatron tune is jumped through the spin resonance and then ramped back to its nominal value.	27
3.1	Phase space motion in the rotating frame at the maximum betatron amplitude location.	32
3.2	The phase space in the resonant frame which rotates with the modulation tune ν_m	34
3.3	The fixed points in the normalized coordinate as a function of the modulation frequency parameter b/b_b	35
4.1	The acceleration complex of polarized proton	40
4.2	The AGS RF dipole control & driving system	42

4.3	The AGS RF dipole control program. The top picture is the front panel and the bottom one is the flow diagram of the RF dipole control program.	44
4.4	The schematic drawing of the AGS internal polarimeter setup	46
4.5	The $p - p$ elastic scattering analyzing power A_e calculated as Eq. (4.5) as a function of beam momentum	49
4.6	Top part: spin tune in the presence of different snake strength. Bottom part: spin closed orbit for a 5% partial snake. It shows that the beam polarization flips sign when it passes through the integer $G\gamma$ s.	50
5.1	Transverse displacement (top) and RF dipole magnet field amplitude (bottom) as a function of revolutions about the AGS. The raw PUE data was filtered to suppress the noise background.	53
5.2	Measured transverse rms beam size versus time in AGS cycle (top). Corresponding beam profiles versus time in AGS cycle (bottom). . . .	55
5.3	Normalized betatron oscillation amplitude versus δ . The solid line is the predicted curve using Eq. (3.18). The acceleration rate is zero for these measurements.	56
5.4	Normalized betatron oscillation amplitude versus δ . The solid line is the predicted curve using Eq. (3.18). The corresponding acceleration rate is $\dot{\gamma} = 2.44\text{sec}^{-1}$	57
5.5	The lower part is raw data of transverse oscillations in the presence of power line ripple. The top trace is the FFT of the data, showing the ripple sideband. For this trace, the horizontal axis is the fractional tune. The modulation tune, the large peak, is 0.273.	59

5.6	The comparisons of the MAD calculations of different models with the measured chromaticities. Model C is the same as Model B except the sextupole strength from the end of the AGS bending magnet is -0.0078 instead of -0.017. Since in the experiment, the measurement was taken at fixed energy, the second term in $K_{2S}L_S$ which reflects the eddy current effect was set to zero in the Model B and C calculations. . . .	65
5.7	The final beam polarization as a function of the beam vertical emittance after crossing the seven intrinsic resonances without corrections. The initial polarization is 1.0 and the acceleration rate $\alpha = 4.8 \times 10^{-5} \text{ rad}^{-1}$ for this calculation.	68
5.8	The measured proton polarization vs. the coherent betatron oscillation amplitude (in mm) for different tune separations at spin depolarizing resonances $0 + \nu_z$ (bottom plot), $12 + \nu_z$ (middle plot), and $36 - \nu_z$ (upper plot). P_z stands for the vertical polarization, while Z_{coh} stands for the vertical coherent oscillation amplitude. The error bars show only the statistical errors. The resonance strength of the coherent spin resonance due to the RF dipole is proportional to the coherent betatron amplitude. The curves are the results of multi-particle spin simulations based on a model with two overlapping spin resonances.	70
5.9	The measured proton beam polarization, at the spin resonance $12 + \nu_z$, vs the tune separation with a fixed RF dipole field strength. The line is the multi-particle simulation results with 1 normalized 95% beam emittance of $26\pi\text{mm-mrad}$, and an initial polarization of 0.45.	74
5.10	Target scans of the AGS internal polarimeter taken at $G\gamma = 13.5$ (top part) and $G\gamma = 7.5$ (bottom part).	78

5.11	The measured asymmetry for different beam energies, or equivalently, $G\gamma$ values. The dotted line shows the asymmetry expected from a 5% partial snake. It is scaled based on the assumption that the analyzing power is inversely proportional to the beam momentum.	79
5.12	Measured asymmetry vs the RF dipole turn-on time in $G\gamma$ value. Powering the RF dipole with a short pulse increased the vertical beam emittance significantly when the RF dipole was turned on before crossing the spin resonance at $G\gamma = 42.3$. The increased emittance made the resonance strong enough to partially flip the beam polarization. The beam polarization was measured at $G\gamma = 43.5$ energy flat-top.	81
5.13	Top: Measured asymmetry vs current of correctors which generate $\cos 9\theta$ oscillation while the current of $\sin 9\theta$ correctors was set at zero. Bottom: Scan of the corrector current for the $\sin 9\theta$ oscillation with the corrector current for the $\cos 9\theta$ oscillation set at 7A. The solid lines in both pictures are the fitting results. The range of the corrector power supply was about ± 25 A.	83
6.1	Results of numerical spin tracking with the regular AGS solenoid partial snake (dashed line) and with a 5% helical partial snake (solid line). The dots are the experimental results. The weak spin resonances at $G\gamma = 24 \pm \nu_z$ and $48 - \nu_z$ were corrected by the energy-jump method [26] in the numerical tracking with the helical partial snake. No corrections were taken for the weak resonances in the numerical tracking with the regular AGS solenoid partial snake. The RF dipole was used to overcome the intrinsic spin resonances at $G\gamma = 0 + \nu_z$, $12 + \nu_z$ and $36 \pm \nu_z$ in both calculations, and the beam emittance at horizontal and vertical plane is 40π mm-mrad and 9π mm-mrad respectively.	92

A.1	The distribution of thirty-two particles which simulates a Gaussian distributed beam	94
B.1	the schematic drawing of using an RF dipole and two BPMs to measure the linear optics.	96

Chapter 1

Introduction

After being introduced by George Uhlenbeck and Samuel Goudsmit in 1925 to explain the hyperfine splitting in the atomic spectra of hydrogen, spin became one of the fundamental concepts of atomic physics, nuclear physics, high energy physics and other fields. Today we all know that spin is an inherent quantum number which takes discrete values that are some multiple of $\frac{1}{2}$, and a deep understanding about spin and its effect in the particle interactions should bring us the essential information about the fundamental properties of elementary particles. One key approach to investigate the spin dependence of elementary particle interactions is to study scattering processes with spin polarized particles. In the past few decades, a series of experiments was carried out. Significant progress was made, yet many questions remained. For instance, the early SLAC polarized electron experimental data suggested the quarks only carry a small portion of the proton's spin. Then one question is to explain the remaining proton's spin. How to explain the disagreement between the earlier experimental results of proton-proton inelastic scattering and the predictions of the Perturbative QCD theory of hadronic interactions? These questions are expected to be answered by studying the scattering processes of higher and higher energy polarized beams.

Although modern accelerators are able to accelerate unpolarized beams up to hundreds of GeVs, it is still difficult to accelerate spin aligned beam particles to high energies without destroying the alignment of their spin vectors due to the depolarization effect which comes from the interaction between a particle's spin and the magnetic fields in accelerators, especially for protons. The electrons, on the other hand, have a unique gift from mother nature, namely the radiative polarization effect where electrons may polarize themselves by emitting photons (synchrotron radiation effect)! Since synchrotron radiation from protons is much weaker, the polarization cannot be recovered once depolarized. The acceleration of polarized proton beams requires careful tuning of machine parameters and delicate techniques to maintain the polarization through the acceleration.

Studies of spin motion in an accelerator in the presence of inhomogeneous magnetic fields arising from the beam orbital motion can be traced back to the early 1960's. In 1959, Bargmann, Michel and Telegdi re-derived the equation for spin precession in an external electro-magnetic field by reformulating the Thomas equation (1926) in covariant four-vector form. It was soon realized that these non-guiding magnetic fields in an accelerator could alter the spin motion and excite spin resonances if the perturbations on the spin motion add up coherently. In the same year, Froissart and Stora also calculated the effect of crossing a single isolated spin resonance on beam polarization.

In a perfect circular accelerator with vertical guiding magnetic fields, all spin vectors precess around the vertical direction which is the "spin closed orbit". In reality, particles may experience non-vertical magnetic fields in misaligned dipoles, quadrupoles and other non-linear magnets in the accelerator. These non-vertical magnetic fields tend to alter the particle spin away from the vertical direction. This perturbation is enhanced if the spin precession frequency coincides with the frequency at which the perturbing magnetic field kicks the spin vector. In this case, the spin is

kicked coherently every revolution around the accelerator and a spin depolarization resonance occurs.

Based on the source of the depolarization forces, spin depolarization resonances can be categorized into two types: *imperfection spin resonances* caused by vertical closed orbit distortion due to the imperfections of the accelerator, and *intrinsic spin resonances* caused by the vertical betatron oscillations of the particle orbit. Since the betatron motion is an intrinsic feature of synchrotrons, the polarized beam acceleration will encounter intrinsic spin resonance even in the absence of the synchrotron magnetic field imperfections. For a circular accelerator with P superperiods, the imperfection spin resonances happen at $G\gamma = k$, where $G\gamma$ is the unperturbed spin precession tune, G is the anomalous g-factor ($G=1.7928747$ for proton), γ is the relativistic Lorentz factor and k is an integer. The intrinsic spin resonances occur at $G\gamma = kP + \nu_z$, where ν_z is the vertical betatron tune. In addition to these two first order spin resonances, there are also higher order spin resonances driven by the coupling between horizontal and vertical planes, nonlinear magnetic fields provided by sextupoles or other higher order multipoles, synchrotron oscillations, etc. However, these higher order spin resonances are normally much weaker than the first order spin resonances, and the resulting depolarization is normally negligible.

The imperfection spin resonances can be overcome by correcting the vertical closed orbit distortion using harmonic dipole correctors, while the intrinsic spin resonances can be compensated with the fast tune jump method. In 1973 a polarized proton beam was first successfully accelerated to 12 GeV in the ZGS (Argonne) and reached 16.5 GeV later at the Brookhaven AGS by using these methods [2]. However, neither methods is flawless. First, the harmonic orbit correction is very sensitive to the variation of the vertical closed orbit, which depends on temperature changes, ground motion, tidal action, etc. Furthermore, the orbit correction method is very tedious, time consuming and hard to be made routine. The fast tune jump method, on the

other hand, is a non-adiabatic process and causes emittance dilution in the beam phase space.

In 1978, Derbenev and Kondratenko proposed to use a specially configured magnet to rotate the spin vector around the longitudinal axis by 180 degrees [3]. In this way, the perturbation of the spin motion which occurs during one revolution around the accelerator will cancel itself during the next turn. This type of magnet was become known as a Siberian snake. Unlike the harmonic correction method which is time consuming and becomes less efficient if there are numerous imperfection spin resonances that need to be corrected, the method of using a Siberian snake to avoid the depolarization is independent of the closed orbit condition and more practical for high energy polarized beam acceleration. This scenario was first tested in 1989 at the Indiana University Cyclotron Facility (IUCF) [4]. The experiment showed that the Siberian snake was able to eliminate the spin depolarization resonances during the acceleration. The ingenious concept of the Siberian snake not only provided us a good solution for polarized proton acceleration, but also stimulated the search for other suitable magnet configurations including: Steffen snake, partial snake and helical snake [6]. In the AGS at Brookhaven National Laboratory, because of the physical constraints, a 5% partial Siberian snake, which rotates the spin vector only by 9° degrees, was installed to compensate the imperfection spin resonances instead of employing a full Siberian snake which rotates the spin vector by 180° degrees. This technique was successfully tested at the AGS in 1994, and the experiment demonstrated that a 5% partial snake was adequate to overcome all the imperfection resonances in the AGS.

For intrinsic spin resonances, the fast tune jump method can result in severe emittance growth due to its non-adiabaticity, and also may cause trouble if there are several intrinsic spin resonances to be dealt with. This could also be a serious problem if it is required to maintain the emittance for some purpose. For instance, for the AGS, the beam emittance is very important when it serves as the injector

of the Relativistic Heavy Ion Collider (RHIC). Therefore, it is desirable to have an alternative to overcome the intrinsic spin resonances without sacrificing the emittance. One way to achieve this is to introduce an RF dipole magnet with a sinusoidally oscillating magnetic field to adiabatically force all the particles in the beam to oscillate coherently at a large amplitude and induce a full spin flip. Since this technique is an adiabatic manipulation, the beam emittance can be preserved. This method was first tested at the AGS in the July and November 1997 polarized proton experiments. Full spin flip was observed at $G\gamma = 0 + \nu_z$, $12 + \nu_z$ and $36 - \nu_z$, and a significant improvement of the achieved beam polarization was evident in comparison to previous polarized proton experiments. Together with the partial Siberian snake method for overcoming the imperfection spin resonances and other techniques for other weak spin resonances, beam polarization is expected to reach 70% at the RHIC injection energy of 25 GeV.

The scenario for RHIC polarized beam operation is to use 2 full snakes in each ring, which can overcome both the imperfection and intrinsic spin resonances [7]. The goal is to induce a polarized proton collisions at 250 GeV with 70% beam polarization. This provides an unique opportunity for the study of QCD and the spin structure of protons.

This thesis addresses this new method of overcoming the intrinsic spin resonances by using an RF dipole. An overview of spin dynamics is given in Chapter 2. The theoretical perspectives of using an RF dipole to adiabatically excite a sustained coherent oscillation with large amplitude are discussed in Chapter 3 along with the effect of driven coherent oscillation on the spin motion. In Chapter 4, hardware for polarized proton acceleration and the experimental setups are introduced. The results of polarized proton experiments are presented in Chapter 5. Earlier experimental results with the AGS Au⁺⁷⁷ beam for emittance manipulation and the measurement of AGS chromaticities for accelerator modeling are also included in this chapter.

Conclusions and future perspectives as well as other applications of the RF dipole method are presented in Chapter 5.

Chapter 2

Spin Dynamics in Synchrotrons

The behavior of polarized beam in synchrotrons is governed by the interaction between the magnetic moment of the circulating particle and the external electro-magnetic fields. In this chapter, the dynamics of spin motion in an external electro-magnetic field and the depolarization mechanism in synchrotrons are discussed. Since we are particularly interested in the acceleration of polarized protons, the discussion will only focus on the spin dynamics of spin $\frac{1}{2}$ particles.

For the class of spin $\frac{1}{2}$ particles, two eigen spin states exist, i.e. spin “up” or “down” along an arbitrary quantization axis. The spin state of a single spin $\frac{1}{2}$ particle in a pure spin state can be described by a unit vector along its quantization axis. This vector is generally named as spin vector. The asymmetry between the populations of spin “up” state and spin “down” state describes the degree of polarization of a beam of spin $\frac{1}{2}$ particles,

$$P = \frac{N_+ - N_-}{N_+ + N_-}, \quad (2.1)$$

where N_+ and N_- are the populations of spin “up” and “down” states. Equation (2.1) shows that a beam is fully polarized and its degree of polarization P is 100% when the spin vectors of all particles point to the same direction. As a collection of spin

$\frac{1}{2}$ particles, the beam spin vector is given by the ensemble average of the spin vector of every individual particle. The effect of a spin depolarization resonance on a single particle as well as on a beam of particles is also included in this chapter.

2.1 Anomalous g -factor

As an internal degree of freedom, the spin of a particle is associated with a magnetic momentum $\vec{\mu}$ given by

$$\vec{\mu} = g \frac{q}{2m_q} \vec{S} \quad (2.2)$$

where \vec{S} , q and m_q are respectively the spin, the electric charge and the rest mass of the particle, g is the gyro-magnetic ratio. For a pure Dirac particle, g is equal to 2 exactly. For real particles, g contains an anomalous part $G = \frac{g-2}{2}$ which arises from vacuum polarization in QED. The following table lists the anomalous g -factor for some particles.

Particle species	Anomalous gyro-magnetic factor
Electron e	1.159652×10^{-3}
Muon μ	1.165924×10^{-3}
Proton p	1.7928474
Deuteron D	-0.1429878

2.2 Spin Precession in an External Electro-magnetic Field

In the particle's rest frame, the spin vector interacts with the external electro-magnetic field \vec{E} and \vec{B} through the magnetic moment,

$$\frac{d\vec{S}}{dt} = \vec{\mu} \times \vec{B}. \quad (2.3)$$

The electric field \vec{E} , on the other hand, does not affect the spin motion. However, it will influence the spin motion if the particle moves and the Lorentz transformation induces magnetic field in the particle's rest frame. Thus for a moving particle, its spin equation of motion can be obtained by transforming Eq. (2.3) from the particle rest frame to the laboratory frame under the Lorentz transformation. The resulting spin equation of motion is called the Thomas-BMT equation [5, 6]

$$\frac{d\vec{S}}{dt} = \frac{e}{\gamma m} \vec{S} \times \left[(1 + G\gamma) \vec{B}_\perp + (1 + G) \vec{B}_\parallel + \left(G\gamma + \frac{\gamma}{\gamma + 1} \right) \frac{\vec{E} \times \vec{\beta}}{c} \right], \quad (2.4)$$

where \vec{S} is the spin vector in the particle's rest frame, e and m are respectively the electric charges and rest mass of the particle, \vec{B}_\perp and \vec{B}_\parallel are the transverse and longitudinal components of the magnetic fields in the laboratory frame with respect to the particle's velocity $\vec{\beta}c$, \vec{E} is the electric field and γ is the relativistic Lorentz factor.

The Thomas-BMT equation describes how the spin vector evolves in the presence of an external electro-magnetic field in general. To study the spin motion of a charged particle in a circular accelerator, it is more convenient to transform the Eq. (2.4) to the frame which rotates with the particle at the cyclotron frequency Ω_c

$$\Omega_c = -\frac{e}{\gamma m} \left[\vec{B} + \frac{\gamma^2}{\gamma^2 - 1} \frac{\vec{E} \times \vec{\beta}}{c} \right], \quad (2.5)$$

and Eq. (2.4) becomes:

$$\frac{d\vec{S}}{dt} = \frac{e}{\gamma m} \vec{S} \times [G\gamma \vec{B}_\perp + (1 + G)\vec{B}_\parallel + (G\gamma - \frac{\gamma}{\gamma^2 - 1}) \frac{\vec{E} \times \vec{\beta}}{c}]. \quad (2.6)$$

In general, a single spin $\frac{1}{2}$ particle can be found in either one of the two eigenstates or in a mixture of them with a certain probability distribution. A two component spinor $\Psi = \begin{pmatrix} u \\ d \end{pmatrix}$ is introduced to describe the spin state of a spin $\frac{1}{2}$ particle, where u and d are the probabilities of the particle being in the two pure spin states. The spin state can also be expressed by a spin vector with three components $\vec{S} = (S_1, S_2, S_3)$ defined as

$$S_i = \langle \Psi | \sigma_i | \Psi \rangle, \quad (2.7)$$

or

$$S_1 = u^* d + u d^*, \quad (2.8)$$

$$S_2 = i(u d^* - u^* d), \quad (2.9)$$

$$S_3 = |u|^2 - |d|^2, \quad (2.10)$$

where u^* and d^* are the complex conjugates of u and d , $\sigma_i, i = 1, 2, 3$ are the Pauli matrices,

$$\sigma_1 = \begin{pmatrix} 0 & 1 \\ 1 & 0 \end{pmatrix}, \quad \sigma_2 = \begin{pmatrix} 0 & i \\ -i & 0 \end{pmatrix}, \quad \sigma_3 = \begin{pmatrix} 1 & 0 \\ 0 & -1 \end{pmatrix}. \quad (2.11)$$

Although the concept of spin belongs to the quantum regime, the spin vector in the Thomas-BMT equation is a semi-classical variable. For a beam of spin $\frac{1}{2}$ particles, the spin vector is the statistical average of the single-particle spin vectors. The beam is fully polarized if the spin vectors of all particles all point along the same direction, and the beam polarization is 100%. Any deviation of the spin vector of an individual

particle leads to a partial polarized beam with less than 100% polarization. If the spin direction of each particle is distributed isotropically, the beam is unpolarized.

Several conclusions can be drawn from Eq. (2.6),

- In the absence of \vec{B}_{\parallel} and \vec{E} , it is the anomalous gyro-magnetic factor that gives rise to the deviation of the spin precession frequency with respect to the cyclotron frequency Ω_c .
- In a perfect accelerator with only the vertical guiding magnetic field, spin vectors which point away from the vertical axis precess around the vertical direction as particles circulate in the accelerator.
- In the absence of electric field, the frequency of spin precession in an ideal circular accelerator with pure vertical guiding magnetic field $\vec{B} = B_z \hat{z}$ is

$$\omega_s = \frac{e}{\gamma m}(1 + G\gamma)B_z.$$

Here we use \hat{z} to denote the vertical direction. In the frame which rotates with the particle at the cyclotron frequency $\Omega_c = -\frac{e}{\gamma m}\vec{B}_z$, the spin precession frequency becomes

$$\omega_s - \Omega_c = \frac{e}{\gamma m}G\gamma B_z.$$

In other words, the spin vector precesses $G\gamma$ times in one revolution of the particle around the accelerator. Thus, the spin tune ν_s is equal to

$$\nu_s = \frac{\omega_s - \Omega_c}{\Omega_c} = G\gamma.$$

- As the particle's energy increases, the spin rotating strength of a longitudinal magnetic field decreases, while the effect of the transverse magnetic field on the spin motion becomes nearly energy independent. Therefore, in the low and

medium energy regime, it is preferable to use a longitudinal field to manipulate the spin vector, and a transverse field is more efficient for spin manipulation at high energies.

- At a magic energy $\gamma = \sqrt{1 + \frac{1}{G}}$, the coefficient of the $\frac{\vec{E} \times \vec{\beta}}{c}$ term vanishes and the spin motion becomes independent of the electric fields. This phenomena can be used to determine the anomalous g -factor of a particle [6].
- Typically, an electric field of 3×10^6 V/m has a spin rotating strength comparable to a magnetic field of 100 Gauss. However, the electric fields applied in existing synchrotrons are much smaller and so their effect on the spin motion can be neglected.

2.3 Spin Motion in Synchrotrons

In synchrotrons, particles in a beam are distributed around the design trajectory (reference orbit) and perform transverse motion (betatron oscillation) while circulating around the accelerator. Usually, a curvilinear coordinate which is expanded about the reference orbit is used to describe the motion of a particle in a synchrotron [6, 9]. Its three unit base vectors \hat{x} , \hat{s} and \hat{z} are respectively along the radially outward, longitudinal and vertical axes shown in Fig. 2.1¹ and satisfy the following relations:

$$\frac{d\hat{x}}{ds} = \frac{\hat{s}}{\rho}, \quad \frac{d\hat{s}}{ds} = -\frac{\hat{x}}{\rho}, \quad \frac{d\hat{z}}{ds} = 0 \quad (2.12)$$

where s is the longitudinal coordinate and ρ is the local radius of the reference orbit. The particle's position can be written as

$$\vec{r}(s) = \vec{r}_0(s) + x\hat{x} + z\hat{z}, \quad (2.13)$$

¹courtesy of Prof. S. Y. Lee, Indiana University.

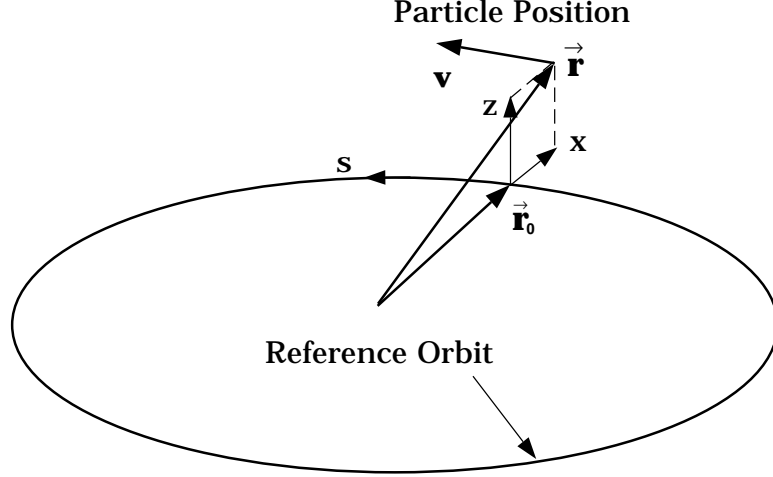


Figure 2.1: Curvilinear coordinate system in circular accelerators.

and $\vec{r}_0(s)$ is the reference orbit.

To study the effect of a particle's motion on its spin precession in synchrotrons, we express the Thomas-BMT equation Eq. (2.6) in terms of the particle's coordinates. Neglecting the effects of the electric field, the Thomas-BMT equation then becomes

$$\frac{d\vec{S}}{dt} = \frac{e}{\gamma m} \vec{S} \times [(1 + G\gamma)\vec{B}_\perp + (1 + G)\vec{B}_{//}], \quad (2.14)$$

where

$$\vec{B}_\perp = \frac{(\vec{v} \times \vec{B}) \times \vec{v}}{v^2}, \quad (2.15)$$

$$\vec{B}_{//} = (B_s + B_z z') \hat{s}. \quad (2.16)$$

Here prime corresponds to the differentiation with respect to the coordinate s , \vec{v} is the velocity of the particle

$$\vec{v} = \frac{d\vec{r}(s)}{dt} = \frac{ds}{dt} [x' \hat{x} + (1 + \frac{x}{\rho}) \hat{s} + z' \hat{z}] \approx v(x' \hat{x} + \hat{s} + z' \hat{z}), \quad (2.17)$$

and $B_z = -\frac{B\rho}{\rho}$ with $B\rho$ as the magnetic rigidity of the particle, or equivalently, the momentum per electric charge. B_s is the longitudinal magnetic field which can be

deduced from the Maxwell equation

$$\nabla \times \vec{B} = 0, \quad (2.18)$$

or

$$\frac{\partial B_s}{\partial z} = \frac{\partial B_z}{\partial s}. \quad (2.19)$$

Thus, the transverse components and longitudinal component of the magnetic field can be expressed in terms of the particle's coordinates.

$$\vec{B}_{//} = -B\rho\left(\frac{z}{\rho}\right)', \quad (2.20)$$

$$\vec{B}_{\perp} = B\rho\left(1 - \frac{x}{\rho}\right)\left[\left(x'' - \frac{1}{\rho}\right)\hat{z} + \frac{z'}{\rho}\hat{s} - z''\hat{x}\right]. \quad (2.21)$$

By substituting Eq. (2.20) and Eq. (2.21) into Eq. (2.14) and also changing the independent variable from time t to the bending angle of the accelerator θ , i.e. $\theta = \int_0^s \frac{ds}{\rho}$, we then obtain

$$\frac{d\vec{S}}{d\theta} = \vec{S} \times \vec{F}, \quad (2.22)$$

where

$$\begin{aligned} \vec{F} &= F_1\hat{x} + F_2\hat{s} + F_3\hat{z} \\ &= [-\rho z''(1 + G\gamma)]\hat{x} + \\ &\quad [(1 + G\gamma)z' - \rho(1 + G)\left(\frac{z}{\rho}\right)']\hat{s} + \\ &\quad [-(1 + G\gamma) + (1 + G\gamma)\rho x'']\hat{z}, \end{aligned} \quad (2.23)$$

and

$$d\theta = \begin{cases} \frac{ds}{\rho} & \text{if } \rho \neq \infty \\ 0 & \text{if } \rho = \infty \text{ in straight sections} \end{cases} \quad (2.24)$$

In the frame which rotates with the particle at its cyclotron frequency, Eq. (2.22) becomes

$$\frac{d\vec{S}}{d\theta} = \vec{n} \times \vec{S}, \quad (2.25)$$

and

$$\begin{aligned} \vec{n} &= -[F_1 \hat{x} + F_2 \hat{s} + (1 + F_3) \hat{z}] \\ &= -F_1 \hat{x} - F_2 \hat{s} + [G\gamma - (1 + G\gamma)\rho x''] \hat{z}. \end{aligned} \quad (2.26)$$

The spin equation of motion in the curvilinear coordinate system is:

$$\frac{dS_1}{d\theta} = (1 + F_3)S_2 - F_2S_3, \quad (2.27)$$

$$\frac{dS_2}{d\theta} = -(1 + F_3)S_1 + F_1S_3, \quad (2.28)$$

$$\frac{dS_3}{d\theta} = F_2S_1 - F_1S_2. \quad (2.29)$$

with

$$\vec{S} = S_1 \hat{x} + S_2 \hat{s} + S_3 \hat{z}, \quad (2.30)$$

2.3.1 Differential Equation of the Spinor

Define a two component spinor so that the spin vector is

$$\vec{S} = \langle \Psi | \vec{\sigma} | \Psi \rangle = \Psi^\dagger \vec{\sigma} \Psi. \quad (2.31)$$

Then the spin equation of Eq.(2.25) can then be cast into a wave equation resembling the Schroedinger Equation,

$$\frac{d\Psi}{d\theta} = -\frac{i}{\hbar} H \Psi. \quad (2.32)$$

Following the simple algebra shown below,

$$\frac{d\vec{S}}{d\theta} = \Psi^\dagger \vec{\sigma} \frac{d\Psi}{d\theta} + \frac{d\Psi^\dagger}{d\theta} \vec{\sigma} \Psi = -\frac{i}{\hbar} \Psi^\dagger [\vec{\sigma}, H] \Psi, \quad (2.33)$$

and

$$-\frac{i}{\hbar}\Psi^\dagger[\sigma, H]\Psi = \vec{n} \times \vec{S} = \vec{n} \times (\Psi^\dagger \sigma \Psi) = -\frac{i}{2}[\vec{\sigma}, (\vec{\sigma} \cdot \vec{n})], \quad (2.34)$$

we find the spin Hamiltonians

$$H = \frac{i}{2}(\vec{\sigma} \cdot \vec{n}). \quad (2.35)$$

Thus, the equation for spin motion can be represented by the differential equation for the spinor

$$\frac{d\Psi}{d\theta} = -\frac{i}{\hbar}H\Psi = -\frac{i}{2}(\vec{\sigma} \cdot \vec{n})\Psi. \quad (2.36)$$

Neglecting the $(1 + G\gamma)\rho x''$ term in the first order approximation, Eq. (2.36) can then be simplified as

$$\frac{d\Psi}{d\theta} = -\frac{i}{2} \begin{pmatrix} G\gamma & -\xi \\ -\xi^* & -G\gamma \end{pmatrix} \Psi. \quad (2.37)$$

where $\xi = F_1 - iF_2$ couples the two eigenstates and causes depolarization. It is a function of the radial and longitudinal magnetic fields and characterizes the perturbation acting on the spin vector due to the non-vertical magnetic field.

The spinor differential equation Eq. (2.37) is solvable if the Hamiltonian H is independent of the bending angle, i.e.

$$\Psi(\theta_2) = e^{-\frac{i}{2}H(\theta_2-\theta_1)}\Psi(\theta_1) = e^{-\frac{i}{2}\nu_s\vec{\sigma}\cdot\vec{n}(\theta_2-\theta_1)}\Psi(\theta_1). \quad (2.38)$$

Here, $e^{-\frac{i}{2}\nu_s\vec{\sigma}\cdot\vec{n}(\theta_2-\theta_1)}$ is a 2×2 matrix named spin transfer matrix $t(\theta_2, \theta_1)$, i.e.

$$t = t_0 I - i(t_1 \sigma_1 + t_2 \sigma_2 + t_3 \sigma_3) = \begin{pmatrix} t_{11} & t_{12} \\ t_{21} & t_{22} \end{pmatrix} \quad (2.39)$$

with

$$t_{11} = t_0 - it_3, \quad t_{12} = -it_1 + t_2, \quad t_{22} = t_{11}^*, \quad t_{21} = -t_{12}^*, \quad (2.40)$$

where t_{11}^* and t_{12}^* are the complex conjugates of t_{11} and t_{12} .

In an accelerator, the magnetic fields are distributed piece-wise along the orbit. The spin precesses in the bending magnets and remains constant in magnetic field free regions. By multiplying the spin transfer matrices element by element, we then can map the spinor at any point along the accelerator, and the transfer matrix describing the propagation of the spinor in one turn is called the “One-Turn Matrix” given by

$$\Psi(\theta + 2\pi) = t(\theta + 2\pi, \theta)\Psi(\theta) = e^{-i\pi\nu_s\vec{\sigma}\cdot\vec{n}}\Psi(\theta). \quad (2.41)$$

From this equation, one can conclude

- In a perfect accelerator, the off diagonal term ξ in the spinor differential equation vanishes and $\Psi(\theta + 2\pi) = e^{-i\pi\nu_s\sigma_3}\Psi(\theta)$. Any spin vector deviating from the vertical direction precesses about the vertical axis while the spin vector which stays in the vertical direction reproduces itself in every successive turn. The vertical axis is called the “spin closed orbit”.
- In the presence of any non-vertical magnetic fields, the spin closed orbit is perturbed away from the vertical direction and the spin tune is modified. The spin vector coinciding with the vector \vec{n} in Eq. (2.26) becomes the spin closed orbit and any other spin vectors different from this direction precess around this axis \vec{n} . Since the perturbation from the error fields is usually small, the spin closed orbit \vec{n} is nearly vertical and the spin tune is approximately $G\gamma$.
- In an accelerator with a relatively strong local error field such as spin rotators and Siberian snakes but otherwise perfect, the simple relation of the spin tune with the beam energy is broken. In this case, the one turn spin transfer matrix is given by

$$M = e^{-i\frac{G\gamma(2\pi-\theta)}{2}\sigma_3} M_{\text{error}} e^{-i\frac{G\gamma\theta}{2}\sigma_3}, \quad (2.42)$$

where θ is the particle orbital angle from the observation point to the error field. For example, considering a simple rotator with axis \hat{n}_e and spin precession angle ψ , The spin transfer matrix of the error field is

$$M_{\text{error}} = e^{-i\frac{\psi}{2}\vec{\sigma}\cdot\hat{n}_e} = \cos\frac{\psi}{2} - i\vec{\sigma}\cdot\hat{n}_e\sin\frac{\psi}{2}, \quad (2.43)$$

with

$$\hat{n}_e = \cos\chi_1\hat{x} + \cos\chi_2\hat{s} + \cos\chi_3\hat{z}. \quad (2.44)$$

The one turn spin transfer map becomes

$$M = e^{-i\pi\nu_s\hat{n}_{co}\cdot\vec{\sigma}}, \quad (2.45)$$

where the spin closed orbit \hat{n}_{co} is no longer along the vertical direction and is given by

$$\cos\pi\nu_s = \cos G\gamma\pi\cos\frac{\psi}{2} - \sin G\gamma\pi\sin\frac{\psi}{2}\cos\chi_3, \quad (2.46)$$

$$\begin{aligned} \hat{n}_{co} = & \frac{[\cos G\gamma(\pi - \theta)\cos\chi_1 - \sin G\gamma(\pi - \theta)\cos\chi_2]\sin\frac{\psi}{2}}{\sin\pi\nu_s}\hat{x} \\ & + \frac{[\cos G\gamma(\pi - \theta)\cos\chi_2 - \sin G\gamma(\pi - \theta)\cos\chi_1]\sin\frac{\psi}{2}}{\sin\pi\nu_s}\hat{s} \\ & + \frac{\sin G\gamma\pi\cos\frac{\psi}{2} + \cos G\gamma\pi\sin\frac{\psi}{2}\cos\chi_3}{\sin\pi\nu_s}\hat{z}. \end{aligned} \quad (2.47)$$

As an example, for a spin rotator with the axis in the horizontal plane $\cos\chi_3 = 0$ and finite spin rotation angle ψ , the spin precession tune is always a non-integer number because

$$\cos\pi\nu_s = \cos G\gamma\pi\cos\frac{\psi}{2}. \quad (2.48)$$

Furthermore, the spin precession will become energy independent if the spin rotation angle ψ is equal to 180° . These properties are very useful in spin manipulations and provide us the methods of preserving the beam polarization in accelerators. We will discuss these in the next section of this chapter.

2.3.2 Spin Depolarization Resonance and Corrections

The differential equation for the spinor Ψ obtained in Section 2.3.1 describes the evolution of the spin vector in synchrotrons. In a first order approximation, the differential equation is given by Eq. (2.37). The off-diagonal term $\xi = F_1 - iF_2$ describes the driving force of the spin resonance and is a function of non-vertical magnetic fields sampled by the particle. In the presence of non-vertical magnetic field, ξ is non-zero and the spin motion is perturbed from its normal precession around the main guiding fields. It can also be expressed in terms of particle coordinates, i.e.

$$F_1 = -\rho z''(1 + G\gamma)\hat{x} \quad (2.49)$$

$$F_2 = (1 + G\gamma)z' - \rho(1 + G)\left(\frac{z}{\rho}\right)' \hat{s} \quad (2.50)$$

Since the particle coordinates are periodic or quasi-periodic functions of the bending angle θ , ξ can be expanded in Fourier series.

$$\xi = \sum_k \epsilon_k e^{-ik\theta}, \quad (2.51)$$

where k is the location of the spin resonance called spin resonance tune. The amplitude of the Fourier expansion ϵ_k describes the spin resonance strength. It also measured the width of the resonance, as the perturbation acting on the spin vector is negligible if the difference between the spin precession frequency and the frequency at which the perturbing field kicks the spin vector is larger than ϵ_k . When the spin motion is off resonance, the perturbation on the spin motion is incoherent with the spin precession and the total kicks on the spin vector are averaged to zero. On the contrary, when the two frequencies coincide with each other, the kicks on the spin vector add up coherently and lead to a continuous spin rotation about the perturbing field. Then the spin motion is on resonance. The stronger the perturbing field, the greater the kick acting on the spin vector and the wider the spin resonance.

In terms of the non-vertical magnetic fields, the resonance strength ϵ_k is given by

$$\epsilon_k = \frac{1}{2\pi} \oint \left[(1 + G\gamma) \frac{\Delta B_x}{B\rho} + (1 + G) \frac{\Delta B_{\parallel}}{B\rho} \right] e^{ik\theta} ds. \quad (2.52)$$

It can also be expressed in terms of particle betatron coordinates, i.e.

$$\epsilon_k = -\frac{1}{2\pi} \oint \left[(1 + G\gamma)(\rho z'' + iz') - i\rho(1 + G)\left(\frac{z}{\rho}\right)' \right] e^{ik\theta} ds. \quad (2.53)$$

The perturbing field comes from the dipole roll, quadrupole misalignment, higher order multipoles, the betatron motion and the off momentum closed orbit. The synchrotron motion can also cause sidebands around the primary spin resonance by modulating the spin precession frequency. Based on the sources of spin resonance, the spin resonances can be categorized into imperfection resonances, intrinsic resonances and resonances due to high order effects.

Imperfection spin resonance

These resonances are driven by the dipole fields sampled by the distorted vertical closed orbit due to the tilts of bending magnets and the misalignment of quadrupoles. Since the error fields repeat themselves after the particle completes one revolution around the accelerator, they will then coherently perturb the spin motion in every revolution if the spin vector precesses an integer number of turns around its closed orbit and reproduces itself after one revolution. Thus, a spin resonance occurs at

$$G\gamma = \text{integer} \quad (2.54)$$

where $G\gamma$ is the spin precession tune and the imperfection spin resonance strength is proportional to the vertical closed orbit distortion. Since the distortion of the vertical closed orbit is sensitive to the harmonics near the vertical betatron tune ν_z , the imperfection resonances near $G\gamma = kP + [\nu_z]$ are the most important ones, where each superperiod contributes constructively. Here, k is an integer, P is the number of

superperiods in the accelerator and $[\nu_z]$ is the nearest integer to the vertical betatron tune.

Intrinsic spin resonance

This type of resonance is driven by the vertical focusing fields of quadrupole magnets, and the resonance condition is related with the vertical betatron tune. For an ideal synchrotron composed of P superperiods, the intrinsic resonance happens at

$$G\gamma = kP \pm \nu_z \quad (2.55)$$

where k is an integer and ν_z is the vertical betatron tune. The intrinsic spin resonance strength is proportional to the amplitude of the vertical betatron oscillation. For example, the AGS is composed of 12 superperiods with 5 FODO cells per superperiod and the intrinsic spin resonances in the AGS are: $G\gamma = 0 + \nu_z$, $G\gamma = 12 \pm \nu_z$, $G\gamma = 36 \pm \nu_z$, $G\gamma = 48 \pm \nu_z$ and $G\gamma = 60 - \nu_z$. Among them, the most important spin resonances are at $G\gamma = 60 - \nu_z$ because the contributions from quadrupoles in every FODO cell are in phase. The following table 5.2 lists the AGS intrinsic spin resonances which will be encountered during the polarized proton acceleration up to 30 GeV/c. The last column of Table 5.2 is calculated based on the Froissart-Stora Formula averaged for a beam with 15 π (95%, normalized) vertical emittance. The Froissart-Stora Formula will be addressed in Section 2.3.3.

Other spin resonances

Besides the imperfection spin resonance and intrinsic spin resonance, there are also other mechanisms which can drive spin depolarization resonances at certain conditions. For example, the synchrotron motion which modulates the beam energy at the synchrotron tune ν_s can lead to sidebands around the primary spin resonances, i.e. $G\gamma = k \pm m\nu_s$ [6]. Here, k and m are integers. Other spin resonances may also

Table 2.1: Intrinsic resonance strengths for the AGS

resonance strength	intrinsic spin resonance	effect on beam polarization
very strong	$60 - \nu_z$	more than 90% spin flip
strong	$0 + \nu_z, 36 \pm \nu_z$	partial spin flip
medium	$12 + \nu_z$	about 75% beam polarization loss
weak	$48 \pm \nu_z$	5% - 10% beam polarization loss
negligible	$24 \pm \nu_z$	less than 5% polarization loss

arise from the linear coupling between horizontal and vertical betatron motions or the sextupole fields experienced by the beam.

In summary, a spin resonance condition can be generally expressed as

$$\nu = k + k_x \nu_x + k_z \nu_z + k_s \nu_s. \quad (2.56)$$

where k , k_x , k_z and k_s are integers, ν_x is the horizontal betatron tune, ν_z is the vertical betatron tune and ν_s is the synchrotron tune.

2.3.3 Effect of Crossing a Single Isolated Spin Resonance – Froissart-Stora Formula

The evolution of the beam polarization when crossing a single spin resonance was studied by Froissart and Stora [10]. They obtained a solution of the spinor equation in terms of the confluent hypergeometric function by assuming the spin resonance is crossed at a constant rate α , where

$$\alpha = \frac{dG\gamma}{d\theta}. \quad (2.57)$$

The asymptotic form of this solution is the Froissart-Stora formula

$$\frac{P_f}{P_i} = 2e^{-\frac{\pi|\epsilon_k|^2}{2\alpha}} - 1. \quad (2.58)$$

P_i corresponds to the polarization long before the spin resonance, or $\theta = -\infty$. P_f is the polarization long after the spin resonance, or $\theta = \infty$. The effect of a spin resonance on the beam polarization is determined by the resonance strength ϵ_k and the resonance crossing rate α . For weak resonances, the beam polarization can be maintained, i.e. $P_f/P_i \approx 1$, if the resonance is crossed at such a high speed that $\frac{\pi|\epsilon_k|^2}{\alpha} \ll 1$. Strong resonances, on the other hand, can produce a full spin flip, i.e. $P_f/P_i \approx -1$ if the resonance crossing rate fulfills the condition $\frac{\pi|\epsilon_k|^2}{\alpha} \gg 1$. Any case in between gives partial or even full depolarization.

Since imperfection resonances are related to the vertical closed orbit distortion which is the same for different particles in a beam, the effect of crossing an imperfection resonance is directly given by Eq. (2.58). For spin resonances which are proportional to the betatron oscillation amplitude, the resonance strength is different for particles oscillating at different amplitudes, such as intrinsic spin resonances. Therefore in synchrotrons, the polarization for a beam composed of particles with different betatron amplitudes and phases after passing through the resonance is to average Eq. (2.58) over the particles' distribution.

$$\left\langle \frac{P_f}{P_i} \right\rangle = \int_0^\infty [2e^{\pi|\epsilon(I)|^2/2\alpha} - 1] \rho(I) dI, \quad (2.59)$$

where I is the action of the particle, and $\rho(I)$ is the distribution function with

$$\int_0^\infty \rho(I) dI = 1. \quad (2.60)$$

The intrinsic resonance strength for a particle is proportional to the betatron oscillation amplitude, or equivalently, to the square root of its action, i.e.

$$|\epsilon(I)|^2 = |\epsilon(I_0)|^2 \frac{I}{I_0}. \quad (2.61)$$

For a beam with Gaussian distribution $\rho(I)$

$$\rho(I) = \frac{1}{2I_0} e^{-I/2I_0}, \quad (2.62)$$

where $I_0 = \varepsilon_{rms}/2$ is the action corresponding to the rms beam emittance ε_{rms} , the beam polarization ratio is then

$$\left\langle \frac{P_f}{P_i} \right\rangle = \frac{1 - \pi |\epsilon(I_0)|^2 / \alpha}{1 + \pi |\epsilon(I_0)|^2 / \alpha}. \quad (2.63)$$

This effect actually weakens the efficiency of slowly crossing strong intrinsic spin resonances to obtain a full spin flip and causes the depolarization. Thus, new methods should be developed to overcome intrinsic spin resonances.

2.3.4 Spin Resonance Correction

In accelerating polarized beams to high energies, one generally encounters numerous spin resonances, and proper ways of manipulating spin are needed to prevent loss of beam polarization. Depending on the mechanism which drives the spin resonances, the method of avoiding depolarization can vary for different types of spin depolarization resonances.

Imperfection resonance correction

For an imperfection resonance which stems from a distorted closed orbit, the most direct way of avoiding this type of resonances is to use harmonic correctors to eliminate the closed orbit distortion. This method has been used in early polarized proton accelerations [2]. However, this method involves a large amount of machine tuning and also is very hard to make routine because the closed orbit is sensitive to a change of temperature, power fluctuation, tide, etc. This makes the acceleration of high energy polarized protons very difficult.

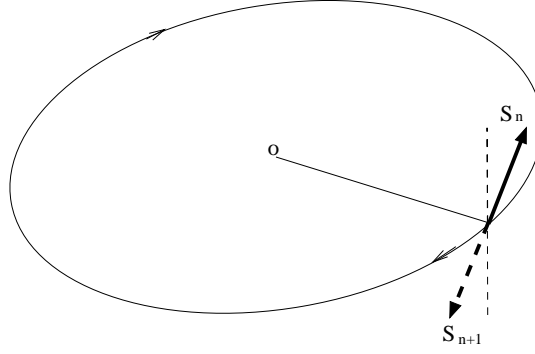


Figure 2.2: With a single full snake in the ring, the spin vector is flipped when the particle finishes one revolution. Thus, the kick acted on the spin vector from the perturbation field will cancel the kick the spin vector received in the previous turn.

The method of using a Siberian snake, on the other hand, is independent of the closed orbit and operationally easier. The idea is to use longitudinal or transverse magnetic fields to rotate the stable spin direction by 180° . The perturbation on the spin from the accelerator lattice is canceled in successive turns. Compared with the harmonic correction method, this is a more practical method for high energy polarized proton acceleration.

Based on the spin rotation angle, a snake is described as either a full snake which rotates the spin vector by 180° or a partial snake for which the rotation angle of the spin vector is less than 180° . A full snake is a powerful tool for overcoming not only the imperfection resonances but other types of spin resonances as well. This is because any perturbation on the spin vector irrespective of its origin will be canceled in the next turn when the spin vector is 180° away from its direction in the previous turn as shown in Fig. 2.2. Thus, the beam polarization should be maintained in an accelerator with a full snake installed. This was first demonstrated in the polarized proton acceleration experiment in the IUCF cooler ring [4].

A partial snake, on the other hand, can overcome an imperfection resonance by

moving the spin precession tune away from integers. Thus, breaking the condition of the imperfection resonances (See Eq. (2.48)). Although the partial snake can only correct the imperfection resonances and leaves the intrinsic spin resonances uncorrected, it is a useful method for medium energy synchrotron where a full snake is not a practical solution like in the AGS because of cost or space constraints. This method was successfully tested at the Brookhaven AGS [11, 12].

Intrinsic resonance correction

Intrinsic spin resonances are driven by the vertical focusing fields arising from the beam betatron motion, an intrinsic feature of particles circulating in a synchrotron. One way to avoid depolarization from this resonance is the tune jump method [2, 12], i.e. to change the betatron tune abruptly when the spin resonance is approached. In this case, the effective resonance crossing rate is greatly enhanced and the effect of the spin resonance can be minimized. The betatron tune can be jumped with quadrupoles which can react in a very short time. Fig. 2.3 illustrates how this method works.

This method involves non-adiabatic beam manipulations and can cause beam emittance dilution. This effect could affect the machine operation and also worsen the beam condition when crossing spin resonances at higher energies. Beside the tune jump method, the polarization can also be maintained by ramping through the resonance slowly enough so that all the particles will follow the spin stable direction and induce a full spin flip. However, since a beam is composed of particles with different betatron amplitudes, core particles experience less perturbations than the edge particles, the efficiency of slow ramping method is reduced as shown in Eq. (2.63). The alternative way to achieve a full spin flip under nominal acceleration rate is to let the whole beam coherently oscillate at a large amplitude and the average magnetic field experienced by the beam is greatly enhanced.

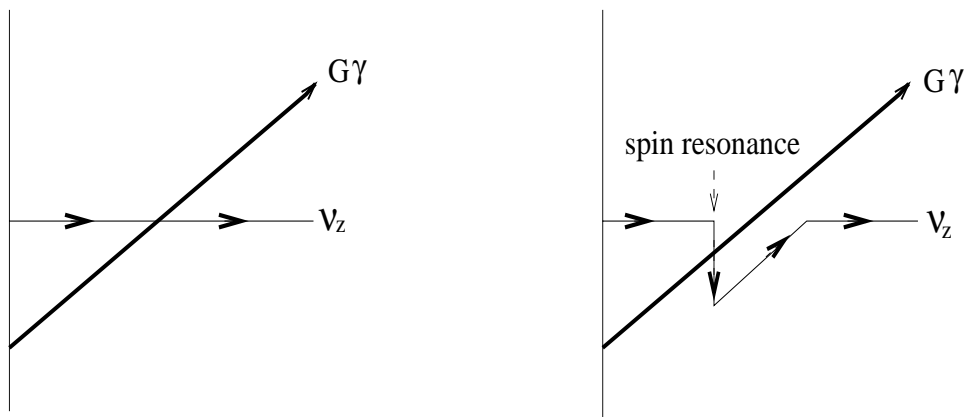


Figure 2.3: The left part corresponds to the betatron tune and $G\gamma$ change during a normal acceleration cycle. The right part shows the betatron tune is jumped through the spin resonance and then ramped back to its nominal value.

This method was also first tested at the IUCF cooler ring [14]. A pulsed kicker was employed to enhance the betatron oscillation. Unlike IUCF, the AGS does not have an emittance cooling system and the betatron oscillation induced by the pulsed kicker would decohere quickly because of the tune spread due to the inherent nonlinear effect, and result in the beam emittance blow up which we certainly want to avoid.

Chapter 3

RF Dipole - A Novel Solution For Intrinsic Spin Resonances

An RF dipole is a device which provides an oscillating magnetic field. In synchrotrons, under the influence of an external driving force oscillating at a frequency close to the intrinsic betatron oscillation frequency, all particles will be forced to oscillate at the driving frequency. The oscillation amplitude is then determined by the strength of the external driving force, and a large coherent oscillation can be induced. If the excitation process is adiabatic, the beam size will not be disturbed. Unlike the pulsed kicker method, using an RF dipole to adiabatically excite a coherent oscillation allows one to control its amplitude and duty time.

In the presence of an RF dipole with a horizontally oriented magnetic field, the differential equation of the vertical betatron motion is given by

$$z'' + k_z(s)z = -\frac{\Delta B_x}{B\rho}, \quad (3.1)$$

where z is the vertical betatron coordinate, the prime corresponds to the derivative with respect to the longitudinal coordinate s , $k_z(s)$ is the focusing function, and

$$\Delta B_x = \Delta B_m \cos \nu_m \theta$$

is the RF dipole magnetic field with ν_m as the modulation tune defined as the ratio of the RF dipole oscillating frequency f_m to the revolution frequency f_0 around the accelerator, θ is the azimuthal angle along the ring. The corresponding Hamiltonian is given by

$$H = \frac{1}{2}z'^2 + \frac{1}{2}K_z z^2 + \frac{\Delta B_m}{B\rho} z \cos \nu_m \theta. \quad (3.2)$$

Using the generating function F_1 ,

$$F_1 = -\frac{z^2}{2\beta_z} \left(\tan \phi_z - \frac{\beta_z}{2} \right), \quad (3.3)$$

where $\beta_z(s)$ is the betatron amplitude function, $\phi_z(s)$ is the new conjugate phase coordinate, the canonical transformation is given by

$$z = \sqrt{2\beta_z I_z} \cos \phi_z, \quad p_z = \alpha_z z + \beta_z z' = -\sqrt{2\beta_z I_z} \sin \phi_z.$$

Here I_z and ϕ_z are conjugate action-angle phase space coordinates. The new Hamiltonian becomes

$$H(I_z, \phi_z) = \frac{I}{\beta_z} + \frac{\Delta B_m}{B\rho} \sqrt{2\beta_z I_z} \cos \phi_z \cos \nu_m \theta, \quad (3.4)$$

where s is still serving as the time variable.

Using the generating function

$$F_2 = (\phi_z - \mu_z + \nu_z \theta) J_z, \quad \mu_z(s) = \int_0^s \frac{ds}{\beta_z},$$

where J_z and $\psi_z = \phi_z - \mu_z(s) + \nu_z \theta$ are conjugate phase space coordinates, and using the orbit angle $\theta = s/R$ as the time variable, the new Hamiltonian becomes

$$H(J_z, \psi_z) = \nu_z J_z + \frac{R\Delta B_m}{B\rho} \sqrt{2\beta_z J_z} \cos(\psi_z + \mu_z - \nu_z \theta) \cos \nu_m \theta, \quad (3.5)$$

where R is the mean radius of the accelerator.

Since ΔB_m and $\mu_z(s) - \nu_z \theta$ are periodic function of θ , the Hamiltonian of Eq. (3.5) can be expanded in Fourier series:

$$H(J_z, \psi_z) = \nu_z J_z + \frac{1}{2} \sum_n \sqrt{2J_z} [C_{n+} e^{i(\psi_z - n\theta)} + C_{n-} e^{-i(\psi_z + n\theta)}] \cos \nu_m \theta, \quad (3.6)$$

where we have

$$C_{n+} = \frac{1}{2\pi} \int_0^{2\pi R} \frac{\Delta B_m}{B\rho} \sqrt{\beta_z} e^{i(\mu_z - \nu_z \theta)} e^{in\theta} ds, \quad (3.7)$$

$$C_{n-} = \frac{1}{2\pi} \int_0^{2\pi R} \frac{\Delta B_m}{B\rho} \sqrt{\beta_z} e^{-i(\mu_z - \nu_z \theta)} e^{in\theta} ds. \quad (3.8)$$

In particular, a localized RF dipole will produce all integer harmonics in the Fourier expansion.

The betatron resonance condition is given by $\nu_m = n \pm \nu_z$. For example, at $\nu_z \approx 8.7$, the resonance condition can be fulfilled by $\nu_m \approx 0.3$ with $n = 9$. At a resonance condition $\nu_m = n \pm \nu_z$, we need to retain only the resonance term

$$H(J_z, \psi_z) \approx \nu_z J_z + \frac{1}{2} \sqrt{2J_z} |C_{\text{eff}}| \cos(\psi_z - n\theta + \nu_m \theta + \chi), \quad (3.9)$$

where χ is the phase of the resonance strength, and

$$|C_{\text{eff}}| = \frac{\Delta B \Delta L}{2\pi B\rho} \sqrt{\beta_z} \quad (3.10)$$

with the integrated rf dipole field strength $\Delta B \Delta L = \int \Delta B_m ds$.

We now transform the phase space into the resonance rotating frame by using the generating function

$$F_2 = (\psi_z - n\theta + \nu_m \theta + \chi) J, \quad (3.11)$$

and the new Hamiltonian becomes

$$H(\psi, J) = \delta J + \frac{1}{2} |C_{\text{eff}}| \sqrt{2J} \cos \psi. \quad (3.12)$$

where $\delta = \nu_z - (n - \nu_m)$ is the resonance proximity parameter, $J = J_z$ and $\psi = \psi_z - n\theta + \nu_z\theta + \chi$.

The fixed points of the resonance Hamiltonian are given by

$$\dot{J} = -\frac{\partial H}{\partial \psi} = 0, \quad \dot{\psi} = \frac{\partial H}{\partial J} = 0. \quad (3.13)$$

We obtain $\psi_{\text{FP}} = 0$ or π and

$$\delta \pm \frac{1}{2}C_{\text{eff}}(2J)^{-\frac{1}{2}} = 0, \quad \text{or} \quad J = \frac{1}{2}\left(\frac{C_{\text{eff}}}{2\delta}\right)^2, \quad (3.14)$$

where the plus sign corresponds to $\psi_{\text{FP}} = 0$, and minus sign to $\psi_{\text{FP}} = \pi$. In this case, there is only one fixed points because the fixed point amplitude of $\psi_{\text{FP}} = 0$ is the negative of the fixed point amplitude of $\psi_{\text{FP}} = \pi$. From Eq. (3.14), the coherent betatron amplitude is found to be

$$Z_{\text{coh}} = \frac{\Delta B_m L}{4\pi B \rho \delta} \beta_z \quad (3.15)$$

Eq. (3.15) can also be easily obtained without going through the seemingly complicated Hamiltonian approach by studying the motion in a phase space frame which is rotating at the RF dipole oscillating frequency.

Consider a particle influenced by a single horizontally oriented RF dipole field of length L at a location in the accelerator where the vertical betatron amplitude function is β_z , the net rotation angle per turn of a particle's phase space vector in the rotating frame is $2\pi\delta$, with $\delta \equiv \nu_z - (k - \nu_m)$ where k is an integer and ν_z is the vertical betatron tune. The RF dipole field deflects the trajectory through an angle $\theta = \Delta B_x L / (B\rho)$. Since the dipole field is oscillating at the same frequency as the rotating frame, the time average change of Z' in this frame is just half the amplitude of the modulated angular deflection:

$$\langle Z' \rangle = \frac{1}{2}(\Delta B_m \ell) / (B\rho) \equiv \frac{1}{2}\theta_0. \quad (3.16)$$

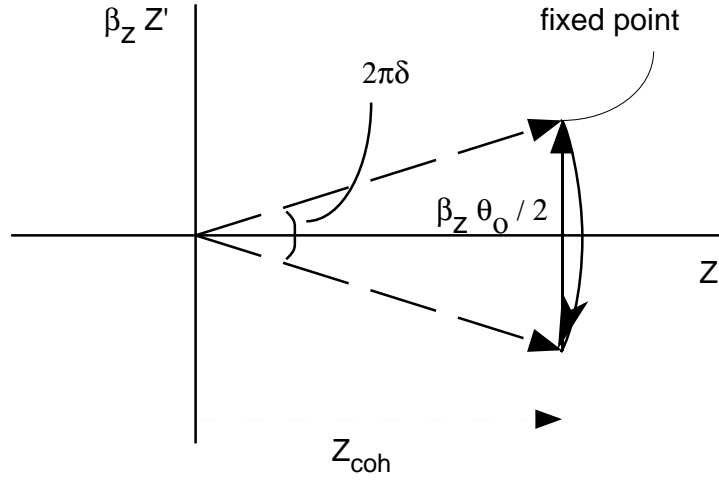


Figure 3.1: Phase space motion in the rotating frame at the maximum betatron amplitude location.

Therefore, the coherent betatron oscillation amplitude is given by

$$2\pi\delta \cdot Z_{\text{coh}} = \langle Z' \rangle \beta_z, \quad (3.17)$$

and

$$Z_{\text{coh}} = \frac{\Delta B_m \ell}{4\pi B \rho \delta} \beta_z, \quad (3.18)$$

which is the same as Eq. (3.15). It shows that the coherent betatron oscillation amplitude is proportional to the maximum dipole field strength and inversely proportional to the resonance proximity parameter δ .

3.1 The Non-linear Detuning Effect

In accelerators with linear magnetic fields, the betatron tune is an invariant with respect to the betatron oscillation amplitude. However, this is not true any more if there are higher order magnetic field in the machine as well. In the presence of

octupole magnet or the second order effect of sextupole magnets, the betatron tune then becomes dependent on the oscillation amplitude, i.e.

$$\nu_z = \nu_{z0} + \frac{Z_{\text{coh}}^2}{2\beta_z} \alpha_{zz} \quad (3.19)$$

Here, z stands for the vertical plane. For horizontal motion, there is a similar relation. $\alpha_{zz} = \frac{\beta_z^2}{16\pi B\rho} \sum_i (B''' \Delta L)_i$ is the vertical detuning coefficient and B''' is the strength function of the octupole. Eq. (3.19) is obtained assuming no linear coupling between the horizontal plane and the vertical plane. If this exists, the vertical betatron tune then becomes dependent on the horizontal betatron oscillation amplitude as well. Since in most of the cases the coupling effect is small, we will not involve this effect into the calculation for simplification.

The non-linear detuning due to octupoles or the second order effect of sextupoles would change the characteristic of the particle's response. To study this, we start from the Hamiltonian (Eq. (3.12)) by adding a non-linear betatron detuning term. The new Hamiltonian becomes

$$H(\psi, J) = \delta J + \frac{1}{2} \alpha_{zz} J^2 + \frac{1}{2} |C_{\text{eff}}| \sqrt{2J} \cos \psi, \quad (3.20)$$

where the detuning parameter α_{zz} can come from octupole magnets to first order or the second order effect of sextupole magnets.

The fixed points of the resonance Hamiltonian are given by

$$\dot{J} = -\frac{\partial H}{\partial \psi} = 0, \quad \dot{\psi} = \frac{\partial H}{\partial J} = 0. \quad (3.21)$$

Equation (3.21) gives $\psi_{\text{FP}} = 0$ or π and

$$\delta + \alpha_{zz} J + \frac{1}{2} C_{\text{eff}} (2J)^{-\frac{1}{2}} \cos \psi_z = 0. \quad (3.22)$$

Defining the parameter $w = \sqrt{2J} \cos \psi_{\text{FP}}$, the equation for the fixed point becomes

$$w^3 + \frac{2\delta}{\alpha_{zz}} w + \frac{C_{\text{eff}}}{\alpha_{zz}} = 0. \quad (3.23)$$

Letting the resonance strength parameter a and the resonance proximity b be

$$a = 2 \frac{C_{\text{eff}}}{\alpha_{zz}}, \quad b = -\frac{2\delta}{\alpha_{zz}},$$

Eq. (3.22) is simplified to

$$w^3 - bw + \frac{1}{2}a = 0, \quad (3.24)$$

which has three solutions for $b \geq b_b = 3(\frac{a}{4})^{\frac{2}{3}}$ given by

$$w_1 = -\frac{2}{\sqrt{3}}b^{\frac{1}{2}}\cos\frac{\xi}{3}, \quad (3.25)$$

$$w_2 = \frac{2}{\sqrt{3}}b^{\frac{1}{2}}\sin(\frac{\pi}{6} - \frac{\xi}{3}), \quad (3.26)$$

$$w_3 = \frac{2}{\sqrt{3}}b^{\frac{1}{2}}\sin(\frac{\pi}{6} + \frac{\xi}{3}), \quad (3.27)$$

with $\xi = \arctan \sqrt{(b/b_b)^3 - 1}$. Here w_1 and w_2 are stable fixed points (SFP) and w_3

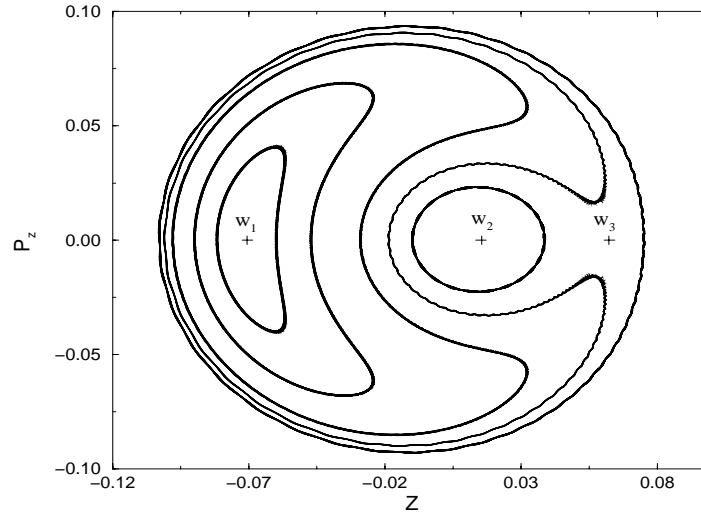


Figure 3.2: The phase space in the resonant frame which rotates with the modulation tune ν_m .

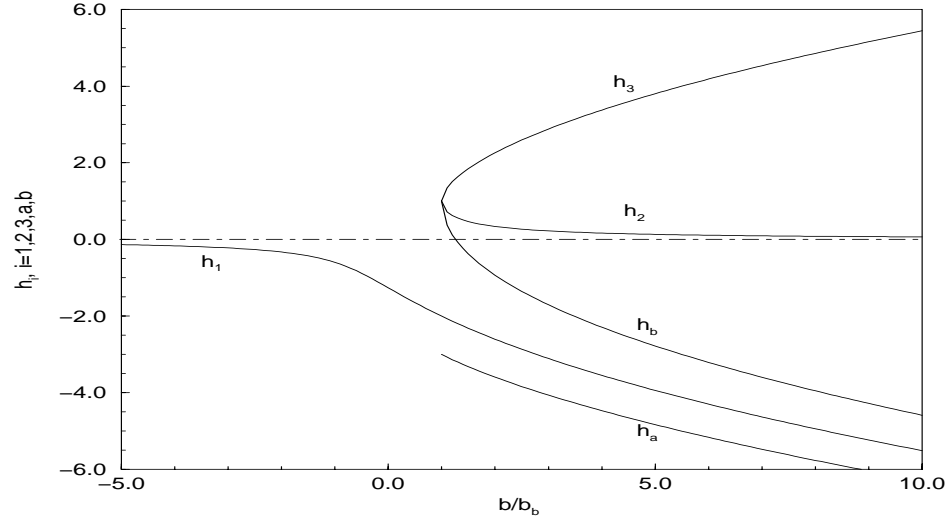


Figure 3.3: The fixed points in the normalized coordinate as a function of the modulation frequency parameter b/b_b .

is the unstable fixed point (UFP) as shown in Fig. 3.2.

Using the normalized coordinates with

$$h_i = \sqrt{\frac{3}{b_b}} w_i$$

for $i = 1, 2, 3$. The two islands are separated by the separatrix which goes through the UFP. The intercepts of the separatrix with the betatron coordinate are given by

$$h_a = -h_3 - \frac{2}{\sqrt{h_3}} \quad (3.28)$$

$$h_b = -h_3 + \frac{2}{\sqrt{h_3}}. \quad (3.29)$$

Figure 3.3 shows the fixed points of resonance islands and the intercepts of the separatrix with a phase space coordinate as a function of the modulation frequency parameter b/b_b .

3.2 The Effect On The Spin Motion

For a single particle, its intrinsic spin resonance strength is linearly proportional to the betatron oscillation amplitude. A bigger oscillation amplitude corresponds to a stronger intrinsic spin resonance and results in a greater rotation of the spin vector after crossing the spin resonance. Based on the Froissart-Stora formula [see Eq. (2.58)], if the resonance strength could be enhanced to such a point that under the nominal acceleration rate $\frac{\pi|\epsilon_0|^2}{\alpha} \gg 1$, a full spin flip then can be obtained.

In reality, particles are distributed at different oscillation amplitudes in a beam and experience different focusing fields in the quadrupoles. Particles at the edge of the beam sample stronger focusing fields and have a greater spin rotation than particles in the core of the beam. The effect of the intrinsic spin resonance on the beam polarization is the ensemble average of the Froissart-Stora formula over all the particles. For a beam with Gaussian distribution, the beam polarization is given by Eq. (2.63). By forcing the whole beam to coherently oscillate at a larger amplitude, particles close to the core of the beam experience greater magnetic fields and the spin resonance strength for the beam is effectively enhanced.

For a coherent oscillation at the same frequency as the betatron oscillation with amplitude Z_{coh} , the ratio of the final polarization after crossing the resonance to the polarization before crossing the resonance becomes

$$\frac{P_f}{P_i} = \int (2e^{-\frac{\pi|\epsilon|^2}{2\alpha}} - 1) \rho(z, p_z) dz dp_z, \quad (3.30)$$

where $\rho(z, p_z)$ is the beam distribution function. For a Gaussian beam distribution, we have

$$\rho(z, p_z) = \frac{1}{2\pi\sigma_z^2} e^{-\frac{(z-z_{\text{coh}})^2 + p_z^2}{2\sigma_z^2}} \quad (3.31)$$

$z = \sqrt{2\beta_z J} \cos \psi$ and $p_z = -\sqrt{2\beta_z J} \sin \psi$ are the particle's coordinates. J is the action and ψ is the phase advance. ϵ is the spin resonance strength of particle with

action J , i.e.

$$\epsilon = \epsilon_0 \sqrt{\frac{2J}{\epsilon_0}} = \epsilon_0 \frac{z_{\text{coh}}}{\sigma_z} \quad (3.32)$$

where ϵ_0 is the resonance strength for beam with rms emittance ϵ_0 and σ_z is the corresponding rms beam size.

Express $\rho(z, p_z)$ with the action and phase variables J and ψ , we have

$$\rho(J, \psi) = \frac{1}{\epsilon_0} e^{-\frac{J+J_{\text{coh}}}{\epsilon_0}} e^{\frac{2\sqrt{J_{\text{coh}}J}}{\epsilon_0} \cos \psi} \quad (3.33)$$

where $J_{\text{coh}} = \frac{Z_{\text{coh}}^2}{2\beta_z}$. After integrated over the phase, we then get

$$\rho(J) = \frac{1}{\epsilon_0} e^{-\frac{J+J_{\text{coh}}}{\epsilon_0}} I_0\left(\frac{2\sqrt{J_{\text{coh}}J}}{\epsilon_0}\right) \quad (3.34)$$

and

$$\int_0^\infty \rho(J) dJ = 1, \quad (3.35)$$

with $I_0(\frac{2\sqrt{J_{\text{coh}}J}}{\epsilon_0})$ as the modified Bessel function. By putting Eq. (3.32) and Eq. (3.34) into Eq. (3.30), we then obtain

$$\frac{P_f}{P_i} = \frac{2}{1 + \pi|\epsilon_0|^2/\alpha} \exp \left\{ -\frac{(Z_{\text{coh}}^2 \hat{\beta}_z / 2\beta_z \sigma_z^2)(\pi|\epsilon_0|^2/\alpha)}{1 + \pi|\epsilon_0|^2/\alpha} \right\} - 1 \quad (3.36)$$

On the other hand, Eq. (3.15) shows that a particle would be unstable if the RF dipole frequency coincides with the betatron oscillation frequency. Therefore, in accelerators with negligible non-linear magnetic fields in order to maintain the stability of the beam, the RF dipole frequency should be slightly away from the intrinsic betatron frequency. Due to this effect, the presence of the RF dipole then artificially introduces an extra spin resonance close to the intrinsic resonance.

The strength of this artificial spin resonance could come from two effects. One is the effect that all the particles coherently oscillate at a large amplitude and experience

the focusing fields in quadrupoles along the ring. This effect is identical to the intrinsic spin resonance and the corresponding spin resonance strength is the intrinsic spin resonance strength enhanced by the factor of the ratio of the coherent oscillation amplitude to the normal betatron oscillation amplitude, i.e.

$$\epsilon_{\text{coh}} = \epsilon_0 \frac{Z_{\text{coh}}}{\sigma_z}. \quad (3.37)$$

where ϵ_0 is the intrinsic resonance strength for beam with rms size σ_z .

The other effect is from the magnet itself. The spin resonance strength of the RF dipole can be calculated from the Thomas-BMT equation, i.e.

$$\epsilon_{\text{rf}} = \frac{1 + G\gamma}{4\pi B\rho} \int B dl. \quad (3.38)$$

However, the strength of this spin resonance is normally very weak compared to the intrinsic spin resonance strength. For instance, for an RF dipole with maximum field 20 Gauss-m, the resonance strength $\epsilon_{\text{rf}} = 1.04 \times 10^{-4}$ at $G\gamma = 8.7$ and the intrinsic spin resonance strength in the AGS is 0.0075 for a beam with 15π normalized 95% emittance at $G\gamma = 0 + \nu_z = 8.7$. Here, ν_z is the vertical betatron tune which is normally set as 8.7 in the AGS.

The most simple case is that the two spin resonances are well separated. In this case, the final beam polarization is

$$\frac{P_f}{P_i} = \frac{1 - \pi|\epsilon_0|^2/\alpha}{1 + \pi|\epsilon_0|^2/\alpha} \left(2 \exp \left\{ -\frac{Z_{\text{coh}}^2 \hat{\beta}_z}{\beta_z \sigma_z^2} \frac{\pi|\epsilon_0|^2}{2\alpha} \right\} - 1 \right). \quad (3.39)$$

However, more generally, the two spin resonances overlap with each other and the final polarization will then depend on the relative phase between the resonances. In this case, it is very difficult to obtain the final polarization analytically and a numerical simulation of tracking the beam polarization in the presence of an RF dipole magnet is needed.

Chapter 4

Experimental Apparatus

The polarized proton acceleration complex at Brookhaven National Laboratory consists of an atomic H^- source, Linear accelerator, Booster and AGS (Alternating Gradient Synchrotron) as shown in Figure 4.1. Polarized beam from the source was accelerated by the 200 MeV LINAC (Linear Accelerator) and strip injected into the Booster. At the end of the LINAC, the beam polarization was measured by a 200 MeV polarimeter. The polarized beam was injected into the AGS at $G\gamma = 4.7$ ($2.27\text{ GeV}/c$) and accelerated to the desired final energy. Table (4) lists the AGS and Booster parameters.

In the experiment, the RF dipole and the 5% partial Siberian snake were employed to correct the spin depolarization. The partial Siberian snake was a solenoid magnet and used to overcome the imperfection resonances in the AGS. This was successfully tested in the AGS in 1994 [11].

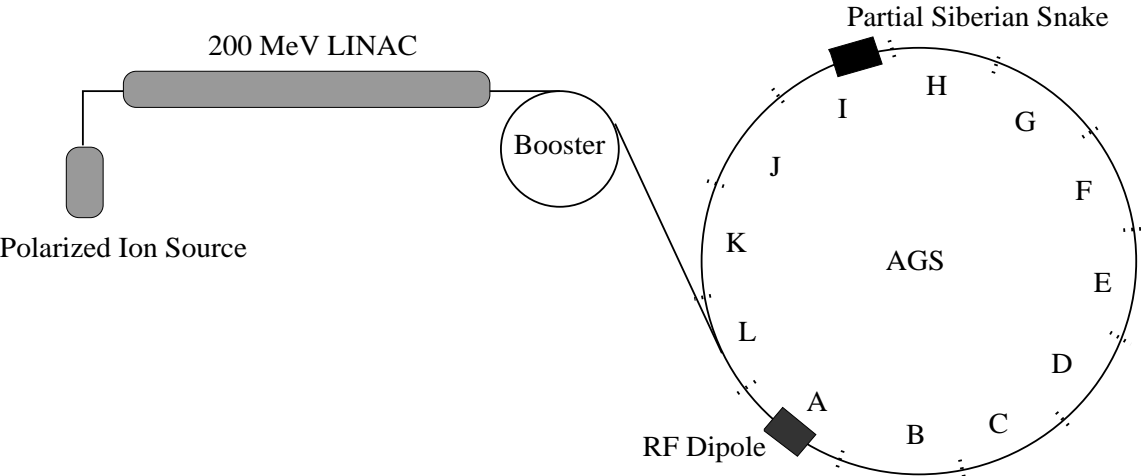


Figure 4.1: The acceleration complex of polarized proton

	AGS	Booster
circumference	807.11 m	201.78 m ($\frac{1}{4}$ of AGS)
ring	12 super-periods with 5 FODO cells/period	6 super-period with 4 FODO cells/period
bending radius	85.378 m	13.751 m
ν_x	8.85	4.8
ν_z	8.7	4.9
intensity (polarized proton)	5×10^9	8×10^9

4.1 RF Dipole Magnet

The RF dipole in the AGS was converted from a pulsed kicker magnet used for vertical betatron tune measurement during the AGS normal operation. The magnet is located in the 10th straight section of the *A* superperiod. The vertical betatron amplitude function is $\beta_z \approx 16.6$ m at this location.

The geometry of the RF dipole magnet is 81.28 cm (32") long, 30.48 cm (12") wide and 22.225 cm ($8\frac{3}{4}$ ") high with a 15.24 cm (6") wide and 6.985 cm ($2\frac{3}{4}$ ") high window. The whole magnet including the ferrite blocks was assembled inside the vacuum chamber and contains a one turn coil. A capacitor was connected with the magnet in parallel to form an LC resonant circuit. The magnet inductance was 0.825 μ henries as measured. The capacitance was chosen to match the desired frequency of the RF dipole oscillating field.

The AGS RF dipole was driven by a sinusoidal oscillating signal with modulated amplitude. The low level driving signal was generated by a WaveTek function generator (Model 296) and sent to a power amplifier. The WaveTek function generator was operated by a control program written in Labview through the GPIB interface. Fig. 4.2 is the block diagram of the RF dipole control system. The power amplifier used was an ENI 1140LA Model unit which produces 1100 Watts power from 9 to 250 kHz. Since the impedance of the magnet is lower than the power amplifier output impedance (50 Ω), a transformer with ratio of 1.67:1 was inserted for the impedance matching between the magnet and the power amplifier. At 108 kHz, the maximum achieved integrated field strength of the RF dipole was 18 Gauss-m.

During the AGS polarized proton acceleration experiment, the polarized proton beam was accelerated from the injection energy (2.3 GeV) to the desired energy about every 2.5 seconds in the AGS. Thus, the WaveTek function generator was activated by the AGS T0 signal which is synchronized with the beginning of the AGS

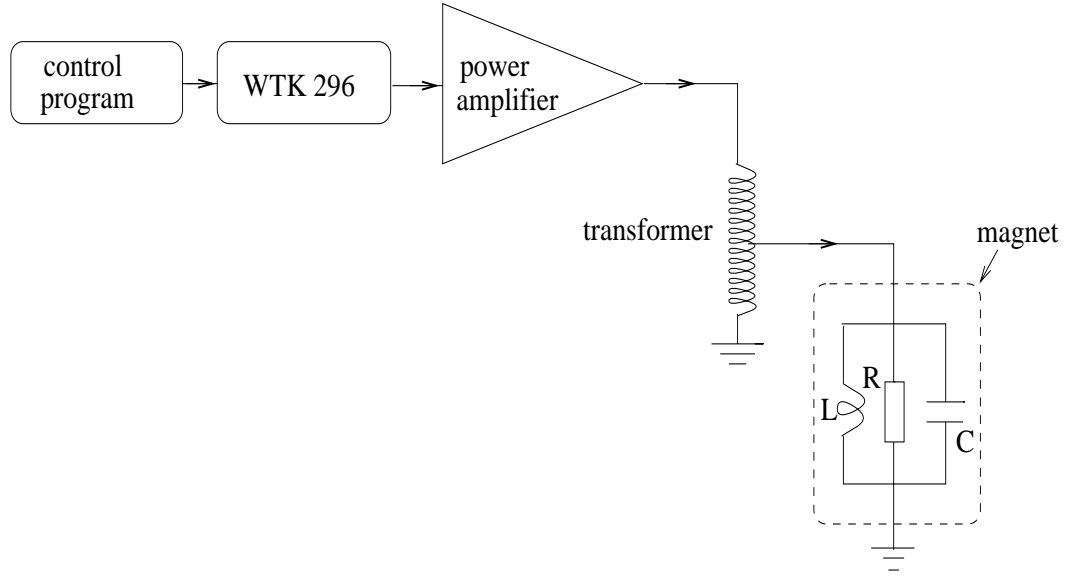


Figure 4.2: The AGS RF dipole control & driving system

acceleration cycle. Then it was triggered by the AGS Gauss Clock signal to generate the oscillating signal. The Gauss Clock signal is proportional to the beam momentum and the calibration is 19.4 counts per Gauss. Since there are four strong intrinsic spin resonances at $G\gamma = 0 + \nu_z$, $12 + \nu_z$, $36 - \nu_z$ and $36 + \nu_z$ which need to be overcome during the acceleration in the AGS up to 25 GeV/c, this external trigger signal is a chain of AGS Gauss Clock signals. The number of Gauss Clock counts is chosen to correspond to the time when each intrinsic spin resonance is encountered. The duty time of the RF dipole was about 10 ms for each spin resonance.

To accelerate the polarized proton from 2.27 GeV/c to 25 GeV/c in the AGS, the particle revolution frequency sweeps from 343.48 kHz to 371.45 kHz. Therefore, the RF dipole modulation tune, namely the ratio of the RF dipole oscillating frequency to the particle revolution frequency, would be changed if the RF dipole oscillating frequency was kept fixed. In order to maintain the separation between the RF dipole modulation tune and the natural betatron tune, the AGS RF signal was used as the external clock signal for the WaveTek function generator to generate a sinusoidal

oscillation signal with frequency locked to the AGS RF signal which is proportional to the particle's revolution frequency. In this way, the RF dipole frequency will then maintain a constant RF dipole modulation tune.

4.2 The Control Program

The RF dipole control program was a LabVIEW application. LabVIEW is a development language program developed by National Instruments. Like C and BASIC, LabVIEW is a general-purpose programming system with extensive libraries of functions and subroutines for hardware-control tasks. However, instead of being a text-based language, LabVIEW is a graphic-based language where a program is created in block diagram form. It contains application-specific libraries for data acquisition, GPIB and serial instrument control, data analysis, data presentation, and data storage. It also includes conventional program development tools like setting breakpoints.

A general LabVIEW program consists of two parts: front panel and block diagram. Front panel is the interactive user interface which simulates the panel of a physical instrument. It contains knobs, buttons, graphs and other controls and indicators. The block diagram is the source code of the application program. Fig. 4.3 shows the front panel and flow chart of the RF dipole LabVIEW application. The frequency of the output waveform is given by

$$f_m = \nu_m \frac{f_{\text{clk}}}{\text{harmonics}}, \quad (4.1)$$

where f_{clk} is the frequency of sampling clock. For this application the sampling clock is the AGS RF signal. The “end of up” in the front panel controls the number of revolutions needed to ramp the RF dipole from zero field to the desired field. The difference between the “start of dn” and “end of up” is the width of the flat-top where the RF dipole field oscillates at a constant amplitude, and the number of revolutions

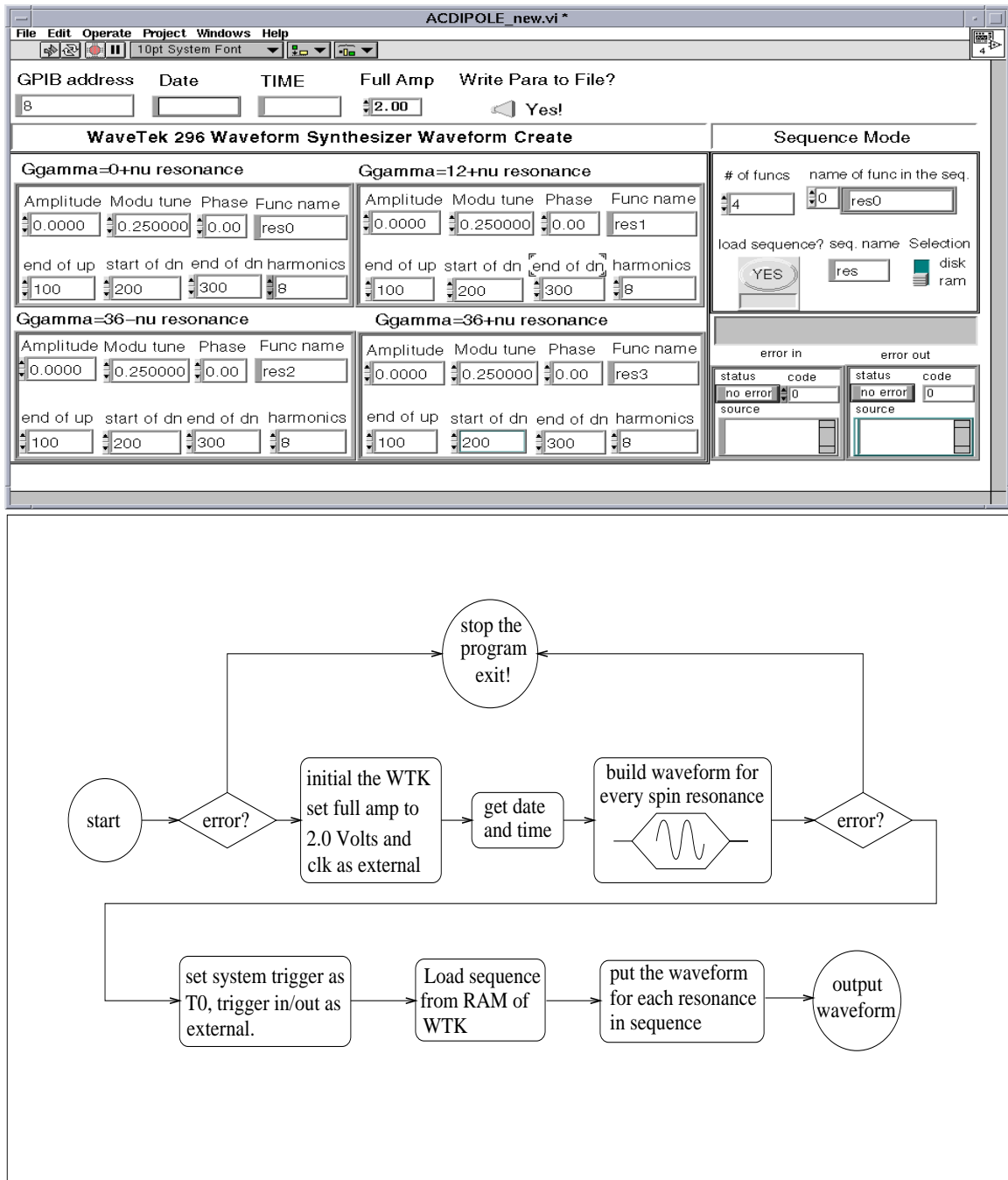


Figure 4.3: The AGS RF dipole control program. The top picture is the front panel and the bottom one is the flow diagram of the RF dipole control program.

taken to de-energize the RF dipole is given by the difference between “end of dn” and “start of dn”.

4.3 AGS Internal Polarimeter

The beam polarization in the AGS was measured by the AGS internal polarimeter installed in the 20th straight section of the C super-period. The polarimeter was designed to measure the left-right asymmetry of the $p-p$ elastic scattering in the process of proton beam scattering off a nylon fish-line ($C_6H_{11}NO$) target. The motivation is to use the well-known analyzing power of $p-p$ elastic scattering [15] to calibrate the asymmetry to the absolute beam polarization. Since only the left-right asymmetry was measured, the longitudinal and radial beam polarization components can not be determined by this polarimeter. The energy range of the internal polarimeter was designed to cover from 4 GeV/c to 25 GeV/c. Figure 4.4 is the schematic drawing of the polarimeter setup [12].

The polarimeter consists of two recoil arms, target and its mechanical system and data acquisition system. The recoil arms are identical and oriented at 77.25° away from the beam direction on the left and right side. Two scintillator counters S_1 and S_2 are placed in each arm. The hodoscope with seven 12 mm wide scintillation counters is used to determine the scattering angle. The elastic scattering is picked up by the thick scintillator counter (dE/dX counter). The thickness of the dE/dX counter was chosen to approximately stop the elastic protons in the center of the counter. Combined with the hodoscope, it also obtains the energy loss of the recoil particle as a function of its scattering angle. Since the kinetic energy of the recoil particle at different scattering angles is different, the energy loss in the dE/dX counter, or equivalently, the corresponding dE/dX pulse height is angle dependent. In order to obtain a uniform pulse height for the recoil particles with different scattering angle, a

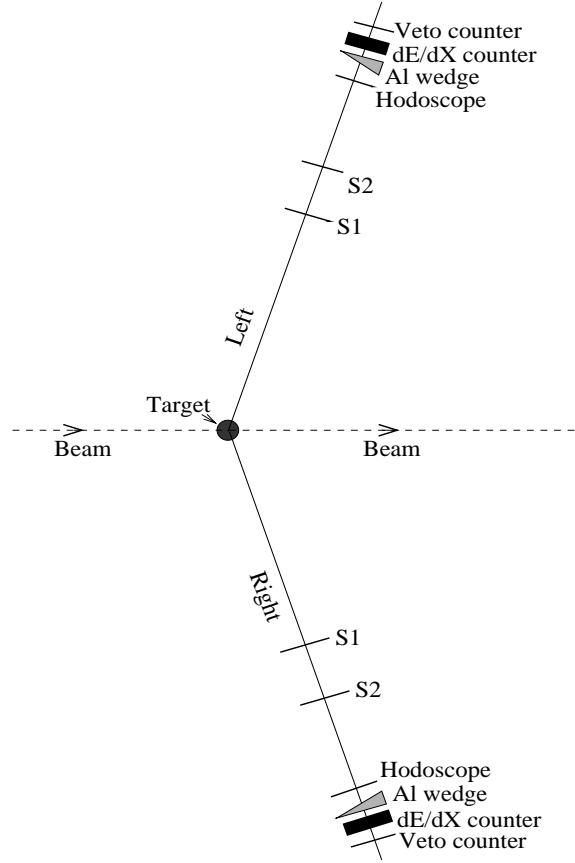


Figure 4.4: The schematic drawing of the AGS internal polarimeter setup

wedge shaped aluminum absorber was placed between the hodoscope and the dE/dX counter. The shape and thickness of the aluminum absorber were chosen so that all the recoil particles lose approximately the same amount of energy in the dE/dX counter. The wedge position should be optimized for different beam energies. The VETO counter at the end of each recoil arm is used to inhibit the inelastic scattering events in the target which produce pions. These pions possess higher energy, therefore lose less energy in the dE/dX counter, hit the VETO counter and generate a pulse.

The scattering of the proton beam off the fish-line target involves both the $p - p$ elastic scattering and p -carbon quasi-elastic scattering. The background of the p -C quasi-elastic events in the detector spectrum must be subtracted to obtain the $p - p$

elastic scattering asymmetry. The subtraction was done by measuring the left-right asymmetry with a pure carbon target. By knowing the asymmetry of the proton scattering off the fish-line target δ_f and the asymmetry of the proton scattering of the carbon target δ_c , the asymmetry of the $p - p$ elastic scattering δ_p then can be expressed as

$$\delta_p = \delta_f \frac{1 - \frac{\delta_c N_c}{\delta_f N_f}}{1 - \frac{N_c}{N_f}}, \quad (4.2)$$

where N_c and N_f are the number of events of the scattering off the carbon target and off the fish-line target, respectively.

The left-right asymmetry was calculated as

$$\delta = \frac{\sqrt{L^\uparrow R^\downarrow} - \sqrt{L^\downarrow R^\uparrow}}{\sqrt{L^\uparrow R^\downarrow} + \sqrt{L^\downarrow R^\uparrow}}, \quad (4.3)$$

where L^\uparrow and L^\downarrow are the number of events in the left arm when the beam polarization is up and down, and R^\uparrow and R^\downarrow are the corresponding events in the right arm. The beam polarization alters its direction between up and down for every AGS cycle to reduce the systematic error of the polarization measurement. The advantage of using root relations to calculate the asymmetry is that the artificial asymmetries due to unequal geometries of the two arms, the fluctuation of beam intensity from pulse to pulse and other sources are canceled out to first order.

After obtaining the left-right asymmetry, the beam polarization P can be calculated as

$$P = \frac{1}{A} \delta, \quad (4.4)$$

where A is the analyzing power and δ is the measured asymmetry. For $p - p$ elastic scattering, the analyzing power is well established [15]. An empirical formula was adopted from Ref. [15] to calculate the $p - p$ elastic scattering analyzing power for

the AGS.

$$A_p = a\sqrt{-t}(1 + bt + ct^2), \quad (4.5)$$

and

$$a = \frac{1}{p}(2.454 + 0.06081p - 0.000154p^2), \quad (4.6)$$

$$b = 1.963 - 0.3544 \log p + 0.1966(\log p)^2, \quad (4.7)$$

$$c = 0.6814 + 0.300 \log p, \quad (4.8)$$

where p is the beam momentum (GeV/c) and t is the momentum transfer given by

$$t = -4m^2 \frac{\frac{\gamma-1}{\gamma+1} \cos^2 \theta}{1 - \frac{\gamma-1}{\gamma+1} \cos^2 \theta}, \quad (4.9)$$

In Eq. (4.9), m is the proton mass, γ is the Lorentz factor and θ is the solid angle of the recoil arm. For the AGS internal polarimeter, $\theta = 77.25^\circ$. Fig. 4.5 shows the calculated analyzing power of $p-p$ elastic scattering for different beam energies.

Alternatively, the beam polarization from the measured fish-line asymmetry can also be obtained by using the effective analyzing power of fish-line in terms of the $p-p$ elastic analyzing power A_p and contribution of the p-C quasi-elastic scattering. The effective analyzing power of fish-line target A_f is given by

$$A_f = A_p \frac{1 - \frac{\delta_c}{\delta_f} \frac{N_c}{N_f}}{1 - \frac{N_c}{N_f}}. \quad (4.10)$$

4.4 AGS 5% Partial Siberian Snake

The imperfection spin resonances are corrected by a 5% partial Siberian snake [11, 12, 16] installed in the 10^{th} straight section of the I super-period. It is an 8 feet long solenoid magnet with maximum integrated strength 4.7 T-m [12].

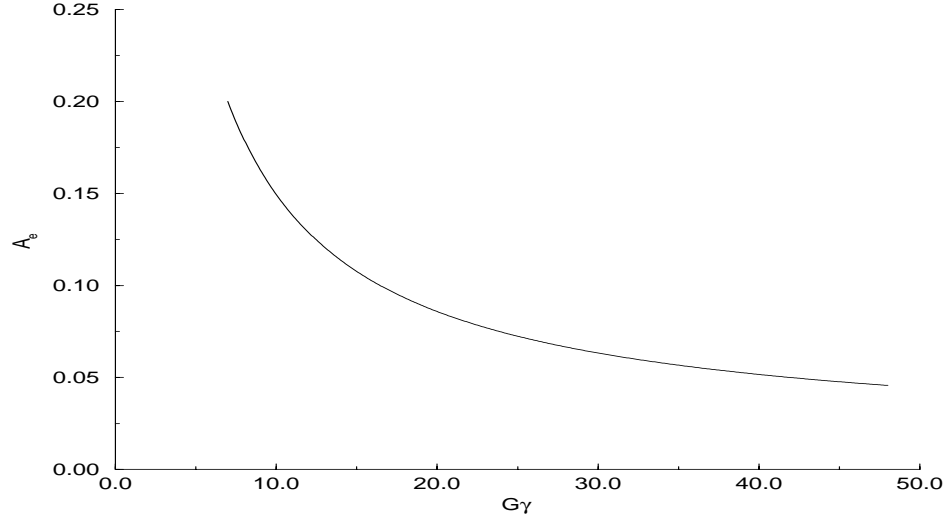


Figure 4.5: The $p-p$ elastic scattering analyzing power A_e calculated as Eq. (4.5) as a function of beam momentum

Unlike a full Siberian snake which can rotate the spin vector by 180 degrees, the 5% partial snake in the AGS only rotates the spin vector by 9 degrees. Generally, in the presence of a single snake with longitudinal magnetic field, the spin precession tune ν_s becomes

$$\cos \pi \nu_s = \cos \pi G\gamma \cos \frac{\phi}{2}, \quad (4.11)$$

and the spin closed orbit $\hat{n}_{co} = n_1 \hat{x} + n_2 \hat{s} + n_3 \hat{z}$ is given by

$$n_3 = \frac{1}{\sin \pi \nu_s} \sin(\pi G\gamma) \cos \frac{\phi}{2}, \quad (4.12)$$

$$n_1 = \frac{-1}{\sin \pi \nu_s} \sin(G\gamma(\pi - \theta)) \sin \frac{\phi}{2}, \quad (4.13)$$

$$n_2 = \frac{1}{\sin \pi \nu_s} \cos(G\gamma(\pi - \theta)) \sin \frac{\phi}{2}. \quad (4.14)$$

where ϕ is the angle the spin vector is rotated in the snake, for AGS, $\phi = 9^\circ$. Since the spin precession tune can never be an integer if ϕ is non-zero as shown in Fig. 4.6,

no depolarization will happen and the vertical component of the spin will change sign at every $G\gamma = \text{integer}$. The bottom part of Fig. 4.6 is the calculated spin closed orbit for a 5% partial snake. It shows that the beam polarization flips sign when it passes through the integer $G\gamma$ s.

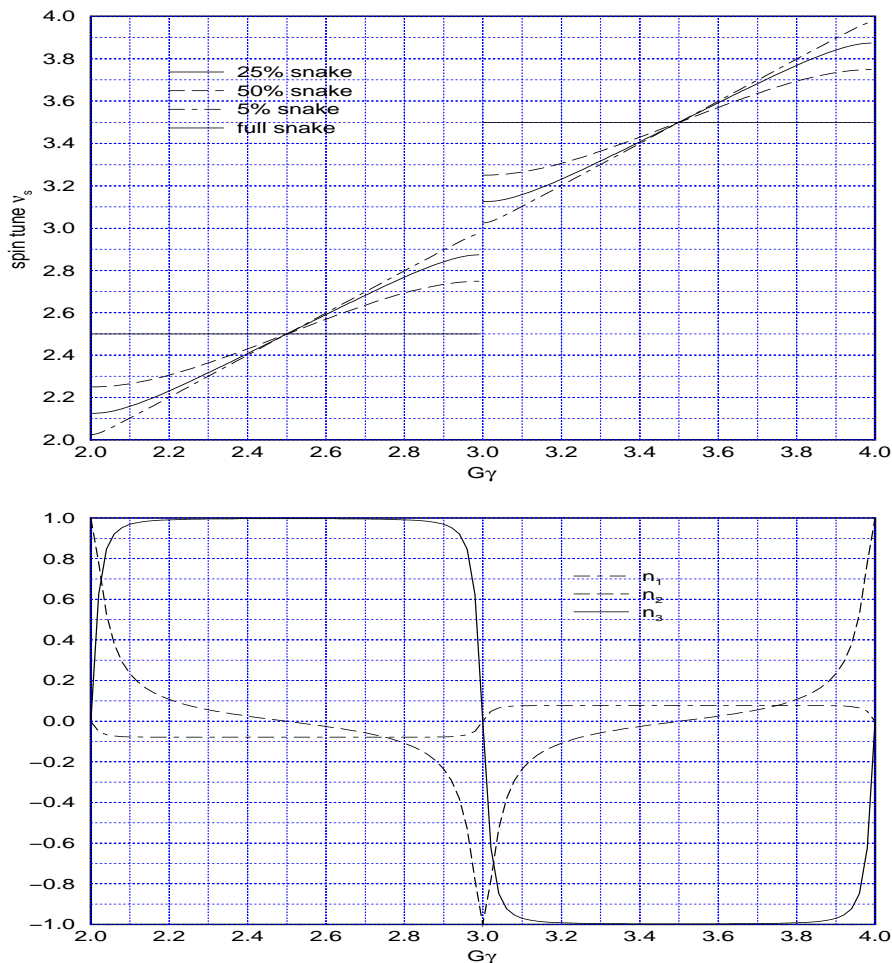


Figure 4.6: Top part: spin tune in the presence of different snake strength. Bottom part: spin closed orbit for a 5% partial snake. It shows that the beam polarization flips sign when it passes through the integer $G\gamma$ s.

The spin rotation angle ϕ is inversely proportional to the momentum rigidity $B\rho$,

i.e.

$$\phi = \frac{1+G}{B\rho} \int B_{//} dl. \quad (4.15)$$

Therefore, in order to keep the partial snake to be able to rotate the spin vector by 9 degrees during the acceleration, the partial snake has to be ramped along with the acceleration.

Chapter 5

Experimental Results

The method of using an RF dipole to force all particles in a beam to coherently oscillate at a large amplitude and induce full spin flip was successfully tested in the recent polarized proton runs. The experimental results are presented in this chapter along with the discussion of a new type of second order spin depolarization resonance observed in the experiment. The results of adiabatic excitation with the AGS Au⁺⁷⁷ beam and the AGS chromaticity studies are also included.

5.1 Results Of Experiments With The AGS Au⁺⁷⁷ Beam

To demonstrate the feasibility of adiabatically exciting a coherent betatron oscillation with an RF dipole, experiments were performed parasitically in the AGS with unpolarized Au⁺⁷⁷ beam during the Heavy Ion Physics run in 1996.

In the experiment, the RF dipole resonant frequency was tuned at 70 kHz, and the RF dipole magnetic field was linearly ramped up in about 3 ms and kept at full amplitude for about 4 ms then ramped back to zero in another 3 ms. Since the RF

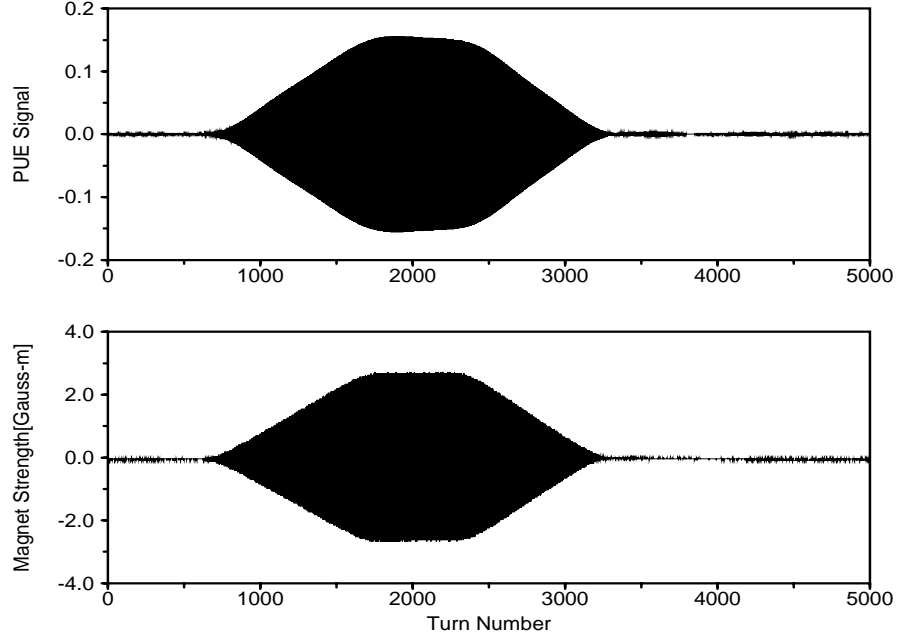


Figure 5.1: Transverse displacement (top) and RF dipole magnet field amplitude (bottom) as a function of revolutions about the AGS. The raw PUE data was filtered to suppress the noise background.

dipole modulation tune would change about 0.01 during the normal acceleration of the Au^{+77} beam, the amplitude modulated sinusoidal oscillating signal of the RF dipole was locked with the AGS RF signal to keep a constant modulation tune. The normalized vertical emittance (95%) of the beam was about 5π mm-mrad and the rms beam size at the working energy (1.1 GeV/c per nucleon) was about 3.9 mm at a maximum amplitude function location in the vertical plane.

The measured turn-by-turn beam vertical betatron oscillation shows that a coherent oscillation was adiabatically excited by operating an RF dipole close to one of the betatron sidebands. Figure. 5.1 shows a typical example where the coherent betatron motion follows the RF dipole field amplitude. The top part of the figure is the turn by turn data of beam vertical displacement measured by a pick-up electrode (PUE).

The PUE is located 4.5 betatron oscillations downstream of the RF dipole, where the vertical amplitude function is 15.4 m. The bottom part of Fig. 5.1 is the readback from the RF dipole current transformer as a function of revolution number. Here, the full dipole strength is 2.82 G-m and its modulation tune is 0.75. The intrinsic vertical betatron tune was measured as 8.745.

In this particular measurement, the beam was accelerated during the excitation. Since the RF dipole becomes less effective on the beam motion as the beam energy is increased (See Eq. (3.15)), the coherent oscillation amplitude slightly decreased while the RF dipole magnetic field oscillating amplitude remained fixed as shown in Fig. 5.1.

The transverse displacement data displayed in Fig. 5.1 was obtained by filtering the raw PUE data through a digital bandpass filter (Equi-Ripple Bandpass) using the Park-McClellan algorithm[13]. Four parameters are needed to determine the stop and pass region of the filter, i.e. higher and lower stop frequencies, higher and lower pass frequencies. The first stopband of the filter goes from zero (DC) to the lower stop frequency. The passband region is between the lower and higher pass frequencies, and the second stopband of the filter goes from the higher stop frequency to the Nyquist frequency. By carefully choosing these four parameters, the noise on the excited coherent oscillation signal, whose frequency is significantly differed from the driving frequency and the intrinsic betatron frequency, can be eliminated.

The evolution of the beam vertical profile was also monitored during the excitation. It was measured by using the existing AGS IPM (Ionization Profile Monitor) system [17]. Results from a typical emittance scan are shown in Fig. 5.2. The top portion of the figure shows the rms beam size (in mm) versus time, with measurements taken in 1 ms intervals. The bottom part of the figure shows a mountain range plot of the corresponding vertical beam profiles. The broadening of the distribution and narrowing as the RF dipole magnet turns off is evident. Because of the long

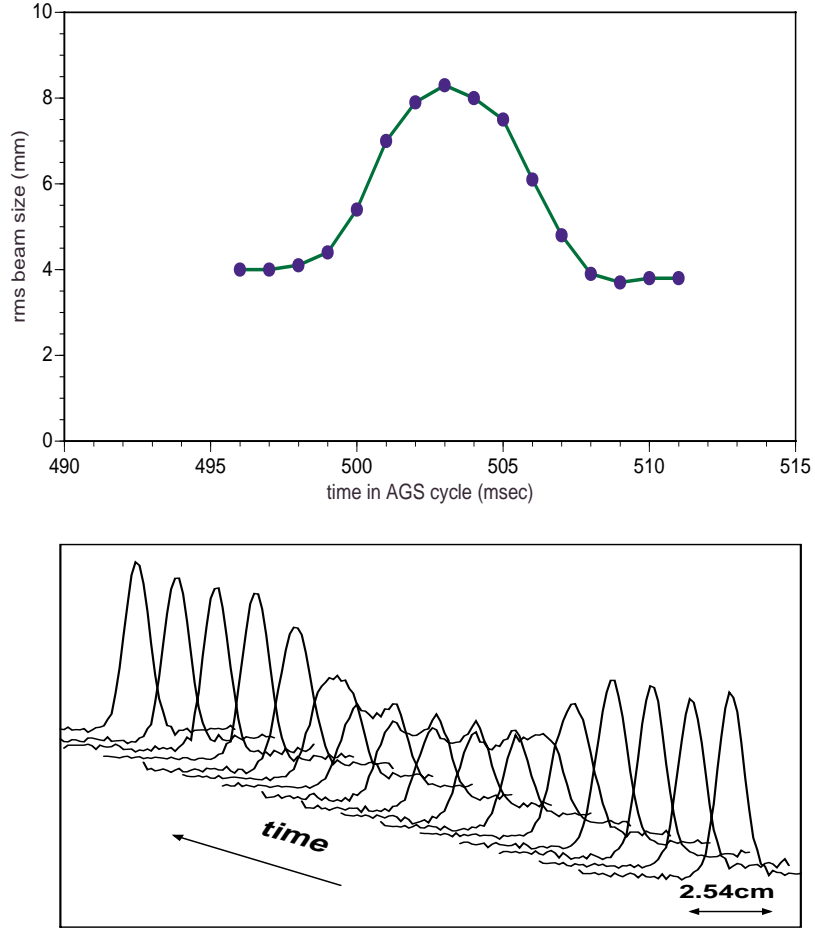


Figure 5.2: Measured transverse rms beam size versus time in AGS cycle (top). Corresponding beam profiles versus time in AGS cycle (bottom).

IPM system measurement time (about 3 ms) in which is beam circulates the AGS roughly 900 times, the measured beam profile is the combined effect of the actual beam size and the coherent betatron oscillation. The rms beam size shown in the plot is the time averaged value. The maximum “measured” rms beam size is related to the actual rms beam size, σ , and the oscillation amplitude Z_{coh} generated by the

RF dipole by

$$\sigma_{meas} = \sigma \sqrt{1 + \frac{1}{2} \left(\frac{Z_{coh}}{\sigma} \right)^2}. \quad (5.1)$$

The fact that the measured rms beam size returns to its previous value indicates that the excitation was indeed adiabatic and that the beam emittance was preserved.

The coherence amplitude as a function of the resonance proximity parameter δ was measured for both acceleration case and fixed energy case in the AGS. The RF dipole modulation tune was held fixed and the betatron tune was changed to produce different separations between the RF dipole modulation tune and the vertical intrinsic betatron tune.

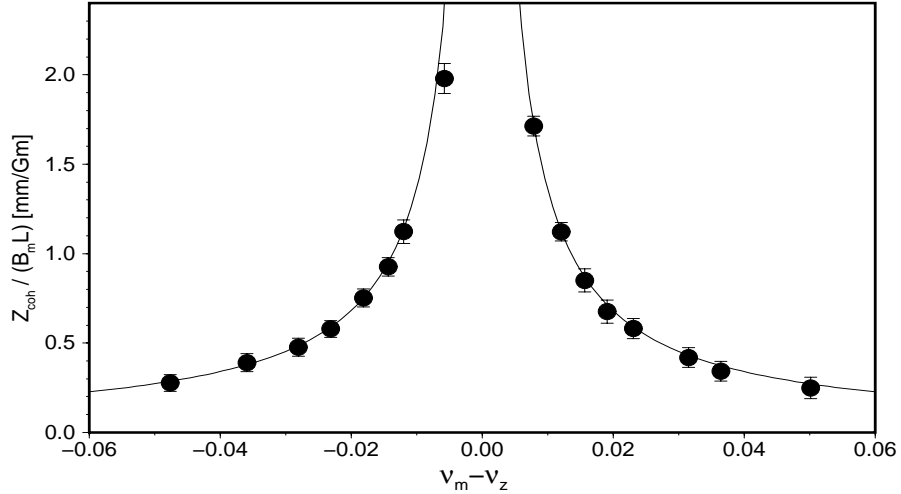


Figure 5.3: Normalized betatron oscillation amplitude versus δ . The solid line is the predicted curve using Eq. (3.18). The acceleration rate is zero for these measurements.

The ratio of the measured coherent amplitude to dipole field amplitude is shown in Fig. 5.3 as a function of different tune separations between the modulation tune and the betatron tune. During this set of measurements, the momentum was held fixed at 1.1 GeV/c per nucleon. This particular ratio is shown because when the tunes were placed near resonance without reducing the dipole field amplitude, the

oscillation amplitude would become large enough to induce beam loss. Thus, only smaller amplitude oscillations provided meaningful measurements at these tune separations. For a tune separation of 0.01, the largest amplitude oscillation which could be maintained without significant beam loss was 2.6 times the rms beam size.

A similar set of measurements is depicted in Fig. 5.4, where in this case the beam is being accelerated at a rate of $\dot{\gamma} \equiv \frac{d\gamma}{dt} = 2.44 \text{ sec}^{-1}$, where γ is the Lorentz factor. By comparing the experimental results from the beam acceleration mode and the results from the beam storage mode, one can conclude that the coherent betatron oscillations are independent of the beam acceleration mode or beam storage mode provided that the time separation between the modulation tune and the intrinsic betatron tune is kept constant.

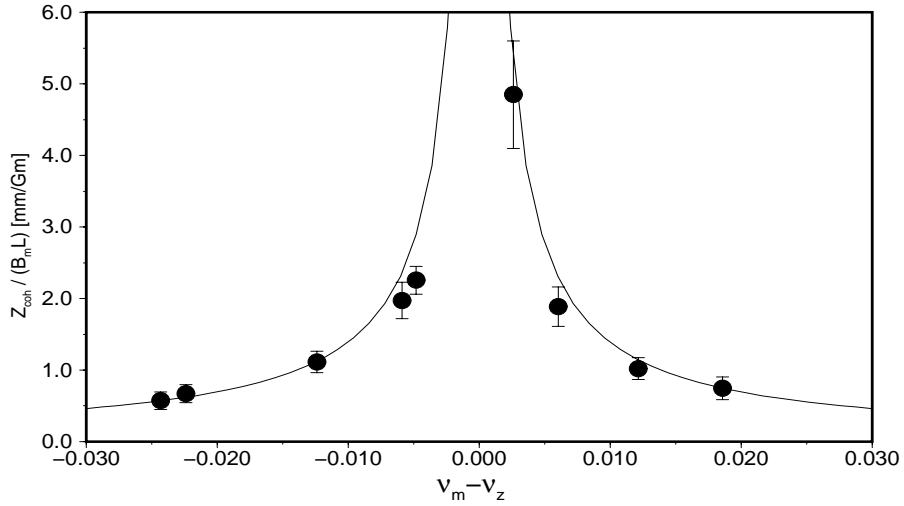


Figure 5.4: Normalized betatron oscillation amplitude versus δ . The solid line is the predicted curve using Eq. (3.18). The corresponding acceleration rate is $\dot{\gamma} = 2.44 \text{ sec}^{-1}$.

Effects of power line ripple

During the experiment, problems with power line ripple were also encountered. In the AGS, an acceleration rate higher than $\dot{\gamma} = 2.44s^{-1}$ requires switching between two different bending magnet power supplies to achieve the necessary voltage in the magnet circuit. The more powerful supply introduces 720 Hz power line ripple to the combined function magnets. Thus, the rate of change of energy, the betatron tunes, and, to the extent that the RF radial loop can follow, the beam orbit are modulated. The net effect is a modulation of the tune separation δ . Figure 5.5 shows an example of this ripple effect.

The beam coherence signal measured from the PUE is shown in the bottom part of Fig. 5.5; a beating structure is evident. The top part in the same figure is the FFT of the data, in which ripple sidebands are apparent.

This power supply ripple can be modeled as a betatron tune modulation on the betatron motion. Using the smooth approximation, the equation of motion is given by

$$\ddot{z} + [\nu_0(1 + \epsilon \cos \nu_r \theta)]^2 z = a \cos(\nu_m \theta + \chi), \quad (5.2)$$

where the overdot is the derivative with respect to the orbital angle θ , z is the betatron displacement as a function of θ , ν_0 is the betatron tune, ν_r is the ripple tune, ϵ is the ripple amplitude, ν_m is the modulation tune, χ is an arbitrary phase angle, and a is the modulation amplitude.

To simplify our discussion without loss of generality, we assume $\chi = 0$. The forced oscillator equation can be solved by the ansatz

$$z = A \cos \nu_m \theta + \sum_{n=1}^{\infty} B_{n\pm} \cos(\nu_m \pm n\nu_r)\theta. \quad (5.3)$$

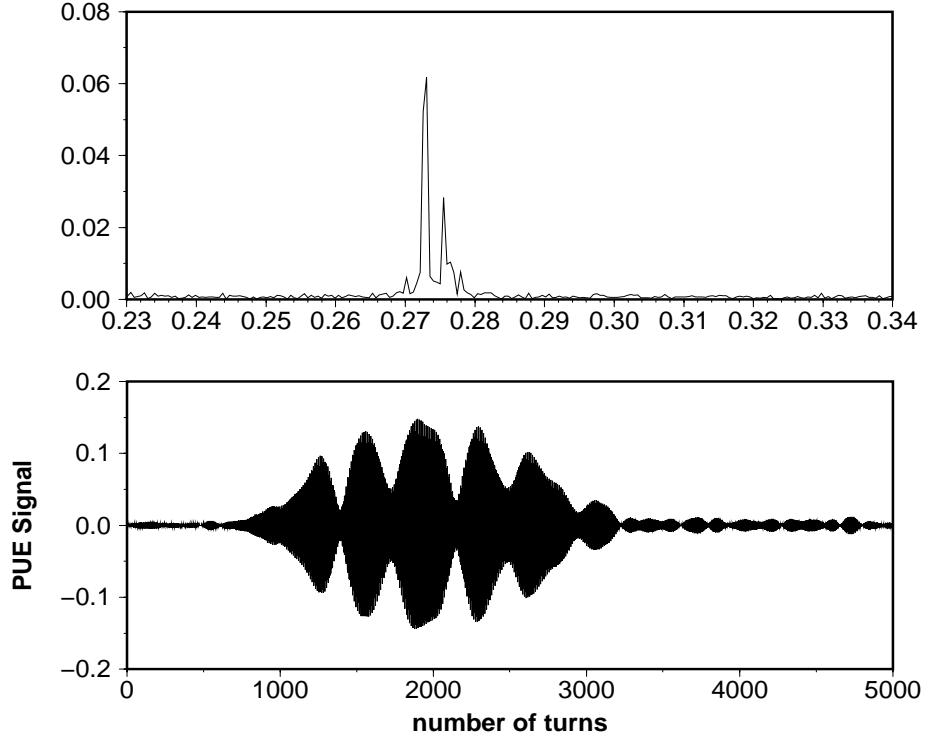


Figure 5.5: The lower part is raw data of transverse oscillations in the presence of power line ripple. The top trace is the FFT of the data, showing the ripple sideband. For this trace, the horizontal axis is the fractional tune. The modulation tune, the large peak, is 0.273.

Since ϵ is a small number, we obtain

$$A = \frac{a}{\nu_0^2 - \nu_m^2 + \frac{\nu_0^4 \epsilon^2}{(\nu_m - \nu_r)^2 - \nu_0^2} + \frac{\nu_0^4 \epsilon^2}{(\nu_m + \nu_r)^2 - \nu_0^2}}, \quad (5.4)$$

and

$$B_{1\pm} = \frac{A\nu_0^2 \epsilon}{(\nu_m \pm \nu_r)^2 - \nu_0^2}. \quad (5.5)$$

Similarly, higher order sidebands can be obtained. Thus, the power supply ripple produces modulated betatron motion with sidebands around the modulation harmonic.

It is worth noting that the sideband amplitudes $B_{n\pm}$ are finite even for $\nu_m = \nu_0 \pm n\nu_r$. There exists only one dipole mode singularity at $\nu_m \approx \nu_0$.

The initial coherent betatron oscillation in the presence of power supply ripple can decohere to induce emittance growth. Careful control of power supply ripple is important to minimize the emittance growth.

5.2 The AGS Chromaticity Setting

As the amplitude of the excited coherent oscillation is inversely proportional to the distance between the intrinsic betatron oscillation tune and the RF dipole oscillation tune shown in Eq. (3.15). A significant tune spread within the particle beam will generate a range of amplitudes. The beam will then occupy more of the aperture, which in turn could lead to beam loss. For instance, assume the tune spread of the beam is 0.003 and the driving tune is 0.005 away from the resonance. In order to keep the outer edge of the beam still within the beam pipe, the central coherent oscillation amplitude can only be 40% of what it would be for zero tune spread. So, to relax the requirement on the available aperture when the RF dipole tune is needed to be closer to the resonance, a very small tune spread is desirable.

One of the major sources of betatron tune spread in the AGS is the chromaticity, namely, the dependence of the betatron tune with the momentum. The corresponding betatron tune spread is given by

$$\Delta\nu = \xi \frac{\Delta p}{p} \quad (5.6)$$

where ξ is the chromaticity and $\frac{\Delta p}{p}$ is the relative momentum spread of the beam.

As an example, if the relative momentum spread $\frac{\Delta p}{p}$ is on the order of 0.001, to make the tune spread of the same order, the chromaticity ξ needs to be controlled to the level of one unit. To achieve this goal, a good model of the sextupole components

in the AGS bending magnets would be very helpful for a better understanding and controlling of the AGS chromaticity properties of the machine.

For a simple lattice composed of N FODO cells, the chromaticity ξ is about equal in magnitude and opposite in sign to the betatron tune [25], i.e.

$$\xi = -\frac{\tan \phi}{\phi} \approx -\nu. \quad (5.7)$$

This is because

$$\xi \approx -\frac{1}{4\pi} \oint \beta K ds \approx -\frac{N}{4\pi} \left(\frac{\beta_F}{f} - \frac{\beta_D}{f} \right), \quad (5.8)$$

where

$$\beta_F = \frac{2L(1 + \sin \frac{1}{2}\phi)}{\sin \phi}, \quad (5.9)$$

$$\beta_D = \frac{2L(1 - \sin \frac{1}{2}\phi)}{\sin \phi}, \quad (5.10)$$

in the thin lens approximation. In the two equations of β_F and β_D , L is the length of the drift space between two quadrupoles, and ϕ is the phase advance of one FODO cell.

The sextupole magnetic field also gives a major contribution to the chromaticity. In thin lens approximations, the contribution of sextupole field to the chromaticity is given by

$$\xi_{x,sextupole} = \frac{1}{4\pi} \int \beta_x D \frac{B''}{B\rho} ds, \quad (5.11)$$

$$\xi_{z,sextupole} = -\frac{1}{4\pi} \int \beta_z D \frac{B''}{B\rho} ds, \quad (5.12)$$

where D is the dispersion function at the place of the sextupole, β_x and β_z are the betatron amplitude functions in the horizontal and vertical planes. Thus, the chromaticity of the machine can be adjusted by using sextupoles at non-zero dispersion locations. In the AGS, the chromaticity can be corrected by two families of high field

sextupoles with two sextupole magnets from each family located in every super-period at horizontal β_{xmax} and vertical β_{ymax} , respectively.

The AGS lattice is composed of combined function magnets which provide both dipole and quadrupole magnetic fields. Since the sextupole field is a systematic error in the dipole magnets, the chromaticity change due to the sextupole component of the AGS bending magnet is sizable and has to be included in the chromaticity calculations.

E. Blesser, E. Auerbach and R. Thern analyzed the measured point-to-point field maps for the AGS bending magnets over a number of different current settings and obtained an empirical parameterized formula for quadrupole and sextupole fields [19].

$$K_1 = \frac{1}{B\rho} \frac{dB}{dx} \quad (5.13)$$

$$= a_{-2} \frac{1}{p^2} + a_{-1} \frac{1}{p} + a_0 + a_1 p + a_2 p^2 \\ + a_3 p^3 + a_4 p^4 + a_5 p^5 + a_6 p^6;$$

$$K_2 = \frac{1}{B\rho} \frac{d^2 B}{dx^2} \quad (5.14)$$

$$= b_{-3} \frac{1}{p^3} + b_{-2} \frac{1}{p^2} + b_{-1} \frac{1}{p} + b_0 + b_1 p + b_2 p^2 \\ + b_3 p^3 + b_4 p^4 + b_5 p^5 + b_6 p^6.$$

where the coefficients a_i and b_i with i as index are listed in Table 5.1. This table provides a model of the AGS chromaticity with the quadrupole and sextupole components smoothly distributed in the bending magnet.

On the other hand, sextupole fields in the AGS bending magnets are divided into several components. At intermediate fields, sextupole field is mainly from the ends of the dipole magnets. At high fields, the sextupole field arises mainly from the magnet saturation.

We assume that the strengths of the sextupole fields from the body of the magnets

Table 5.1: The coefficients of the empirical parameterized formula.

	AF	AD	BF	BD	CF	CD
a_{-2}	-9.963E-6	1.049E-5	-1.037E-5	1.086E-5	1.939E-5	-1.816E-5
a_{-1}	-2.712E-4	2.776E-4	-2.791E-4	2.839E-4	3.726E-4	-3.682E-4
a_0	4.877E-2	4.872E-2	4.858E-2	4.853E-2	4.854E-2	4.847E-2
a_1	4.252E-5	-4.422E-5	4.181E-5	-4.329E-5	1.565E-5	-1.480E-5
a_2	-1.503E-5	1.543E-5	-1.455E-5	1.490E-5	-7.013E-6	6.803E-6
a_3	1.990E-6	-2.024E-6	1.905E-6	-1.935E-6	1.128E-6	-1.102E-6
a_4	-1.247E-7	1.258E-7	-1.185E-7	1.195E-7	-8.217E-8	8.025E-8
a_5	3.724E-9	-3.727E-9	3.516E-9	-3.524E-9	2.771E-9	-2.696E-9
a_6	-4.330E-11	4.305E-11	-4.085E-11	4.071E-11	-3.563E-11	3.457E-11
b_{-3}	-2.112E-5	-4.541E-5	-3.360E-5	-5.333E-5	3.241E-5	5.462E-5
b_{-2}	2.313E-4	3.866E-4	3.420E-4	4.614E-4	1.491E-4	-3.118E-4
b_{-1}	-4.989E-3	-5.152E-3	-5.262E-3	-5.368E-3	4.230E-3	4.530E-3
b_0	-6.356E-3	-6.237E-3	-7.659E-3	-7.548E-3	-1.036E-2	-1.033E-2
b_1	-1.355E-4	-8.211E-5	-1.202E-4	-8.463E-5	-4.559E-4	-5.104E-4
b_2	5.202E-5	2.948E-5	4.837E-5	3.258E-5	1.559E-4	1.748E-4
b_3	-5.935E-6	-2.636E-6	-5.852E-6	-3.462E-6	-1.702E-5	-1.907E-5
b_4	2.124E-7	2.178E-9	2.318E-7	7.609E-8	7.902E-7	9.025E-7
b_5	6.365E-11	6.024E-9	-1.237E-9	3.240E-9	-1.445E-8	-1.751E-8
b_6	-9.882E-11	-1.607E-10	-7.770E-11	-1.247E-10	3.833E-11	7.240E-11

are

$$K_{2S}L_S = c_{-1}\frac{1}{p} + c_0 + c_1p + c_2p^2 + c_3p^3, \quad (5.15)$$

$$K_{2L}L_L = K_{2S}\frac{90}{75}. \quad (5.16)$$

where $K_{2S}L_S$ and $K_{2L}L_L$ are the integrated strengths of the body sextupole fields of the long (228.6 cm, or 90 inches) and short (90.5 cm, or 75 inches) bending magnets, respectively. Here, we assume that the body sextupole integrated strength of the bending magnet is proportional to the length of the magnet. The strengths of the sextupole fields coming from the two ends of the bending magnet, it is assumed to be independent of the beam energy, i.e.

$$K_{2E}L_E = \text{constant} = d. \quad (5.17)$$

The coefficients c_i ($i = -1, 0, 1, 2, 3$) and d with i as the index were used to fit the measured chromaticities [18, 19] for different momenta, The results are

$$K_{2S}L_S = 0.058\frac{1}{p} - 5.2 \times 10^{-4} - 3.6 \times 10^{-4}p - 7.0 \times 10^{-5}p^2 + 2.8 \times 10^{-6}p^3, \quad (5.18)$$

$$K_{2E}L_E = -0.017. \quad (5.19)$$

The second term in $K_{2S}L_S$ is from the eddy current on the vacuum chamber and is proportional to the magnetic field ramping rate \dot{B} . In these chromaticity measurements, $\dot{B} = 2$ T/s.

Comparison of the experimental data with the MAD results of different models

Figure 5.6 shows the comparisons of the MAD calculations of using different models with the measured chromaticities obtained in the first test using the RF dipole to excite a vertical coherent oscillation with the AGS Au^{+77} beam. The chromaticity was measured at momentum $p \approx 1.1$ GeV/c per nucleon with zero acceleration rate.

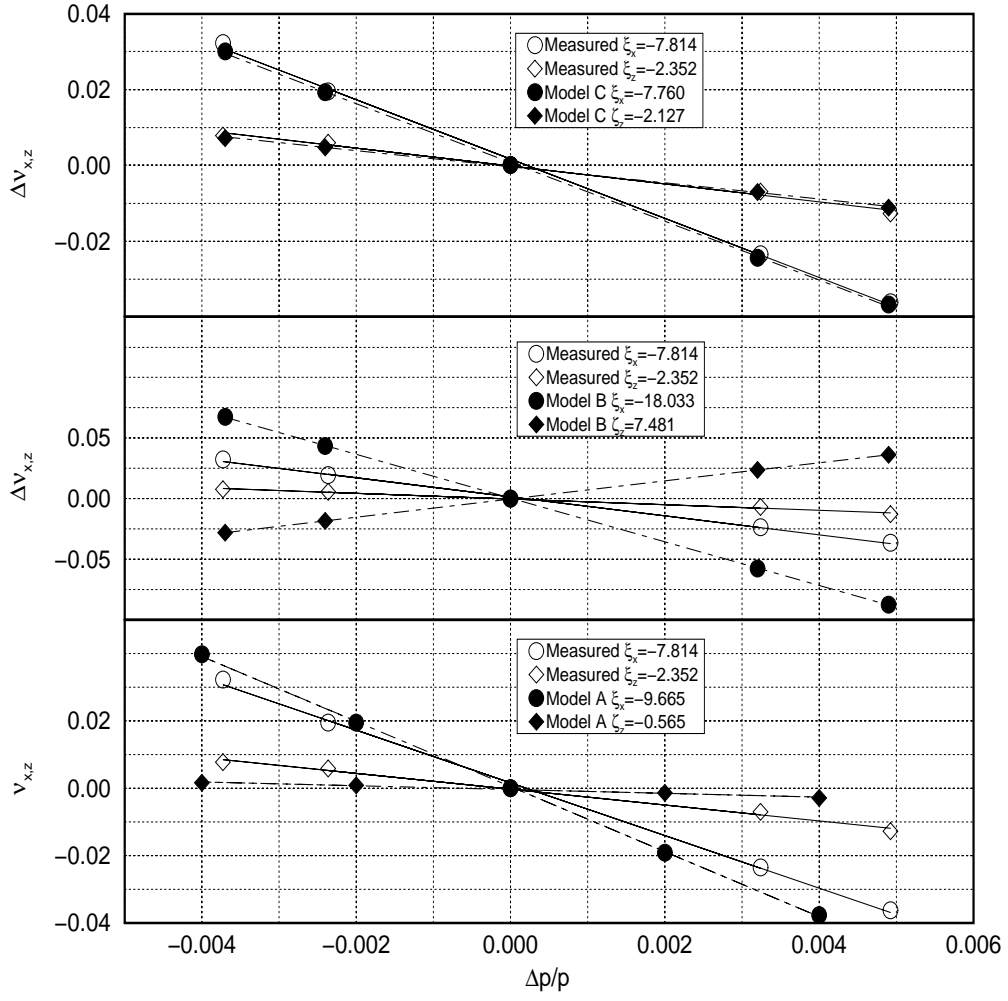


Figure 5.6: The comparisons of the MAD calculations of different models with the measured chromaticities. Model C is the same as Model B except the sextupole strength from the end of the AGS bending magnet is -0.0078 instead of -0.017. Since in the experiment, the measurement was taken at fixed energy, the second term in $K_{2S}L_S$ which reflects the eddy current effect was set to zero in the Model B and C calculations.

Meanwhile, since the bending magnetic field was ramped during the acceleration, an eddy current was induced on the vacuum chamber [20]. The induced eddy current, in turn, produces an additional sextupole field which will then act on the beam and change the chromaticity. For a nearly rectangular shaped vacuum chamber, the sextupole field due to the eddy current effect can be written as

$$K_2 \approx 2\mu_0\sigma \frac{h}{g} \frac{\dot{B}}{B\rho}, \quad (5.20)$$

where $\dot{B} = \frac{dB}{dt}$ is the ramping rate of the bending magnetic field, h is the thickness of the vacuum chamber, g is the gap height and σ is the conductivity of the chamber material. For stainless steel $\mu_0\sigma \approx 2 \text{ sec}/m^2$. For the AGS, the vacuum chamber was made of stainless steel and $h/g \approx 0.078/3$, thus the sextupole field due to the eddy current is about

$$K_2 = 0.104 \frac{\dot{B}}{B\rho} \quad [m^{-3}]. \quad (5.21)$$

5.3 Spin Experimental Results

To accelerate polarized protons to 25 GeV in the AGS, numerous spin depolarization resonances will be encountered including forty-three imperfection resonances at every integer $G\gamma$ and seven intrinsic resonances at $0 + \nu_z$, $12 + \nu_z$, $24 \pm \nu_z$, $36 \pm \nu_z$ and $48 - \nu_z$. Their strengths are related with the vertical closed orbit distortions for the imperfection resonances and the vertical betatron oscillation amplitude for intrinsic resonances. Since the AGS has 12 superperiods with five FODO cells in every period, 12 and its integer multiples are dominant harmonics and harmonic 60 is the most important one. Among the seven intrinsic spin resonances, four of them are strong ones, i.e. $0 + \nu_z$, $12 + \nu_z$, $36 \pm \nu_z$. The other three resonances are relatively weak and will not cause significant polarization loss. Table 5.2 lists the ratio of the polarization after crossing each of those spin resonances to the initial polarization for a beam with

Table 5.2: AGS intrinsic spin resonances in the acceleration from 2.27 GeV/c to 25 GeV/c

P[GeV/c]	$G\gamma$	ϵ_k	$\frac{P_f}{P_i}$
4.45	$0 + \nu_z = 8.7$	0.0061	-0.418
7.95	$24 - \nu_z = 15.3$	0.0002	0.995
10.79	$12 + \nu_z = 20.7$	0.0024	0.452
14.25	$36 - \nu_z = 27.3$	0.0051	-0.260
17.08	$24 + \nu_z = 32.7$	0.0004	0.979
20.54	$48 - \nu_z = 39.3$	0.0006	0.953
23.37	$36 + \nu_z = 44.7$	0.011	-0.772

10π mm-mrad normalized 95% vertical emittance. The third column is the strength of each spin resonance assuming a single particle at normalized rms $\frac{10}{6}\pi$ mm-mrad ellipse. Fig. 5.7 shows the final polarization of the polarized proton beam after crossing all the seven intrinsic resonances without any corrections as a function of vertical beam emittance. One can see that for a beam with about 10π mm-mrad emittance, the survived polarization is less than 10% after passage through all the seven intrinsic spin resonances under the normal AGS acceleration rate.

In the AGS Booster, polarized protons were injected at $G\gamma = 2.18$ and extracted at $G\gamma = 4.7$. The imperfection resonance at $G\gamma = 4$ was corrected by the vertical harmonic correctors with magnetic fields

$$B = a_k \cos k\theta + b_k \sin k\theta \quad (5.22)$$

where k is the harmonic number and a_k and b_k are the field amplitudes. The imperfection resonance at $G\gamma = 3$ is much weaker and the depolarization is negligible. Since the Booster vertical betatron tune was set as $\nu_z = 4.9$, there is no strong intrinsic resonance during the acceleration cycle.

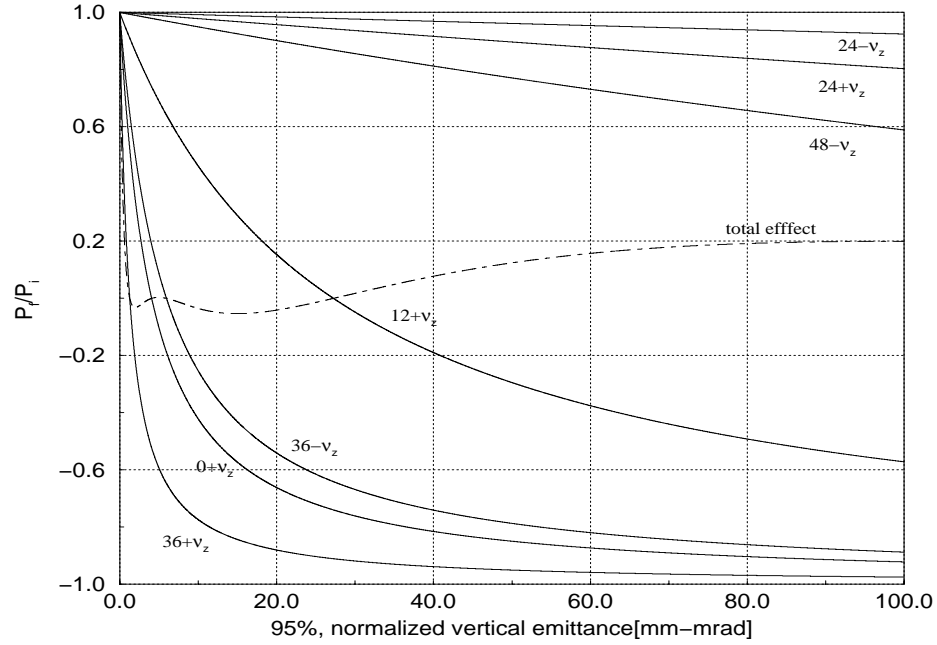


Figure 5.7: The final beam polarization as a function of the beam vertical emittance after crossing the seven intrinsic resonances without corrections. The initial polarization is 1.0 and the acceleration rate $\alpha = 4.8 \times 10^{-5} \text{ rad}^{-1}$ for this calculation.

The first experiment using the RF dipole to overcome strong intrinsic resonances was performed in the AGS Polarized Proton Acceleration Experiment in July, 1997. Table 5.3 listed schemes which were used in the experiment to overcome different types of spin depolarization resonances in the AGS

Since it is destructive for the AGS internal polarimeter to take measurements with bunched beam because of very high count rates, the beam polarizations were measured at flat-top energies when the acceleration stopped and beam was debunched. Three energy flat-tops were set up at $G\gamma = 13.5$, $G\gamma = 24.5$ and $G\gamma = 30.5$ successively to check the beam polarizations after crossing $0 + \nu_z$, $12 + \nu_z$ and $36 - \nu_z$ respectively.

Table 5.3: Schemes for spin resonance correction.

Scheme	Type of spin resonances
5% partial Siberian snake	imperfection resonances
RF dipole	strong intrinsic resonances at $0 + \nu_z$, $12 + \nu_z$ and $36 - \nu_z$
none	weak intrinsic resonances at $24 \pm \nu_z$ and $48 - \nu_z$

5.3.1 RF dipole amplitude scan at three resonances

Fig. 5.8 shows the measured polarization after crossing each of the three intrinsic resonances at $0 + \nu_z$, $12 + \nu_z$ and $36 - \nu_z$ for different amplitudes of the RF dipole field strength with the distance between the RF dipole modulation tune and the vertical intrinsic betatron tune fixed. The systematic error of the beam polarization was estimated to be 0.10, and the statistical error was about ± 0.03 .

The middle portion of Fig. 5.8 shows the beam polarization after crossing intrinsic resonance $G\gamma = 12 + \nu_z$ for different RF dipole field strength amplitudes. The RF dipole modulation tune was set at 0.004 away from the vertical betatron tune. When the RF dipole was turned off, the beam was fully depolarized. When the amplitude of the excited coherent oscillation was increased, the amount of spin flip was increased until a full spin flip plateau was reached for $Z_{\text{coh}} \leq 15$ mm as shown in Fig. 5.8. The fact that the beam polarization saturated at large amplitudes of the excited coherent oscillation indicates a full spin flip was achieved.

The solid curves shown in Fig. 5.8 correspond to result obtained in numerical spin simulations which calculate the beam polarization after crossing two spin resonances separated by a tune difference distance δ . The beam polarization was obtained from

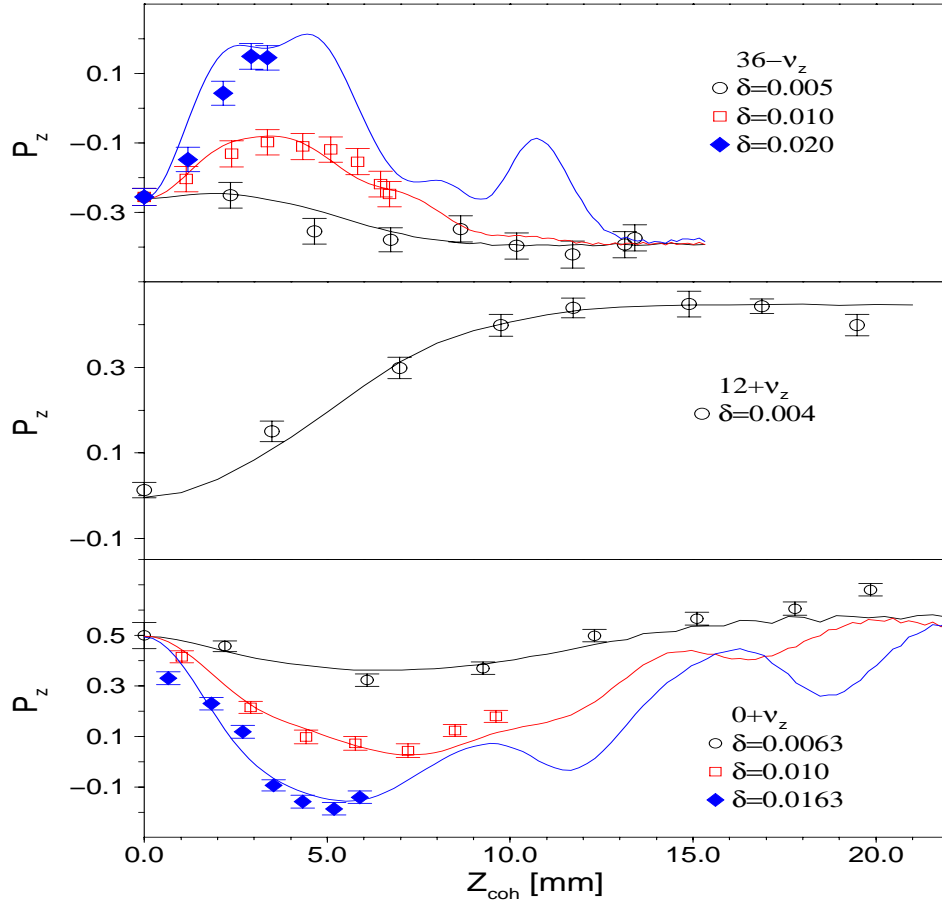


Figure 5.8: The measured proton polarization vs. the coherent betatron oscillation amplitude (in mm) for different tune separations at spin depolarizing resonances $0 + \nu_z$ (bottom plot), $12 + \nu_z$ (middle plot), and $36 - \nu_z$ (upper plot). P_z stands for the vertical polarization, while Z_{coh} stands for the vertical coherent oscillation amplitude. The error bars show only the statistical errors. The resonance strength of the coherent spin resonance due to the RF dipole is proportional to the coherent betatron amplitude. The curves are the results of multi-particle spin simulations based on a model with two overlapping spin resonances.

the ensemble average of a collection of thirty-two particles which were arranged to simulate a Gaussian distribution [See Appendix A]. The spin vector of each particle was tracked by multiplying its turn by turn transform matrix. A scaling factor was introduced to normalize the simulation results to the corresponding asymmetry measured by the polarimeter. This factor is a combination of the initial polarization and the analyzing power.

The measured beam polarizations for crossing spin resonances $G\gamma = 0 + \nu_z$ and $36 - \nu_z$, shown in the bottom part and top part of Fig. 5.8 respectively, also demonstrate that full spin flips were obtained at large coherent betatron oscillations. Since the coherent oscillation amplitude is linearly proportional to the RF dipole strength and inversely proportional to the resonance proximity parameter δ and the particle rigidity $B\rho$, the maximum coherent oscillation amplitude is limited by the achievable RF dipole field strength. Thus, when the RF dipole modulation tune was placed closer to the betatron tune, the AGS RF dipole was able to reach the saturation region but if the two tunes were separated farther, the maximum RF dipole field strength would not be sufficient to excite a strong coherent oscillation to induce a full spin flip.

Unlike the numerical simulation of the intrinsic resonance at $12 + \nu_z$, the simulations of the spin resonances at $0 + \nu_z$ and $36 - \nu_z$ with larger resonance proximity parameter δ shown in Fig. 5.8 show a rather complicated oscillatory behavior which can be explained as the interference of the intrinsic spin resonance and the resonance induced by the RF dipole itself. For the spin resonance at $12 + \nu_z$, since its strength was relatively weak compared with the strengths of the resonances $0 + \nu_z$ and $36 - \nu_z$, it is easier for the induced spin resonance due to the excited coherent motion to dominate and giving a smooth dependence of the measured polarization on the RF dipole field strength. On the other hand, since the intrinsic spin resonances at $0 + \nu_z$ and $36 - \nu_z$ were strong enough to partially flip the spin, they strongly interfere with the coherent spin resonance induced by the RF dipole and give rise

to a significant interference pattern in which the degree of spin flip also depends on the relative phase between the intrinsic spin resonance and the resonance artificially induced by the RF dipole. Nevertheless, this interference pattern should die off and a full spin flip is expected when the strength of the RF-induced spin resonance becomes strong enough.

Both the beam vertical betatron tune and beam emittance are essential parameters determining the tune separation between the two spin resonances and the intrinsic resonance strength in the numerical simulation. It is known that the intrinsic resonance strength is proportional to the size of the vertical betatron oscillation, or equivalently, to the square root of the vertical beam emittance, i.e.

$$\epsilon_1 = \sqrt{\frac{\epsilon_1}{\epsilon_2}} \epsilon_2, \quad (5.23)$$

where ϵ_1 and ϵ_2 are the resonance strength for a beam with emittance ϵ_1 and ϵ_2 . Similarly, the resonance strength of the induced spin resonance is given by

$$\epsilon_{rf} = \frac{Z_{\text{coh}}}{\sigma} \epsilon, \quad (5.24)$$

where ϵ_{rf} is the induced resonance strength and ϵ is the intrinsic resonance strength of a particle at the rms beam size σ .

The simulations for $G\gamma = 12 + \nu_z$ and $36 - \nu_z$ were done with the measured betatron tune. However, since the betatron tune at $G\gamma = 0 + \nu_z$ was not *accurately* measured during the experiment setup, the tune separation δ at $G\gamma = 0 + \nu_z$ was obtained by fitting the experimental data. The best fit corresponded to a tune separation of $\delta = 0.0063 \pm 0.0014$. The beam emittance, on the other hand, was obtained from the measured depolarization with RF dipole off at $G\gamma = 13.5, 24.5$ and 30.5 . Based on the Froissart-Stora formula, the normalized 95% beam emittance was $36 \pm 13 \pi$ mm-mrad for $0 + \nu_z$ and $26 \pm 4 \pi$ mm-mrad for $12 + \nu_z$ and $36 - \nu_z$. This is also consistent with the beam profile measurements taken by the AGS Ionization Profile Measurement (IPM).

However, the IPM measurements were not very reliable due to the low beam intensity. The lower beam emittance for resonances $12 + \nu_z$ and $36 + \nu_z$ was attributed to more careful machine tuning later in the experiment.

Since the vertical betatron tune was mistuned at higher energy flap-tops from the optimal value at the $0 + \nu_z$ for the polarization measurement, there was a $15\% \sim 20\%$ polarization loss. This was reflected in a lower polarization value at the higher energies for the $12 + \nu_z$ and $36 - \nu_z$ spin resonances. This polarization loss at $0 + \nu_z$ can be avoided by properly setting the vertical betatron tune and the RF dipole field strength amplitude.

5.3.2 The resonant proximity parameter δ scan

According to Eq. (3.15), the coherent oscillation amplitude increases when the RF dipole modulation tune is pushed closer and closer to the betatron tune with a fixed RF dipole strength. This, then in turn, will enhance the strength of the induced spin resonance strength. The smaller and smaller distance between the two neighboring resonances also helps to reduce their interference and reach full spin flip.

Figure 5.9 shows the measured beam polarization for the $12 + \nu_z$ intrinsic resonance as a function of the tune separation at a fixed RF dipole field strength of 18.5 Gauss-m. The solid line shows the result of a numerical spin multi-particle simulation. When the RF dipole modulation tune is close to the intrinsic betatron tune, the polarization reaches a plateau of full spin flip.

5.3.3 Effective analyzing power of fishline

The beam polarization P in the AGS is obtained by normalizing the measured left-right asymmetry δ_f of the polarized proton scattering off the fishline target with the

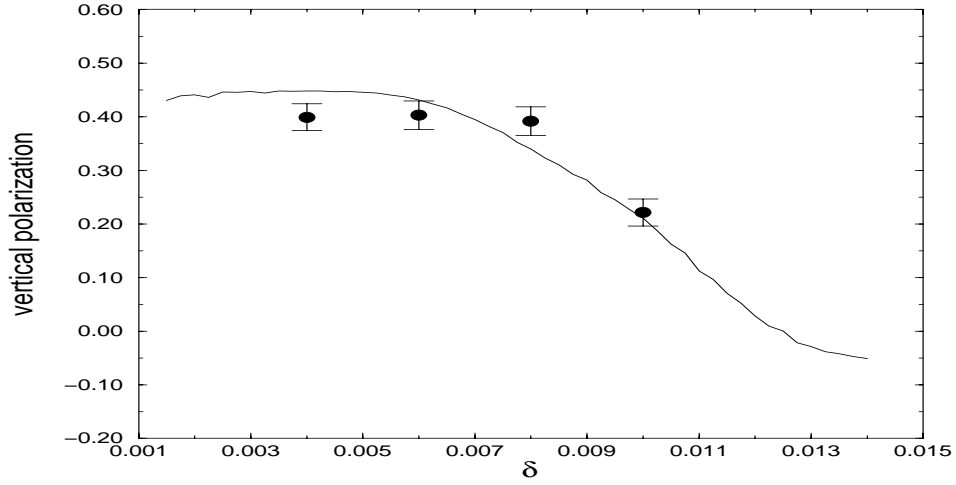


Figure 5.9: The measured proton beam polarization, at the spin resonance $12 + \nu_z$, vs the tune separation with a fixed RF dipole field strength. The line is the multi-particle simulation results with 1 normalized 95% beam emittance of $26\pi\text{mm-mrad}$, and an initial polarization of 0.45.

corresponding analyzing power A_f , i.e.

$$P = \frac{\delta_f}{A_f}. \quad (5.25)$$

Since the fishline target contains both carbon and proton nuclei, the scattering of the proton off the target involves not only $p-p$ elastic scattering but $p-C$ quasi-elastic scattering as well. To obtain the effective analyzing power of the fishline target A_f , a measurement of the asymmetry with a pure carbon target is needed. The effective analyzing power can be expressed as

$$A_f = \frac{A_p}{\alpha}, \quad (5.26)$$

where A_p is the analyzing power of $p-p$ elastic scattering which is well established [15],

and

$$\alpha = \frac{1 - (\delta_c/\delta_f)(N_c/N_f)}{1 - N_c/N_f} \quad (5.27)$$

where δ_c is the asymmetry of the $p - \text{carbon}$ scattering, N_c is the total number of events measured with a carbon target and N_f is the total number of events measured with the fishline target.

Eq. (5.27) is only valid if the number of incident particles are the same. Since, the intensity actually varies from cycle to cycle, and also the number of AGS cycles can be different, the number of total event for different target in Eq. (5.27) should be normalized by both the luminosity and the number of AGS cycles.

Values of various event scalers and their sums were recorded by the AGS internal polarimeter data acquisition system, such as the number of events in each arm of detectors denoted as L and R . To reduce the systematic errors, the polarization vector of the incident beam was flipped between up and down every other AGS cycle. The resulting asymmetry was then calculated as

$$\delta = \frac{\sqrt{L^\uparrow R^\downarrow} - \sqrt{L^\downarrow R^\uparrow}}{\sqrt{L^\uparrow R^\downarrow} + \sqrt{L^\downarrow R^\uparrow}}, \quad (5.28)$$

As discussed in Section (4.3), the VETO counter installed at the end of each detector arm was used to eliminate pion production events from the $p-p$ inelastic scattering events. The VETO counter can be set to different threshold levels. For this particular polarimeter setup, two different levels were used to obtain the left-right asymmetries. The asymmetry obtained with higher threshold level was denoted as $F2$, otherwise $F1$. However, in the experiment, it was found that $F2$ was not as reliable as $F1$ and seldom was used.

Another asymmetry obtained by the AGS internal polarimeter was set up to resemble the AGS old polarimeter measurement for the calibration purposes, and therefore was named “old-asymmetry”. Unlike $F1$ and $F2$ type measurements, old

asymmetry does not use the VETO counter to eliminate pion events. It is this asymmetry which was used to obtain the beam polarization in the data analysis. The data of $F1$ type measurement were used to calibrate the analyzing power for the old asymmetries, i.e. Eq. (5.26) becomes

$$A_f = \frac{\delta_f}{\delta_{F1}/A_{F1}} = \frac{\delta_f}{\delta_{F1}} \frac{A_p}{\alpha_{F1}}, \quad (5.29)$$

where δ_f and δ_{F1} are old and $F1$ asymmetries, α_{F1} is the α factor in Eq. (5.27) based on the $F1$ asymmetry, and A_p is the analyzing power given by Eq. (4.5).

Since the elastic analyzing power A_p is a function of beam momentum, several matched carbon and fishline runs were taken for each energy flat-tops in the experiment. The effective analyzing power was then obtained by averaging over the analyzing power given by each pair of matched runs. Below in Table 5.4 are the analyzing power for different beam energies.

Table 5.4: analyzing power at $G\gamma = 13.5, 24.5$ and 30.5

$G\gamma = 13.5$	run #	A_f	$\overline{A_f}$	A_e
	1	0.05797 ± 0.0067	0.0402 ± 0.0033	0.117
	2	0.04659 ± 0.0060		
	3	0.00382 ± 0.0042		
	4	0.002652 ± 0.0025		
$G\gamma = 24.5$	1	0.02869 ± 0.0030	0.0276 ± 0.0025	0.073
	2	0.02461 ± 0.0042		
$G\gamma = 30.5$	1	0.0186 ± 0.0034	0.0197 ± 0.0027	0.062
	2	0.02108 ± 0.0044		

Puzzles

Many matched carbon and fishline runs were also taken at $G\gamma = 7.5$. However, the analyzing power obtained from those matched runs is lower than the asymmetry itself which unreasonably gives more than 100% beam polarization. It is not very clear what had happened during the measurement. One possible reason is that the carbon target data could be contaminated with scattering events from the fishline target if the two targets are not well separated in space, or the beam size is comparable to the distance between the two targets, or the beam swings around the orbit. The target scan taken at this energy in Fig. 5.10 shows that the two peaks for the fish-line target and carbon target are not well separated.

5.4 Effects of Linear Betatron Coupling

Normally, the horizontal betatron oscillation does not affect the spin motion if the betatron oscillation in the horizontal plane two transverse plane is fully decoupled from the oscillation in the vertical plane. However, since the AGS partial snake is a solenoid magnet, it introduces sizable coupling between the two transverse planes and gives rise to the coupling spin depolarization resonances at horizontal betatron tune. The resonance strength of this type of spin resonance is proportional to the horizontal betatron oscillation amplitude and the coupling strength [6].

Although compared with intrinsic spin resonances the coupling spin resonances are much weaker, there is still noticeable beam polarization loss at these resonances. To minimize the coupling spin resonances, one can separate the horizontal betatron tune from the the vertical betatron tune to reduce the coupling strength, or alternatively, to correct the linear coupling close to the entry and exit of the partial snake using skew quadrupoles.

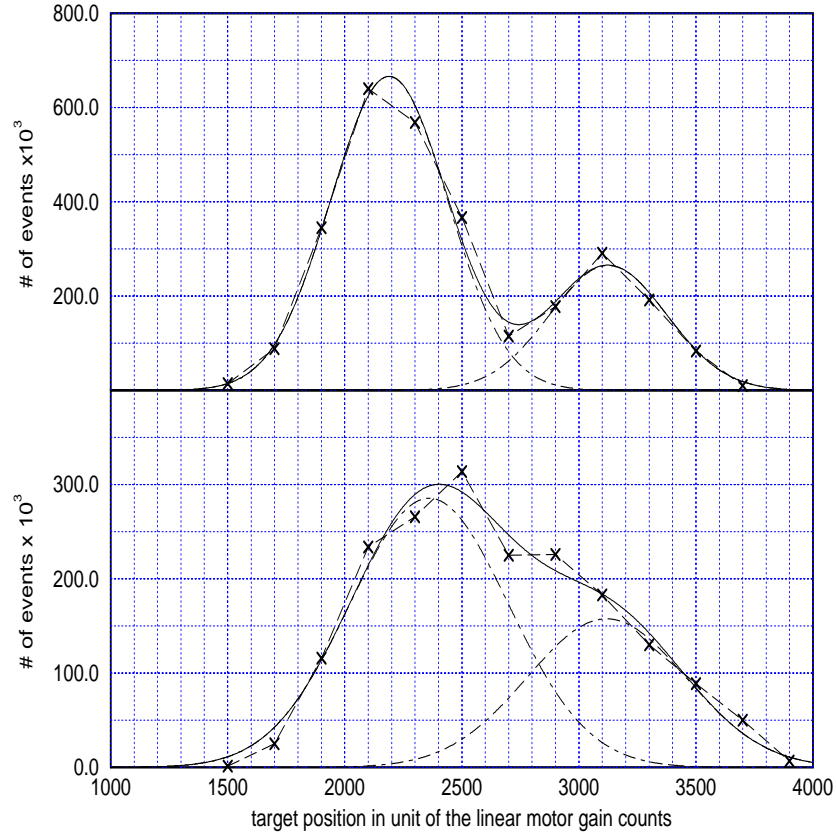


Figure 5.10: Target scans of the AGS internal polarimeter taken at $G\gamma = 13.5$ (top part) and $G\gamma = 7.5$ (bottom part).

5.5 Second Order Spin Resonance

Other than the horizontal magnetic fields arising from the imperfection of the vertical closed orbit and the vertical intrinsic betatron oscillation which drive the imperfection and intrinsic spin depolarization resonances, there are other sources in the accelerator which can also drive higher order spin resonances. For example, the horizontal focusing fields due to horizontal displacement generate spin tune modulations and may induce sidebands around strong resonances. The depolarization caused by such a resonance is in general negligible unless a large horizontal closed orbit excursion

occurs. Unlike the intrinsic spin resonance, this resonance is driven not only by the vertical betatron oscillation but also by the horizontal closed orbit distortion. This new type of spin resonance was first observed in the November 1997 polarized proton experiment at the AGS.

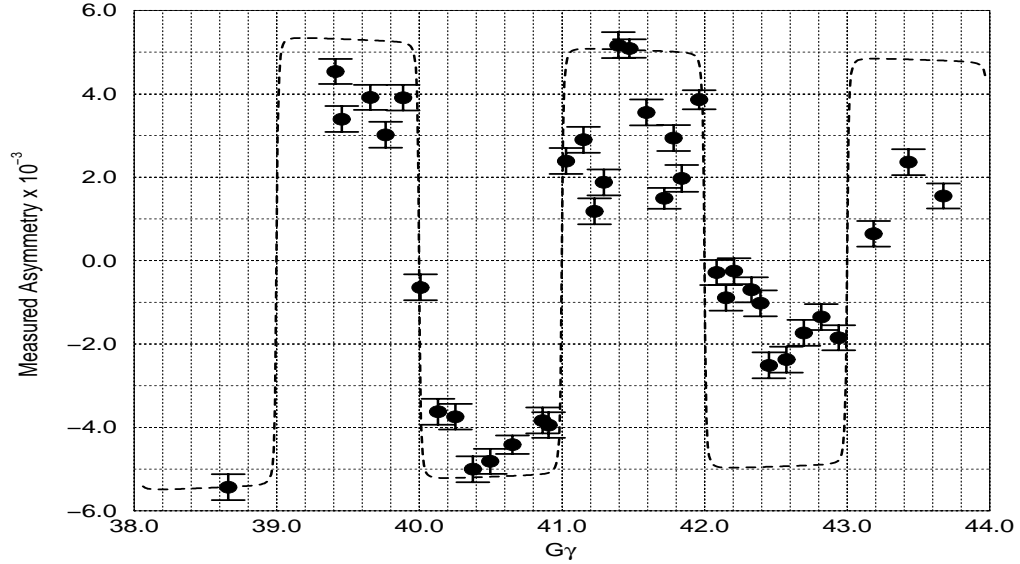


Figure 5.11: The measured asymmetry for different beam energies, or equivalently, $G\gamma$ values. The dotted line shows the asymmetry expected from a 5% partial snake. It is scaled based on the assumption that the analyzing power is inversely proportional to the beam momentum.

Figure 5.11 shows the measured asymmetry as a function of $G\gamma$. The measured asymmetry changed sign at every $G\gamma = \text{integer}$ because of the partial Siberian snake. Additional structure elsewhere occurred because, for a real synchrotron, any small defects break the superperiodicity of the accelerator and generate numerous *gradient error spin resonances* at $G\gamma = k \pm \nu_z$ where integer k is not an integer multiple of the synchrotron's superperiodicity P ; since the strength of the resonance $k \pm \nu_z$ is

very small, it will not cause notable polarization loss at nominal acceleration rate. However, the asymmetry for each energy of Figure 5.11 was measured by coasting the beam at that energy, therefore the rate for a beam to pass through the spin resonance was very low during the measurement and the depolarization effect at $G\gamma = k \pm \nu_z$ was greatly enhanced¹. At $G\gamma = n + \frac{1}{2}$, halfway between two weak intrinsic resonances, the asymmetry reached the expected value as indicated by the dashed line. However, significant depolarization occurred around $G\gamma = 42.3$.

The exact location of this polarization loss was determined by measuring the asymmetry as a function of the turn-on time of the RF dipole which was pulsed in such a way that the vertical beam emittance was significantly increased. If the RF dipole is turned on after the spin resonance, the emittance growth will not affect the final beam polarization. Otherwise, the depolarization effect at this resonance is enhanced. The experimental data are shown in Figure 5.12. The horizontal axis is the value of $G\gamma$ at the time when the RF dipole was turned on. Figure 5.12 shows that when the RF dipole was turned on before crossing the spin resonance the increased emittance made the resonance strong enough to partially flip the beam polarization, demonstrating the dependence of the resonance on the vertical beam emittance. The transition between the two plateaus of asymmetries corresponds to the position of the resonance which is $G\gamma = 42.3$.

To demonstrate the dependence on the horizontal closed orbit distortion, we employed thirty-two harmonic closed orbit correctors in the AGS to eliminate the dominant harmonic component of the horizontal closed orbit distortion. In the AGS,

¹The normal acceleration rate in the AGS is $\alpha = 4.8 \times 10^{-5}$. At the point in the acceleration cycle where the second order spin resonance discussed in this thesis was encountered, the vertical betatron tune was 8.70. The horizontal betatron tune in the AGS was set 8.83. However, due to the off-center beam orbit (+6 mm) and also the large chromaticity (-2.5, unnormalized) at the end of the acceleration cycle, the actual horizontal tune was estimated to be 8.755.

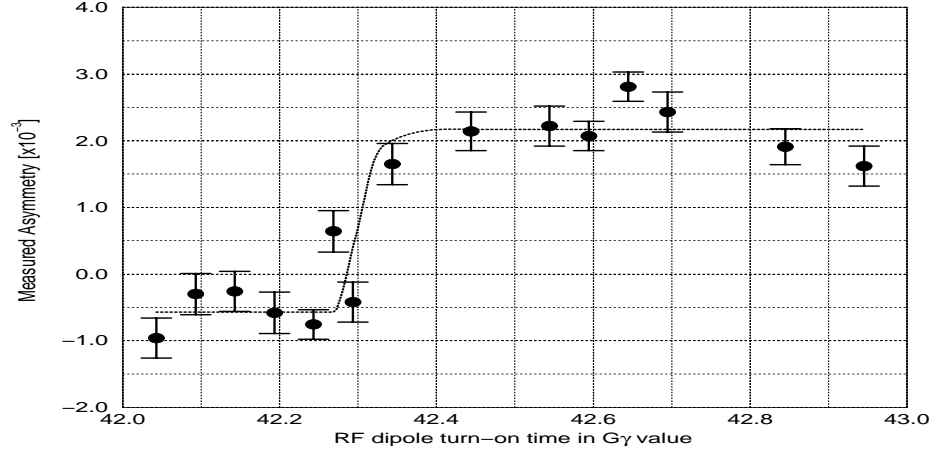


Figure 5.12: Measured asymmetry vs the RF dipole turn-on time in $G\gamma$ value. Powering the RF dipole with a short pulse increased the vertical beam emittance significantly when the RF dipole was turned on before crossing the spin resonance at $G\gamma = 42.3$. The increased emittance made the resonance strong enough to partially flip the beam polarization. The beam polarization was measured at $G\gamma = 43.5$ energy flat-top.

the dominant harmonic component is 9, the nearest integer to the horizontal betatron tune (set about 8.8), the nearest integer is 9 and thus 9^{th} harmonic component is more important than other harmonic components. Two sets of independent correctors were set up to form $\cos 9\theta$ and $\sin 9\theta$. Figure 5.13 shows the measured asymmetry for different corrector settings. The top part is a scan of $\cos 9\theta$ current while the $\sin 9\theta$ current was set at zero. The bottom is the scan of the $\sin 9\theta$ current with the $\cos 9\theta$ current set at 7A. The solid lines are fits of the experimental data based on the Froissart-Stora formula [10] for a beam with a Gaussian distribution betatron amplitude, i.e:

$$\frac{P_f}{P_i} = \frac{1 - \pi|\epsilon|^2/\alpha}{1 + \pi|\epsilon|^2/\alpha}. \quad (5.30)$$

Assuming the rms resonance strength ϵ is proportional to the rms amplitude of horizontal closed orbit distortion \hat{x}_{co} , we find

$$\frac{\pi|\epsilon|^2}{\alpha} = b[(x - c)^2 + (y - d)^2], \quad (5.31)$$

where b , c , and d are constants, and x and y stand for the currents of $\cos 9\theta$ and $\sin 9\theta$, respectively. The best fit occurs for $b = (1.29 \pm 0.18) \times 10^{-3}$, $c = 5.6 \pm 1.5\text{A}$ and $d = -8.0 \pm 1.2\text{A}$. The corresponding strength for this spin resonance without corrections ($x=y=0$) is

$$\epsilon = \sqrt{\frac{b\alpha}{\pi}[c^2 + d^2]} \approx (5.70 \pm 0.87) \times 10^{-4}, \quad (5.32)$$

where the acceleration rate was $\alpha = 0.84 \times 10^{-5} \text{ rad}^{-1}$ and the 95% normalized beam emittance in the vertical plane was about $10\pi \text{ mm-mrad}$ measured by the AGS ionization profile monitor.

To understand the mechanism of this new spin resonance, we start from the BMT equation expressed in terms of the particle's coordinates described in a curvilinear coordinate system [6, 9]:

$$\frac{d\vec{S}}{d\theta} = \vec{S} \times \vec{F} \quad (5.33)$$

where \vec{S} is the spin vector, θ is the orbital bending angle, i.e. $d\theta = ds/\rho$ and $\vec{F} = F_1\hat{x} + F_2\hat{s} + F_3\hat{z}$ with

$$F_1 = -\rho z''(1 + G\gamma), \quad (5.34)$$

$$F_2 = (1 + G\gamma)z' - \rho(1 + G)\left(\frac{z}{\rho}\right)', \quad (5.35)$$

$$F_3 = -(1 + G\gamma) + (1 + G\gamma)\rho x''. \quad (5.36)$$

Here the prime is the derivative with respect to the longitudinal coordinate s , and ρ is the accelerator bending radius. The F_1 and F_2 terms induce depolarization, while the

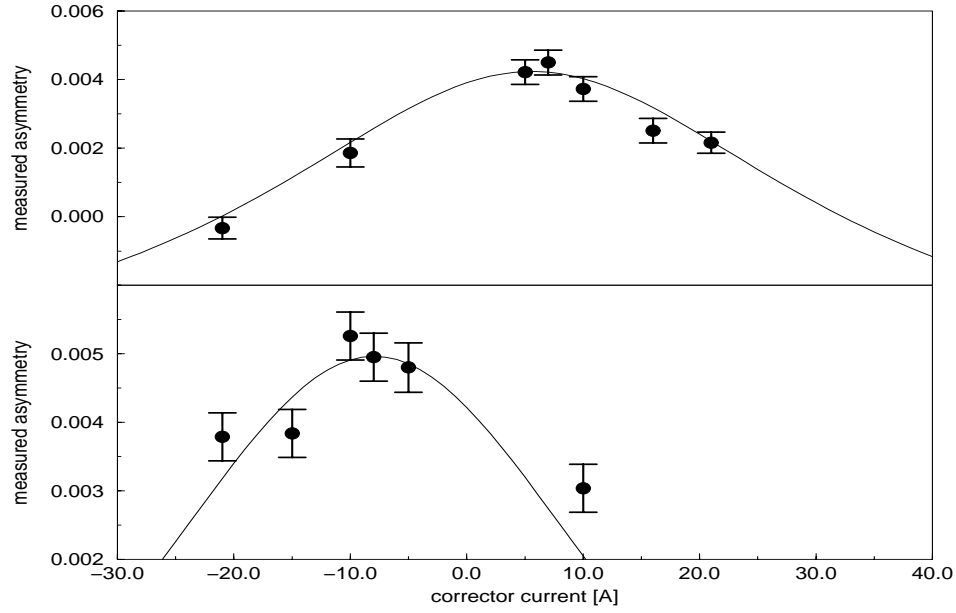


Figure 5.13: Top: Measured asymmetry vs current of correctors which generate $\cos 9\theta$ oscillation while the current of $\sin 9\theta$ correctors was set at zero. Bottom: Scan of the corrector current for the $\sin 9\theta$ oscillation with the corrector current for the $\cos 9\theta$ oscillation set at 7A. The solid lines in both pictures are the fitting results. The range of the corrector power supply was about ± 25 A.

F_3 term causes spin precession about the vertical axis. The second term in F_3 , which is normally small and neglected in first order calculations [9]. However, at certain condition, this term can also induce spin tune modulation and generate sidebands around strong primary spin resonances.

Defining the two component spinor ψ such that $\vec{S} = \langle \psi | \vec{\sigma} | \psi \rangle$ where $\vec{\sigma}$ contains the Pauli matrices [6], we transform the Thomas-BMT equation into the spinor equation of motion

$$\frac{d\psi}{d\theta} = -\frac{i}{2} \begin{pmatrix} G\gamma - (1 + G\gamma)x''\rho & -\xi \\ -\xi^* & -G\gamma + (1 + G\gamma)x''\rho \end{pmatrix} \psi, \quad (5.37)$$

where the off-diagonal element $\xi = F_1 - iF_2$ characterizes the perturbation acting on the spin vector due to the non-vertical magnetic field. Since the particle coordinate in synchrotrons are quasi-harmonic, the spin perturbing terms can be expanded in Fourier series.

$$\xi = \sum_K \epsilon_K e^{-iK\theta}, \quad (5.38)$$

where the amplitude ϵ_K is the spin depolarization resonance strength,

$$\epsilon_K = \frac{1}{2\pi} \int (F_1 - iF_2) e^{iK\theta} d\theta. \quad (5.39)$$

The imperfection resonance occurs at $K = \text{integer}$ and the intrinsic resonance occurs at $K = kP + m\nu_z$. Table (5.2) lists the rms strength of seven AGS intrinsic spin resonances calculated for a beam with 10π mm-mrad 95% normalized vertical emittance [9]. Two additional intrinsic spin resonances at $60 - \nu_z$ and $48 + \nu_z$ will be encountered if the beam is accelerated up to 30 GeV. Among the nine intrinsic spin resonances, the spin resonance at $60 - \nu_z$ is the strongest because every quadrupole in FODO cell then contributes coherently [6].

In the presence of a large horizontal closed orbit distortion, the horizontal coordinate in F_3 cannot be neglected, Transferring Eq. (5.37) into the spin precession frame with

$$\psi_I(\theta) = e^{\frac{i}{2}\sigma_3 \int (G\gamma - ax''\rho) d\theta} \psi(\theta), \quad (5.40)$$

we obtain [6, 28]

$$\frac{d\psi_I}{d\theta} = -\frac{i}{2} \begin{pmatrix} 0 & -\tilde{\xi} \\ -\tilde{\xi}^* & 0 \end{pmatrix} \psi_I, \quad (5.41)$$

where

$$\tilde{\xi} = \xi e^{i \int (G\gamma - (1+G\gamma)x''\rho) d\theta}. \quad (5.42)$$

Substituting Eq. (5.38) into Eq. (5.42) Near a particular spin resonance harmonic K , we obtain

$$\tilde{\xi} \cong \epsilon_K e^{-i(K\theta - \int (G\gamma - (1+G\gamma)x''\rho)d\theta)}. \quad (5.43)$$

In a small range of $G\gamma$, the spin precession phase factor can be approximated to

$$\int_0^\theta (G\gamma - (1+G\gamma)x''\rho)d\theta = G\gamma\theta - (1+G\gamma)x'|_0^\theta. \quad (5.44)$$

Generally, the horizontal displacement is

$$x = x_{co} + x_\beta + D \frac{\Delta P}{P} \quad (5.45)$$

where x_{co} is the horizontal closed orbit distortion, x_β is the betatron coordinate and $D \frac{\Delta P}{P}$ is the off-momentum closed orbit. The horizontal closed orbit distortion x_{co} dominated by the harmonic $n = [\nu_x] = 9$, the nearest integer to the horizontal betatron tune ν_x , is given by

$$x_{co} = \hat{x}_{co} \cos(n\phi), \quad (5.46)$$

$$x'_{co} = \frac{dx_{co}}{ds} = -\hat{x}_{co} \frac{n}{\nu_x \beta_x} \sin(n\phi), \quad (5.47)$$

where $\phi = \frac{1}{\nu_x} \int_0^s \frac{1}{\beta_x(t)} dt$ with ν_x and β_x being the horizontal betatron tune and amplitude function, and $\phi' = 1/\nu_x \beta \approx 1/R$. Thus $\phi \approx \theta$ and the spin precession phase factor in Eq. (5.43) becomes

$$G\gamma\theta - (1+G\gamma)x'|_0^\theta = G\gamma\theta + g \sin(n\theta), \quad (5.48)$$

where $g = \hat{x}_{co} \frac{(1+G\gamma)n}{R}$ and R is the average radius of the accelerator. The spin perturbation kernel $\tilde{\xi}$ becomes

$$\tilde{\xi} = \epsilon_K e^{-i(K\theta - G\gamma\theta - g \sin(n\theta))} = \sum_{l=-\infty}^{l=\infty} \epsilon_K J_l(g) e^{-i(K - G\gamma - nl)\theta}. \quad (5.49)$$

Here $e^{ig \sin(n\theta)}$ is expanded into Fourier series, and $J_l(g)$ are the Bessel functions.

If $G\gamma = K - nl$, the spin perturbation kernel of Eq. (5.49) will introduce strong perturbations to the spin motion. This new set of spin depolarization resonances is located at sidebands of the primary spin resonance at $G\gamma = K$. Their resonance strengths are

$$\epsilon_{K-nl} = \epsilon_K J_l(g). \quad (5.50)$$

Hence, the stronger the primary spin resonance, the stronger the sideband resonances. Normally, $g \ll 1$, $J_1(g) \approx g/2$ and other Bessel functions with $l > 1$ are higher order in g , which implies that $K - n$ is the strongest among the set of sideband resonances. For the AGS, the sideband spin resonance at $G\gamma = 60 - \nu_z$ is extremely strong and therefore the spin resonance parasitic to $60 - \nu_z$ can cause depolarization if a large horizontal closed orbit distortion exists. Since the closed orbit distortion in the AGS is dominated by harmonic 9, the sideband resonance is located at $60 - 9 - \nu_z = 42.3$, as observed in the experiment in which the AGS vertical betatron tune ν_z was 8.7. The strength of the resonance at $60 - 9 - \nu_z$ is

$$\epsilon_{60-9-\nu_z} = \frac{g}{2} \epsilon_{60-\nu_z} = \left[\frac{9(1+G\gamma)}{2R} \hat{x}_{co} \right] \epsilon_{60-\nu_z}. \quad (5.51)$$

For the AGS, the resonance strength at $60 - \nu_z$ is 0.064 for a beam with 10π mm-mrad 95% normalized vertical emittance [9]. In order to compare the analytical results and the experimental results, the harmonic corrector current must be converted to its corresponding closed orbit distortion. However, due to the low intensity of the polarized proton beam, the closed orbit could not be directly measured for the various harmonic corrector currents. For the harmonic corrector currents set as $(I_{\cos 9\theta}, I_{\sin 9\theta}) = (5.6A, -8.0A)$, the closed orbit distortion is optimally compensated. Therefore, the uncorrected closed orbit distortion can be estimated from the known machine lattice with the harmonic corrector currents set $(I_{\cos 9\theta}, I_{\sin 9\theta}) =$

$(-5.6A, 8.0A)$, and the betatron tunes set at $\nu_x = 8.755, \nu_z = 8.7$. The estimated uncorrected closed orbit distortion amplitude was about 7 mm, and the resonance strength calculated from Eq. (5.51) was then equal to 6.8×10^{-4} , which is consistent with the experimental results of 5.7×10^{-4} . This spin depolarization resonance can also be induced by the sextupoles. However, based on our accelerator modeling of the AGS, the resonance strength from the sextupoles is one order of magnitude too small to explain the experimental results.

Chapter 6

Conclusions and Future Prospects

6.1 Conclusions

Because of the interactions between the spin vector and magnetic fields in the accelerators, special schemes and methods are needed to accelerate polarized protons to high energies without destroying the beam polarization. Driven by the vertical betatron oscillation, intrinsic spin resonances are one of the major types of spin resonances and can cause substantial beam polarization loss. One way to cure this spin resonance is to use a fast quadrupole magnet to jump the vertical betatron tune through the resonance line. However, this tune jump method is a non-adiabatic process and can cause beam emittance dilution in the phase space.

On the other hand, because the intrinsic spin resonance strength is proportional to the particle's vertical betatron oscillation amplitude, particles close to the core of the beam experience weaker spin resonance than the particles on the edge of the beam. This situation can be improved by exciting a coherent oscillation so that the spin motion of core particles then sees stronger perturbing magnetic fields. Thus, the overall beam effective resonance strength is enhanced and a full spin flip can be

induced if the coherent oscillation is strong enough.

To achieve this, an RF dipole with its magnetic field oscillating at a frequency close to the intrinsic betatron oscillation frequency can be employed to induce a controllable coherent oscillation. This has been demonstrated in the AGS with the unpolarized Au^{+77} beam. In the experiment, the RF dipole was gradually turned on and off. A sustained coherent oscillation was adiabatically excited and the beam emittance was preserved. As a non-destructive beam manipulation, this method has been successfully applied in the AGS polarized proton acceleration to overcome the intrinsic spin depolarization resonances at $0 + \nu_z$, $12 + \nu_z$ and $36 - \nu_z$, where ν_z is the vertical betatron tune. The results of the recent AGS polarized proton acceleration experiments showed that the beam polarization was saturated at large coherent oscillations and full spin flip was obtained.

Since the RF dipole has to be operated off resonance to maintain the beam stability for an accelerator with linear optics, the polarized beam will then encounter not only an intrinsic spin resonance at the betatron oscillation frequency but also an artificial spin resonance induced by the RF dipole at its oscillating frequency. Normally, the two frequencies are close to each other. Thus, the two spin resonances will interfere with each other if they are close enough to overlap, and the final beam polarization will be determined not only by their strengths but also by the phase between the two resonances. Hence, to make the RF dipole more efficient, it is desirable to set the RF dipole frequency closer to the intrinsic betatron frequency, which will then, in turn, require a very small chromaticity value. In the experiment, we were able to set a very small vertical chromaticity by adjusting the AGS chromatic sextupoles, and put the RF dipole modulation tune as close as 0.004 away from the vertical betatron tune.

In the recent AGS polarized proton experiments, a new type of spin resonance was also observed. It was verified in the experiment that this resonance occurs at $G\gamma = 60 - 9 - \nu_z$ and is related to not only the vertical betatron oscillation but horizontal

closed orbit distortion as well. Here, ν_z is the vertical intrinsic betatron tune and 9 is the dominant harmonic component of the horizontal closed orbit distortion.

This can be understood as a second order effect due to the vertical fields arising from the horizontal closed orbit excursion which lead to spin tune modulation and induce a series of sidebands around every intrinsic spin resonance. The resonance strength of the l_{th} sideband is the strength of the intrinsic resonance modulated by the l_{th} Bessel function with a variable proportional to the rms amplitude of the horizontal closed orbit distortion, and they occur at $K - nl - \nu_z$. Here, K is the corresponding intrinsic resonance, n is the harmonic component of the horizontal closed orbit, for AGS $n = 9$. Among these resonances, the 1st order sideband is the strongest one. Normally, these resonances are all negligible. However, since in the AGS the $60 - \nu_z$ spin resonance is extremely strong (its strength is about an order of magnitude higher than other intrinsic spin resonance strengths), the $60 - 9 - \nu_z$ will then cause notable polarization loss as observed in the experiment if there is also a large horizontal closed orbit distortion. To correct this resonance, the harmonic component of the horizontal closed orbit distortion must be eliminated. In the experiment, this was accomplished by using horizontal correctors distributed in the AGS.

6.2 Prospects Of Polarized Proton Beam Acceleration in the AGS

Although the recent AGS polarized proton acceleration experiments have demonstrated that the beam polarization was preserved at intrinsic resonances $0 + \nu_z$, $12 + \nu_z$ and $36 - \nu_z$, the beam polarization still suffers about 20% loss. A further study showed that this is mainly due to the linear coupling spin depolarization resonances. The linear coupling is primarily caused by the longitudinal magnetic field of the partial

Siberian snake. An empirical estimation of the coupling resonance strength is that it is about 3~5% of the intrinsic resonance strength. Hence, the stronger the intrinsic spin resonance, the stronger the coupling resonance. This is especially bad for intrinsic resonance $36 + \nu_z$ whose coupling resonance can cause about 10% polarization loss.

The linear coupling spin resonances are hard to deal with individually because of the weak resonance strength, making the RF dipole method, for example, ineffective for this type of spin resonance. One possible way to minimize the depolarization due to the coupling resonance is to replace the solenoid partial Siberian snake with a transverse field snake such as a Steffen snake or a helical snake. By doing so, it is expected that the beam polarization loss can be minimized. Figure 6.1¹ shows the comparison of the numerical tracking results with the regular AGS solenoid partial snake and with a helical partial snake. The substantial improvement of the final beam polarization by changing the partial snake magnetic field orientation is evident.

¹courtesy of Dr. H. Huang, BNL.

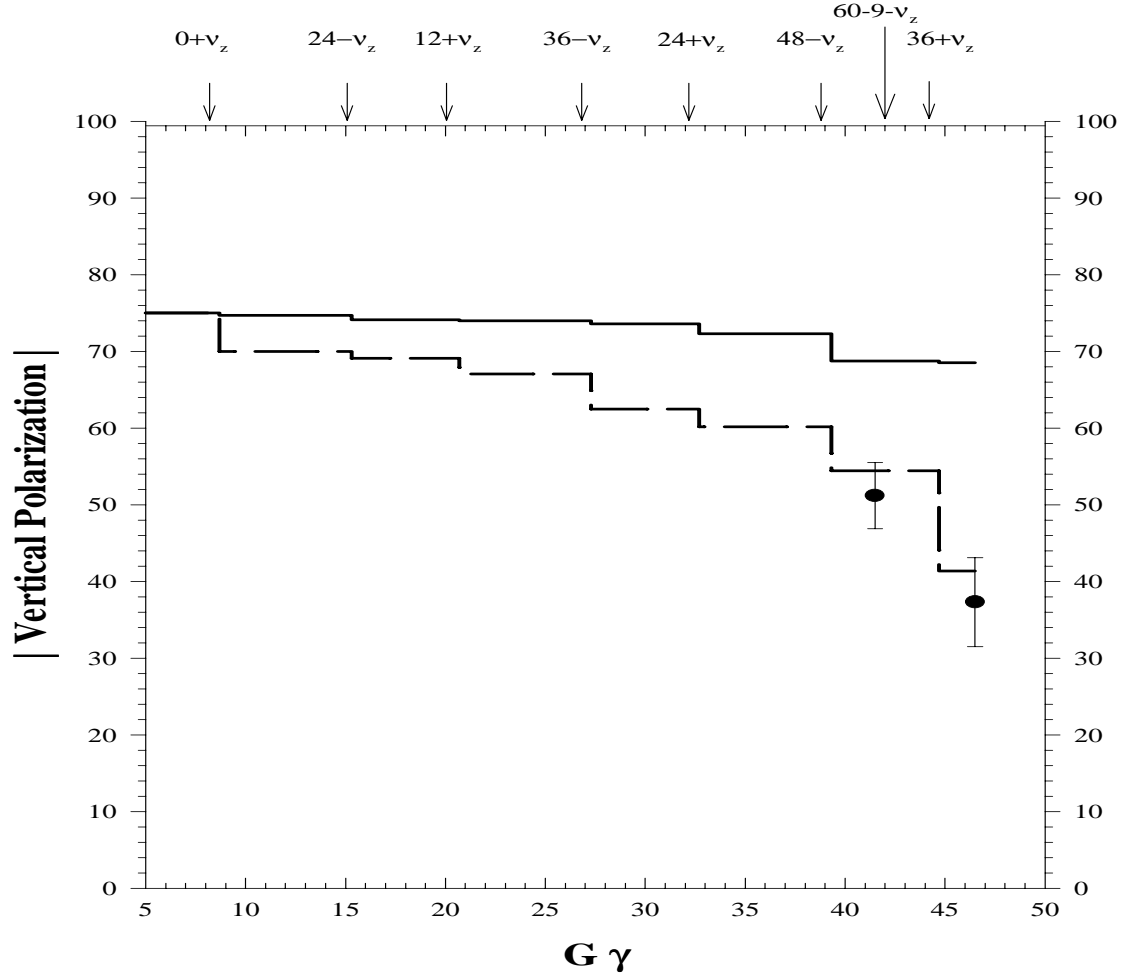


Figure 6.1: Results of numerical spin tracking with the regular AGS solenoid partial snake (dashed line) and with a 5% helical partial snake (solid line). The dots are the experimental results. The weak spin resonances at $G\gamma = 24 \pm \nu_z$ and $48 - \nu_z$ were corrected by the energy-jump method [26] in the numerical tracking with the helical partial snake. No corrections were taken for the weak resonances in the numerical tracking with the regular AGS solenoid partial snake. The RF dipole was used to overcome the intrinsic spin resonances at $G\gamma = 0 + \nu_z$, $12 + \nu_z$ and $36 \pm \nu_z$ in both calculations, and the beam emittance at horizontal and vertical plane is 40π mm-mrad and 9π mm-mrad respectively.

Appendix A

Multi-particle distribution in the numerical simulation of two spin resonance model

In the numerical simulation with two nearby spin resonances, beam polarization is calculated by averaging the spin vector of individual particle. Thirty-two particles are used in the numerical simulation to resemble a Gaussian distributed particles. Since the intrinsic spin resonance strength of a particle is proportional to its betatron oscillation amplitude [see Eq. (3.32)], the resonance strength for each particle is weighted by its distribution factor $w(J)$, where J is proportional to the particle's action.

The thirty-two particles are divided into four different groups. Each group contains 8 particles distributed uniformly in phase with the same weight factor $w(J)$, i.e. -0.2671 , -0.94 , -1.9617 and -4.1589 . Since

$$\frac{1}{2}(e^{-0.2671/2.0} + e^{-0.94/2.0} + e^{-1.9617/2.0} + e^{-4.1589/2.0}) = 1.0,$$

the statistical average of these thirty two particles is equivalent to a beam with

Gaussian distribution $\rho(J)$

$$\rho(J) = \frac{1}{2}e^{-J/2}. \quad (\text{A.1})$$

Fig. A.1 is a schematic drawing of the thirty-two particles distribution. Here, the

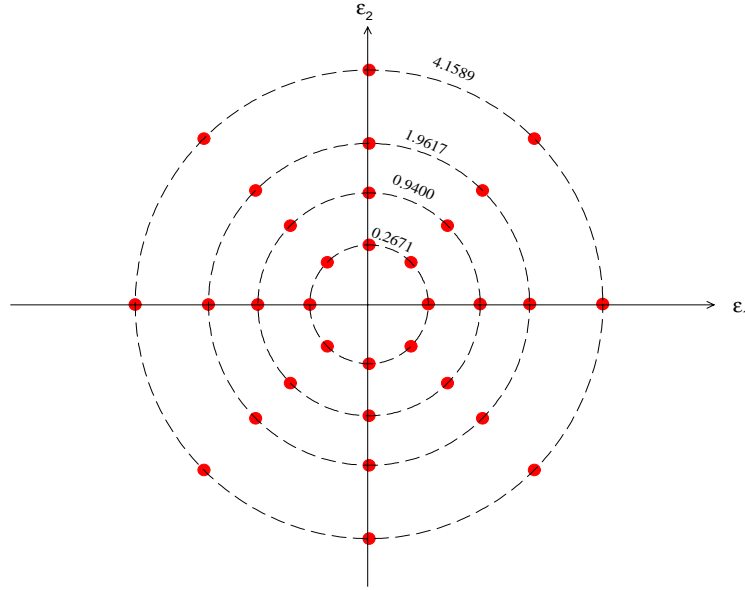


Figure A.1: The distribution of thirty-two particles which simulates a Gaussian distributed beam

length of the vector which starts from the origin and ends at each particle gives the J factor in Eq. (A.1), and the particle's spin resonance phase is determined by the direction of the vector.

Appendix B

Other applications of adiabatic coherent excitation

Compared with the method of exciting a coherent oscillation by a pulsed dipole magnet or other non-adiabatic manipulations, the method of using RF dipole will not cause the beam filament in phase space due to the guide field nonlinearities inherent in the accelerator and destroy the beam condition. As a non-destructive and controllable method, it can be applied to many applications which require minimum disturbance of machine operations. Two possible applications are listed as follows.

B.1 Using the RF dipole as a diagnostic tool to measure the Courant-Snyder parameters

In this application, two beam position monitors (BPMs) which can digitize the turn-by-turn betatron oscillation are needed. Fig. B.1 is the schematic drawing of the system. It is known that the coordinates at BPM2 are related with the coordinates

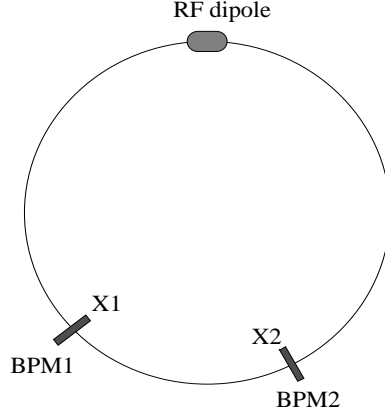


Figure B.1: the schematic drawing of using an RF dipole and two BPMs to measure the linear optics.

at BPM1 through

$$\begin{pmatrix} x_2 \\ x'_2 \end{pmatrix} = \begin{pmatrix} \sqrt{\frac{\beta_2}{\beta_1}}(\cos \psi_{21} + \alpha_1 \sin \psi_{21}) & \sqrt{\beta_1 \beta_1} \sin \psi_{21} \\ -\frac{1+\alpha_1 \alpha_2}{\sqrt{\beta_1 \beta_2}} \sin \psi_{21} + \frac{\alpha_1 - \alpha_2}{\sqrt{\beta_1 \beta_2}} \cos \psi_{21} & \sqrt{\frac{\beta_1}{\beta_2}}(\cos \psi_{21} - \alpha_2 \sin \psi_{21}) \end{pmatrix} \begin{pmatrix} x_1 \\ x'_1 \end{pmatrix}. \quad (\text{B.1})$$

Therefore, x'_1 can then be expressed by the positions at the two BPMs, i.e.

$$x'_1 = \frac{x_2}{\sqrt{\beta_1 \beta_2} \sin \psi_{21}} - \frac{\cot \psi_{21} + \alpha_1}{\beta_1} x_1. \quad (\text{B.2})$$

By putting x'_1 into the Courant-Snyder constant

$$x_1^2 + (\beta_1 x'_1 + \alpha_1 x_1)^2 = 2\beta_1 J, \quad (\text{B.3})$$

an elliptical equation is obtained

$$x_1^2 + \left(\sqrt{\frac{\beta_1}{\beta_2}} \frac{x_2}{\sin \psi_{21}} - \cot \psi_{21} x_1 \right)^2 = 2\beta_1 J. \quad (\text{B.4})$$

Hence, the ratio of the betatron functions $\sqrt{\frac{\beta_1}{\beta_2}}$, the phase advance between the two BPMs ψ_{21} and $\beta_1 J$ can be obtained by fitting the turn-by-turn data recorded at the

two BPMs. Since the coherent oscillation is excited by the RF dipole, the action J is determined by the excitation level, i.e. $J = \frac{1}{2}Z_{coh}^2$, and the betatron function β_1 can be then calculated. With a third BPM data, the function α can also be obtained.

B.2 Spin flipper

Another application on spin manipulation is to use the RF dipole as a spin flipper [22] which flips the spin vector direction by 180° . This could be a useful method to reduce the systematic error for the spin physics experiments at high energy storage rings.

As a spin flipper, the RF dipole induces a spin depolarization resonance at the frequency of its oscillating field. By ramping the frequency of the RF dipole oscillating field through the spin precession frequency, the beam polarization will evolve as Froissart-Stora formula, i.e.

$$\frac{P_f}{P_i} = 2e^{\pi|\epsilon_K|^2/2\alpha} - 1, \quad (\text{B.5})$$

where P_f and P_i are the final and initial polarizations, ϵ_K is the spin resonance strength of the spin flipper and α is the ramping rate of the RF dipole frequency. Therefore, for a given ramping rate α , a full spin flip can be obtained if the resonance strength ϵ_K is strong enough.

Unlike the strength of the spin resonance due to the large amplitude coherent oscillation by operating an RF dipole close to the vertical betatron tune which is proportional to the amplitude of the oscillation (see Eq. (3.37)), the resonance strength of a spin flipper is independent of the lattice parameters and fully determined by the magnetic field strength of the spin flipper. Based on the Thomas-BMT equation, the resonance strength is given by

$$\epsilon_K = \frac{1 + G\gamma}{4\pi} \frac{\Delta B \Delta L}{B\rho}, \quad (\text{B.6})$$

where $\Delta B \Delta L$ is the integrated field strength of the spin flipper. To achieve more than 99% spin flip, the spin resonance strength ϵ_K of the spin flipper should be greater than $1.84\sqrt{\alpha}$.

Appendix C

Figure 5.4 and Figure 5.3 data

Table C.1: Data of Figure 5.4.

$\nu_m - \nu_z$	$\frac{Z_{\text{coh}}}{B_m L}$ [mm/Gauss-m]	Z_{coh} [mm]
-0.0243	0.572 ± 0.114	3.692
-0.0224	0.671 ± 0.120	4.250
-0.0124	1.114 ± 0.139	5.305
-0.0059	1.972 ± 0.237	6.370
-0.0048	2.256 ± 0.183	9.542
0.0026	4.851 ± 0.704	7.325
0.0061	1.886 ± 0.258	7.782
0.0122	1.020 ± 0.143	6.576
0.0186	0.747 ± 0.149	4.529

Table C.2: Data of Figure 5.3.

$\nu_m - \nu_z$	$\frac{Z_{\text{coh}}}{B_m L}$ [mm/Gauss-m]	Z_{coh} [mm]
-0.0476	0.277 ± 0.046	2.00
-0.0359	0.390 ± 0.051	2.82
-0.0280	0.477 ± 0.051	3.45
-0.0231	0.579 ± 0.046	4.19
-0.0181	0.752 ± 0.051	5.44
-0.0143	0.927 ± 0.051	6.70
-0.0120	1.122 ± 0.065	8.12
-0.0058	1.980 ± 0.084	9.80
0.0079	1.713 ± 0.056	8.48
0.0121	1.122 ± 0.051	8.12
0.0157	0.851 ± 0.065	6.16
0.0191	0.676 ± 0.065	4.89
0.0231	0.581 ± 0.056	4.20
0.0315	0.419 ± 0.056	3.03
0.0365	0.343 ± 0.056	2.48
0.0502	0.249 ± 0.060	1.80

Appendix D

Figure 5.8 and Figure 5.9 data

Table D.1: Data of the RF dipole amplitude scan and the resonance proximity parameter δ scan at $12 + \nu_z$ in Figure 5.8 and Figure 5.9.

$ \nu_m - \nu_z $	P_z
0.00	0.399 ± 0.025
0.01	0.403 ± 0.027
0.01	0.392 ± 0.027
0.01	0.221 ± 0.025

$ \nu_m - \nu_z $	Z_{coh} [mm]	P_z
0.004	0	0.013 ± 0.018
	19.49	0.399 ± 0.025
	16.88	0.443 ± 0.017
	14.90	0.448 ± 0.030
	11.73	0.439 ± 0.023
	9.74	0.399 ± 0.026
	6.97	0.299 ± 0.025
	3.49	0.151 ± 0.024

Table D.2: Data of RF dipole amplitude scan at $0 + \nu_z$.

$ \nu_m - \nu_z $	Z_{coh} [mm]	P_z
0.0063	0	0.500 ± 0.051
	2.19	0.457 ± 0.021
	6.09	0.323 ± 0.025
	9.26	0.370 ± 0.025
	12.30	0.500 ± 0.024
	15.11	0.567 ± 0.025
	17.79	0.606 ± 0.026
	19.86	0.681 ± 0.024
0.010	1.02	0.415 ± 0.024
	2.91	0.215 ± 0.024
	4.41	0.098 ± 0.028
	5.77	0.073 ± 0.027
	7.20	0.044 ± 0.027
	8.49	0.124 ± 0.025
	9.62	0.179 ± 0.024
0.0163	0.66	0.331 ± 0.026
	1.84	0.230 ± 0.025
	2.68	0.118 ± 0.025
	3.53	-0.094 ± 0.022
	4.332	-0.158 ± 0.025
	5.18	-0.186 ± 0.025
	5.89	-0.141 ± 0.025

Table D.3: Data of RF dipole amplitude scan at $36 - \nu_z$.

$ \nu_m - \nu_z $	Z_{coh} [mm]	P_z
0.005	0	-0.255 ± 0.025
	2.35	-0.250 ± 0.037
	4.65	-0.353 ± 0.037
	6.73	-0.378 ± 0.035
	8.64	-0.347 ± 0.038
	10.18	-0.396 ± 0.038
	11.71	-0.421 ± 0.039
	13.13	-0.392 ± 0.037
	13.40	-0.373 ± 0.038
0.010	6.70	-0.247 ± 0.037
	6.46	-0.218 ± 0.037
	5.83	-0.154 ± 0.038
	5.09	-0.118 ± 0.037
	4.32	-0.109 ± 0.038
	3.36	-0.097 ± 0.037
	2.38	-0.131 ± 0.038
	1.15	-0.204 ± 0.036
	0	-0.255 ± 0.025
0.020	0	-0.255 ± 0.025
	3.36	0.146 ± 0.035
	2.91	0.150 ± 0.037
	2.16	0.044 ± 0.035
	1.19	-0.147 ± 0.035

Appendix E

Experimental data of second order resonance.

Table E.1: Data of $\cos 9\theta$ and $\sin 9\theta$ current scan in Figure 5.13.

$\cos 9\theta$ current	measured asymmetry $\times 10^{-3}$	$\sin 9\theta$ current	measured asymmetry $\times 10^{-3}$
-21 [A]	-0.33 ± 0.32	-10 [A]	5.26 ± 0.35
-10 [A]	1.86 ± 0.41	-8 [A]	4.95 ± 0.37
5 [A]	4.22 ± 0.36	-21 [A]	3.79 ± 0.35
7 [A]	4.5 ± 0.36	10 [A]	3.04 ± 0.35
10 [A]	3.73 ± 0.36	-15 [A]	3.84 ± 0.35
16 [A]	2.51 ± 0.36	-5 [A]	4.8 ± 0.35
21 [A]	2.16 ± 0.31		

Table E.2: Data of energy scan in Figure 5.11.

$G\gamma$	P_z	$G\gamma$	P_z
38.66	-5.43 ± 0.31	41.40	5.17 ± 0.31
39.41	4.54 ± 0.3	41.47	5.09 ± 0.22
39.46	3.40 ± 0.31	41.59	3.56 ± 0.31
39.66	3.92 ± 0.3	41.72	1.50 ± 0.25
39.76	3.02 ± 0.31	41.78	2.94 ± 0.31
39.89	3.91 ± 0.31	41.84	1.98 ± 0.32
40.01	-0.638 ± 0.31	41.96	3.86 ± 0.23
40.13	-3.62 ± 0.31	42.08	-0.28 ± 0.30
40.25	-3.74 ± 0.31	42.15	-0.89 ± 0.31
40.37	-5.00 ± 0.31	42.21	-0.25 ± 0.31
40.50	-4.81 ± 0.3	42.33	-0.70 ± 0.30
40.65	-4.41 ± 0.22	42.39	-1.02 ± 0.31
40.86	-3.83 ± 0.31	42.45	-2.51 ± 0.31
40.91	-3.94 ± 0.31	42.57	-2.37 ± 0.31
41.03	2.39 ± 0.31	42.70	-1.73 ± 0.31
41.15	2.90 ± 0.31	42.82	-1.35 ± 0.31
41.23	1.19 ± 0.31	42.94	-1.85 ± 0.30
41.29	1.88 ± 0.31	43.18	0.65 ± 0.31
43.43	2.36 ± 0.31	43.67	1.55 ± 0.31

Table E.3: Data of RF dipole turn-on time scan in Figure 5.12.

$G\gamma$	P_z
42.04 [A]	-0.96 ± 0.30
42.09 [A]	-0.30 ± 0.31
42.14 [A]	-0.26 ± 0.30
42.19 [A]	-0.58 ± 0.31
42.24 [A]	-0.76 ± 0.22
42.27 [A]	0.64 ± 0.31
42.29 [A]	-0.42 ± 0.30
42.34 [A]	1.65 ± 0.31
42.44 [A]	2.14 ± 0.29
42.54 [A]	2.22 ± 0.30
42.59 [A]	2.07 ± 0.22
42.64 [A]	2.81 ± 0.22
42.69 [A]	2.43 ± 0.30
42.84 [A]	1.91 ± 0.27
42.94 [A]	1.62 ± 0.30

Bibliography

- [1] I. M. Ternov, Yu. M. Loskutov and L. I. Korovina, Soc. Phys. JETP, 14 (1962) 921.
- [2] F. Z. Khiari *et al.*, Phys. Rev. D**80**, 45 (1989).
- [3] Ya. S. Derbenev and A. M. kondratenko, Part. Accel. 8 115 (1978).
- [4] A. D. Krish *et al.*, Phys. Rev. Lett. 63, 1137 (1989).
- [5] L.H. Thomas, Phil. Mag. 3, 1 (1927); V.Bargmann, L. Michel, and V.L. Telegdi, Phys. Rev. Lett. **2**, 435 (1959).
- [6] S.Y. Lee, *Spin Dynamics and Snakes in Synchrotrons*, (World Scientific Pub. Co., Singapore, 1997).
- [7] Design Report of Polarized Proton at RHIC, 1997.
- [8] T. Khoe *et al.*, Part. Accel. **6**, 213 (1975).
- [9] E.D. Courant and R. Ruth, BNL report, BNL-51270 (1980).
- [10] M. Froissart and R. Stora, Nucl. Inst. Meth. **7** 297 (1960).
- [11] H. Huang *et al.*, Phys. Rev. Lett. **73**, 2982 (1994).
- [12] H. Huang, Ph.D. Thesis, Indiana University (1994).

- [13] LabVIEW Analysis VI Reference Manual, 1994
- [14] B.B. Blinov, *et al.*, Phys. Rev. Lett. **73**, 1621 (1994).
- [15] H. Spinka et al. Nucl. Instrum. Methods 211, 239 (1983).
- [16] T. Roser, in *High-Energy Spin Physics-1988, Proceedings of the 8th International Symposium on High-Energy Spin Physics*, Minneapolis, 1988, edited by K. J. Heller, AIP Conf. Proc. No. 187 (AIP, New York, 1989), P.1442.
- [17] H. Weisberg *et al.*, IEEE Trans. Nucl. Sci. **NS-30**, 2179 (1983).
- [18] E. Blesser, AGS/AD/Tech Note No. 288.
- [19] E. Auerbach, E. Blesser, and R. Thern, AGS/AD/Tech Note No. 276.
- [20] M. Syphers, *An introduction to the physics of high energy accelerators*, (John Wiley & Sons, Inc., 1993).
- [21] D.D. Caussyn *et al.*, Phys. Rev. Lett. **73**, 2857 (1994).
- [22] A. Chao and M. Tigner, *Handbook of Accelerator Physics and Engineering*, to be published.
- [23] M. Bai *et al.*, Phys. Rev. E **56**, 5 (1997).
- [24] S. Tepikian, S.Y. Lee, E.D. Courant, Particle Accelerators **20**, 1 (1986).
- [25] S. Y. Lee and S. Tepikian, IEEE Trans. Nucl. Sci. NS-32, 2225 (1985).

- [26] H. Huang, et al., *Overcoming Weak Intrinsic Depolarizing Resonances with Energy Jump*, IEEE Particle Accelerator Conference and International Conference on High-Energy Accelerators, Vancouver, May, 1997.
- [27] M. Bai *et al.*, Phys. Rev. Lett. **80**, 4673 (1998).
- [28] S. Y. Lee and M. Berglund, Phys. Rev. E**54**, 806 (1996).
- [29] Hans Grote, and F. Christoph Iselin *The MAD Program User's Reference Manual*, CERN/SL/90-13 (AP).
- [30] L. Laclare *et al.*, J. Phys. (Paris), Colloq. **46**, C2-499 (1985).
- [31] H. Sato *et al.*, Nucl. Instrum. Methods Phys. Res., Sect. A **272**, 617 (1988).
- [32] E. D. Courant and H. S. Snyder, *Theory of the Alternating Gradient Synchrotron*, Ann. Phys. 3, 1 (1958).